# CURRENT-PROGRAMMED MODE CONTROL STRATEGIES FOR ELECTROSURGICAL GENERATORS

by

DANIEL A. FRIEDRICHS

B.S.E.E., South Dakota State University, 2008

A thesis submitted to the

Faculty of the Graduate School of the

University of Colorado in partial fulfillment

of the requirement for the degree of

Doctor of Philosophy

Department of Electrical, Computer, and Energy Engineering

2011

This thesis entitled:

"Current-Programmed Mode Control Strategies for Electrosurgical Generators"

written by Daniel A. Friedrichs

has been approved for the Department of Electrical, Computer, and Energy Engineering

_____

Robert W. Erickson, Ph.D.

_____

Dragan Maksimović, Ph.D.

Date_____

The final copy of this thesis has been examined by the signatories, and we find that both the content and the form meet acceptable presentation standards for scholarly work in the above mentioned discipline.

# ABSTRACT

Friedrichs, Daniel A. (Ph.D., Electrical Engineering, Department of Electrical, Computer, and Energy Engineering)

Current-Programmed Mode Control Strategies for Electrosurgical Generators

Thesis directed by Professor Robert W. Erickson

Electrosurgery is used in modern surgical practice to cause various desirable clinical effects by invoking $I^2R$ heating in tissue. The ability to achieve a consistent clinical result is predicated on the ability of the electrosurgical instrument to deliver a well-regulated constant output power, capable of quickly responding to changes in tissue impedance. Yet, electrosurgical devices available today suffer from very poor transient output power regulation, with potential for improvement limited by inherent restrictions in the chosen system architectures.

This thesis presents a revolutionary new approach to the design of electrosurgical power supplies by employing current-programmed mode ("CPM") control strategies to inherently achieve the desired output characteristic: a constant power AC source with maximum voltage and current limits and with near-deadbeat regulation. CPM control of a full-bridge boost inverter and nonlinear carrier-control of a buck converter are presented as new methods of producing constant power source AC outputs.

Analysis and small-signal models contained herein demonstrate the efficacy of the proposed constant power control schemes, showing that major sources of non-idealities include peak-to-average error, artificial ramp-induced error, and transient error. The nonlinear carrier-

controlled buck power source exhibits a transient error dependent on the size of the inductor, while the CPM controlled boost power source transient error is independent of the inductor size.

A prototype ESG employing CPM control generates the ideal output characteristic and achieves near-deadbeat regulation of output power. Maximum voltage- and current-limits are invoked equally quickly. The standard deviation in per-cycle output power during arc cutting is less than 2%, compared to greater than 25% in the prior art. Histological analysis of *ex vivo* tissue samples shows a marked decrease in collateral tissue damage, proving a previously-unknown correlation between high-speed output power regulation and thermally-induced tissue necrosis.

Simultaneous control of multiple converter stages in the prototype demonstrates the ability to achieve high peak output voltages with low average power using a continuous output carrier: a significant simplification over the prior art.

*To my parents*

*To Daphne*

# Acknowledgements

I would like to thank Mr. Jim Gilbert and colleagues at Covidien for their generous support and assistance in completing this work.

I would also like to thank my advisor, Professor Robert Erickson, for his invaluable advice and guidance, and for his immeasurable patience and good humor.

Special thanks to Dr. Maranke Koster for preparation of histology samples.

# Contents

## Chapter 1 - Introduction



## Chapter 2 - Realization of the Ideal ESG Output Characteristic

## Chapter 5 – Realizing Non-Cutting Waveforms with Continuous Outputs



## Chapter 6 – Conclusions

# List of Tables

# List of Figures

# CHAPTER 1

# INTRODUCTION

## 1.1 – Principles of Electrosurgery

Electrosurgery is the use of a high-frequency AC current to cause heating of human or animal tissue to achieve desirable clinical effects such as cutting, coagulation (stopping the flow of blood), fulguration (vaporizing tissue with arcs), or desiccation (dehydration) [1]. Electrosurgery is a prominent tool in the modern operating room, finding use in 80% of surgical procedures performed in the United States. The importance of this application can be judged by the size of the market for ESGs and associated disposables, which is in excess of $1Bn per annum [2, 3].

A device known as an electrosurgical generator ("ESG") supplies high-frequency current to an instrument held by the surgeon. As the instrument contacts the tissue of interest, the flow of current causes $I^2R$ heating: the dominant physical mechanism which causes electrosurgical effects [4]. As the intracellular temperature rises, different clinical effects are observed depending on the final temperature and the length of the time interval over which heating occurs. When intracellular temperatures reach 45°C, thermal denaturation of proteins occurs, leaving what is known as a "white coagulum", or tissue that has been heated until blanched, but not charred. If temperatures rise to 90°C over a long time interval, boiling water vapor within the cell

can exit the cell wall in an orderly manner, causing desiccation of tissue. If the temperature of 90°C is reached quickly, however, expanding water vapor causes the cell wall to burst, creating a cutting effect [5]. If temperatures reach 200°C, sufficient energy exists to break intramolecular bonds between the constituent carbon atoms that comprise living matter, reducing remaining cellular solids to elemental carbon – this is known as "black coagulum", or charring of tissue [6]. Such different tissue effects are desirable in different surgical situations, and this variety of outcomes contributes to the versatility of electrosurgery. Note that electrosurgery is significantly different from electrocautery, which refers to resistance heating of a surgical instrument that causes tissue damage through heat conduction, rather than direct generation of heat by electrical conduction (as occurs in electrosurgery) [7].

Experimentation with electrosurgery began over 100 years ago, when d'Arsonval first observed that a sufficiently high frequency current (>10 kHz) could pass through tissue without causing muscle stimulation [8]. By the mid-1920s, several commercially-available ESGs were marketed, using a combination of vacuum tube oscillators and spark gaps. By 1970, solid-state devices were able to replicate the desirable effects produced by the spark gap, and the industry concentrated heavily on ESGs with resonant inverter output stages. As recently as 1990, manufacturers were still producing ESGs with unregulated outputs. Today, resonant inverters are still prevalent, and most ESGs perform some regulation of output voltage or power [9].

Electrosurgical applications are broadly categorized as "monopolar" or "bipolar". In bipolar applications, the surgeon's instrument is shaped like a tweezers or hemostat, and contains both a source and return electrode. Bipolar instruments are often used for sutureless vessel sealing, where mechanical pressure on the instrument combines with energy delivered by the ESG to thermally coagulate a vessel shut. In monopolar electrosurgery, the surgeon's instrument

is a blunt conductive pencil which serves as the source electrode, and the patient is attached to a large return (or “dispersive”) electrode to complete the circuit, as illustrated in Fig. 1.1.

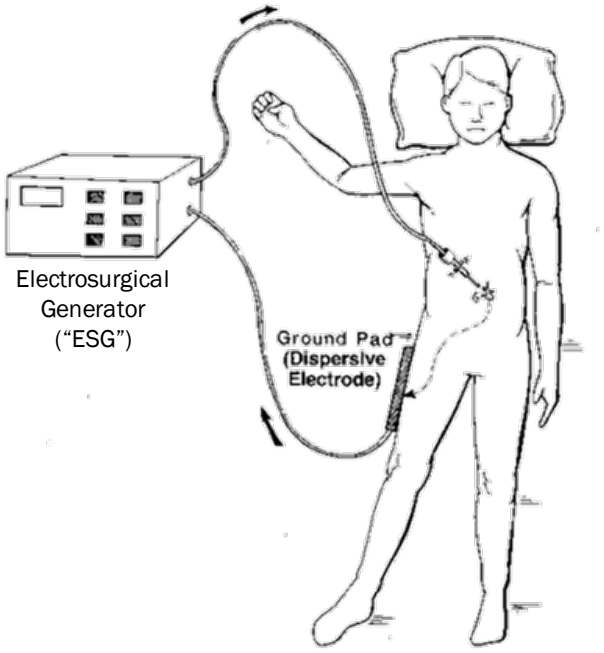


Fig. 1.1 – Use of monopolar electrosurgery

*Illustration courtesy Covidien*

Since the surgeon’s instrument has a much smaller surface area than the return electrode, clinically significant current density is only experienced by the tissue immediately adjacent to the instrument. As the current flows through the patient and into the large return electrode, current density decreases to a level that causes no tissue effects for reasonable exposure levels. This disparity between the size of the source and return electrode in monopolar electrosurgery effectively localizes the tissue effects to the tip of the surgical instrument.

Relative to a cold scalpel, electrosurgery offers numerous advantages to the surgeon. Perhaps most significantly, electrosurgery can simultaneously cut tissue and affect hemostasis

(sealing of bleeding blood vessels) [10]. As current flows, the tissue directly contacting the instrument tip experiences sufficient current density to cause vaporization - the few adjacent cell layers experience a decreased current density only sufficient to thermally coagulate bleeding vessels. This dual-purpose effect represents an enormous time savings to the surgeon, maintains a clean surgical field, and minimizes patient blood loss. Additionally, electrosurgery maintains a relatively constant cutting speed and drag force (friction between the instrument and tissue), which improves controllability [9]. Finally, electrosurgery is required for many laparoscopic procedures, where it would be difficult or impossible to articulate a cold scalpel through a small opening to a distant surgical site.

The significance of the advantages imparted by electrosurgery cannot be understated. In fact, John A. Pearce, a noted expert on electrosurgery, writes that, “Many of the delicate neurosurgical techniques would be impossible without electrosurgery – and it is likely that open heart surgery and much of urologic surgery would likewise not be carried out [in the absence of electrosurgery]” [8].

## 1.2 – Tissue Characteristics

The apparent electrical impedance of tissue to high-frequency current varies significantly depending on the tissue composition and the manner in which the electrosurgical instrument is being used. Figure 1.2 shows ranges of impedance encountered for different tissue types, demonstrating a total range from approximately 0 Ω to approximately 4 kΩ [6].

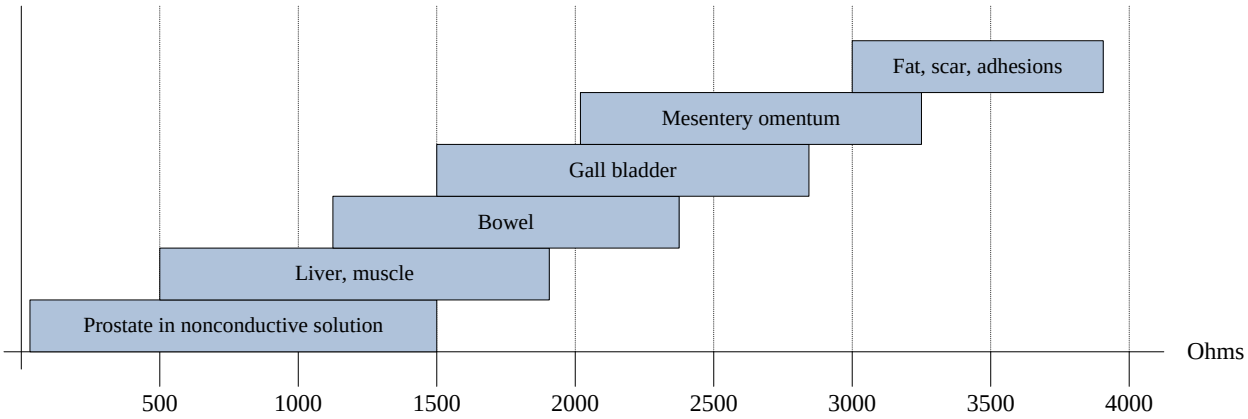


Fig. 1.2 – Impedances of various tissue types

In addition to exhibiting a tissue-type-dependent variation in impedance, tissue of the same type presents varying impedance as it heats, dehydrates, and is vaporized. Figure 1.3 shows the average per-cycle impedance of muscle tissue during arc cutting.

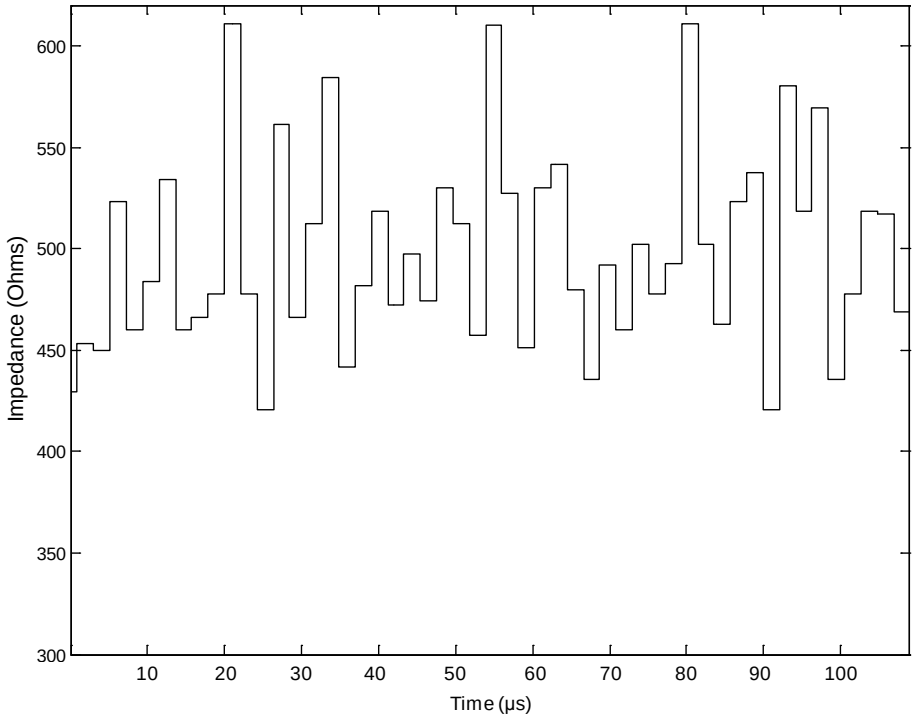


Fig. 1.3 – Average per-cycle impedance during arc cutting of muscle tissue

While Fig. 1.3 shows significant (>200 Ω) variations in impedance between adjacent cycles, transitions between different tissue types (such as muscle tissue heavily striated with fat deposits or scarring) would exhibit even greater variation in impedance.

While the electrical impedance of tissue varies widely, the thermal characteristics are more consistent. Figure 1.4 shows the thermal conductivity of several tissue types, as well as copper, water, and air, as points of comparison, and Fig. 1.5 shows the volumetric heat capacity of the same [11]. The thermal conductivity of tissue is relatively constant, suggesting that heat gained by tissue is then lost at a uniform rate (although given the fast rate of heating occurring in electrosurgery, thermal diffusion may be insignificant in any tissue type [12]). The volumetric heat capacity of tissue is also relatively constant, suggesting that a quantum of energy will cause

an equal temperature rise in any tissue type. Note that volumetric heat capacity is a more appropriate measurement than specific heat, as specific heat describes heat gain per unit mass, while the electrosurgical instrument will be in contact with a unit volume of tissue.

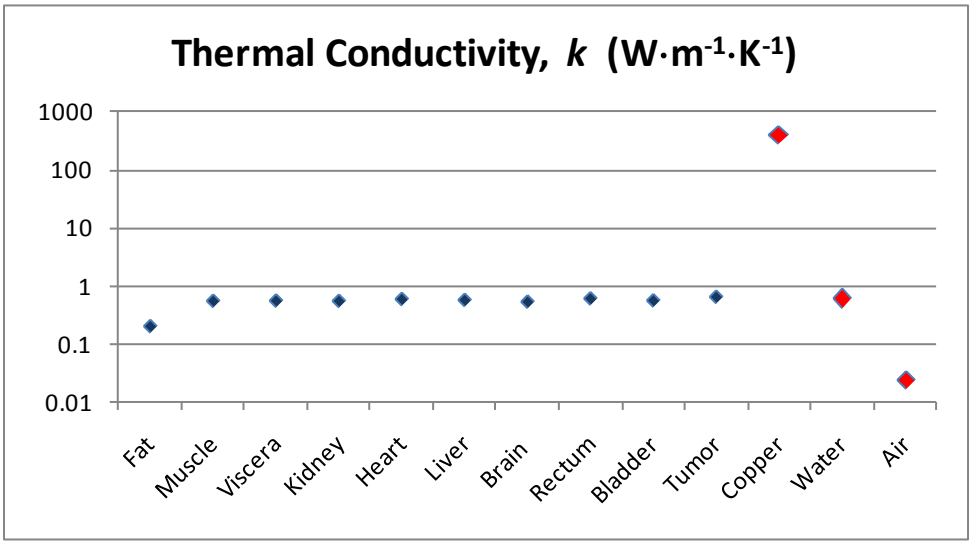


Fig. 1.4 – Thermal conductivity of various tissue types and points of comparison

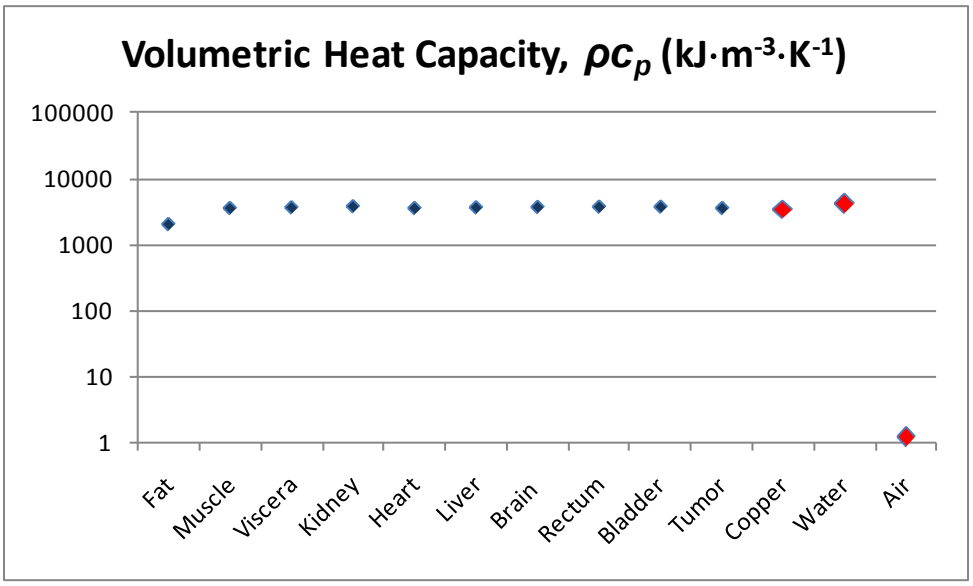


Fig. 1.5 – Volumetric heat capacity of various tissue types and points of comparison

## 1.3 – Desired Output Characteristic

Given that the fundamental physical mechanism underlying electrosurgery is $I^2R$ heating, and observing the wide range of electrical impedance but relatively constant thermal capacity and conductivity, it becomes clear that to obtain a uniform rate of heating, a constant power source output characteristic is desired from the ESG. Practically, an ESG must be limited to some maximum output voltage and current. Additionally, at power levels commonly encountered in electrosurgery, the maximum voltage developed at high impedance loads may be several hundreds of volts, which can cause significant arcing between the tip of the instrument and the patient. This arcing effectively decreases the surface area of the instrument, increasing the current density experienced by some tissue, and increases the likelihood of developing unwanted carbonization at that site. Thus, regulation of maximum output voltage is also critically important to achieve the desired tissue effect. Figure 1.6 shows the ideal ESG output characteristic as an *(i ,v)* plot.

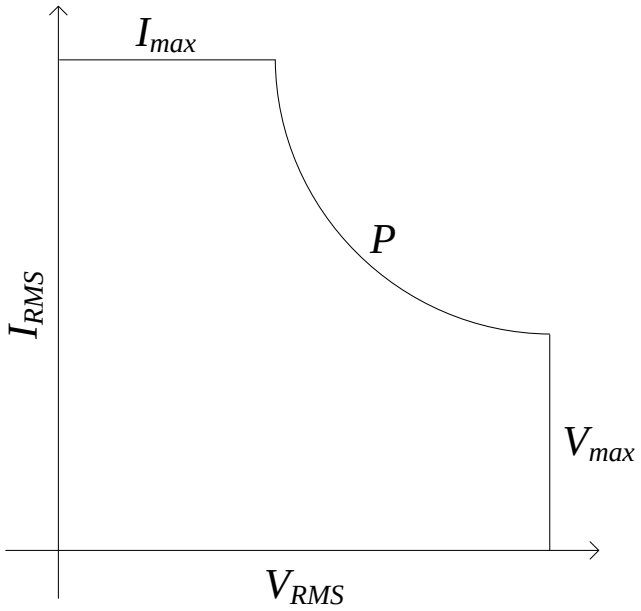


Fig. 1.6 – Desired output characteristic of an ESG

## 1.4 – Prior Art

Most commercially-available ESGs use a resonant inverter to realize the desired output characteristic. The resonant inverter has an elliptical equilibrium output characteristic [13, 14] which reasonably approximates the desired output characteristic (shown in Fig. 1.6), as it tends to behave as a current source at low impedances and as a voltage source at high impedances. At mid-range impedances, where the vast majority of tissue lies, there is significant error between the delivered power and the desired (hyperbolic) constant-power curve, as shown in Fig. 1.7.

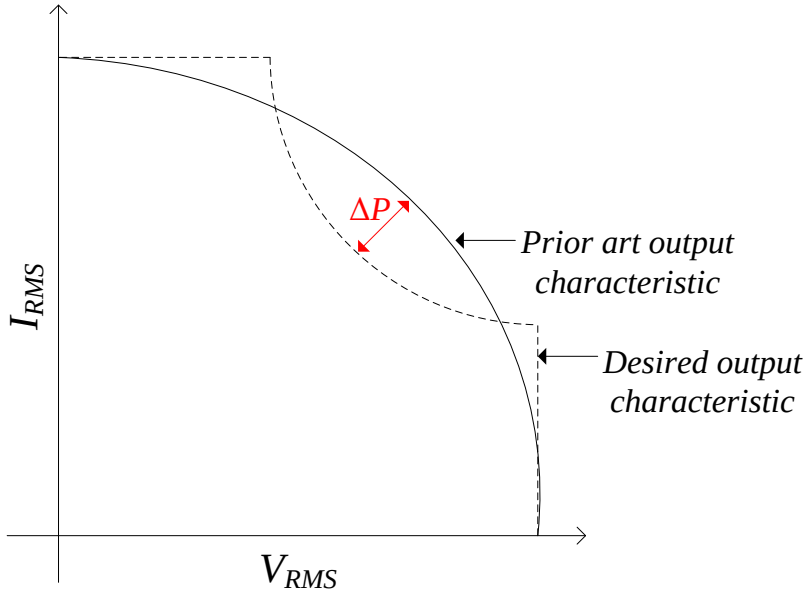


Fig. 1.7 – Prior-art output characteristic compared to desired output characteristic

While the steady-state output of the resonant inverter exhibits the error illustrated in Fig. 1.7, resonant inverters also experience ringing during transients which cause significant deviation in both output voltage and current from the equilibrium output curve [32]. Thus, during transients, the delivered output power varies even more significantly than shown in Fig. 1.7. The combined

transient and steady-state errors result in resonant inverter-based ESGs having frequent and significant deviation from the requested power level.

To improve compliance between requested and delivered power, manufacturers have added closed-loop control systems to resonant inverter-based ESGs, as shown in Fig. 1.8.

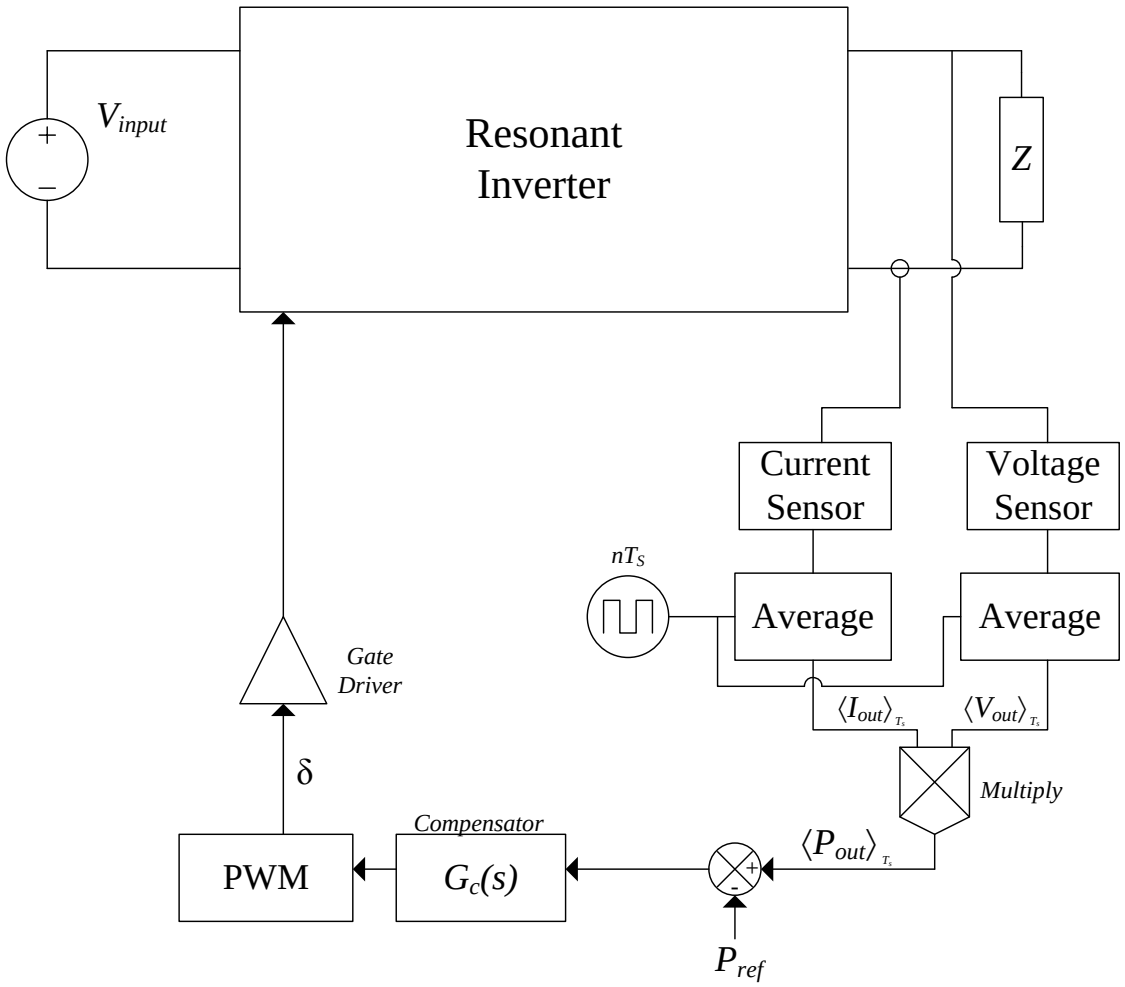


Fig. 1.8 – Resonant inverter-based ESG with closed-loop power regulation

Sensors on the output of the ESG measure the magnitudes of the output voltage and current. Since the output is AC, these measurements need to be taken over a full output cycle (in practice, electrical noise forces the averaging of measurements from many tens or hundreds of

cycles to obtain useful data). The averaged values of output voltage and current magnitude are then multiplied to determine the average output power, which is compared to the desired output power, and the error between requested and delivered power is fed to a compensator network, which signals a pulse-width-modulator to change the control signal given to the resonant inverter, which results in a change in the size of the output ellipse. This process is illustrated in Fig. 1.9.

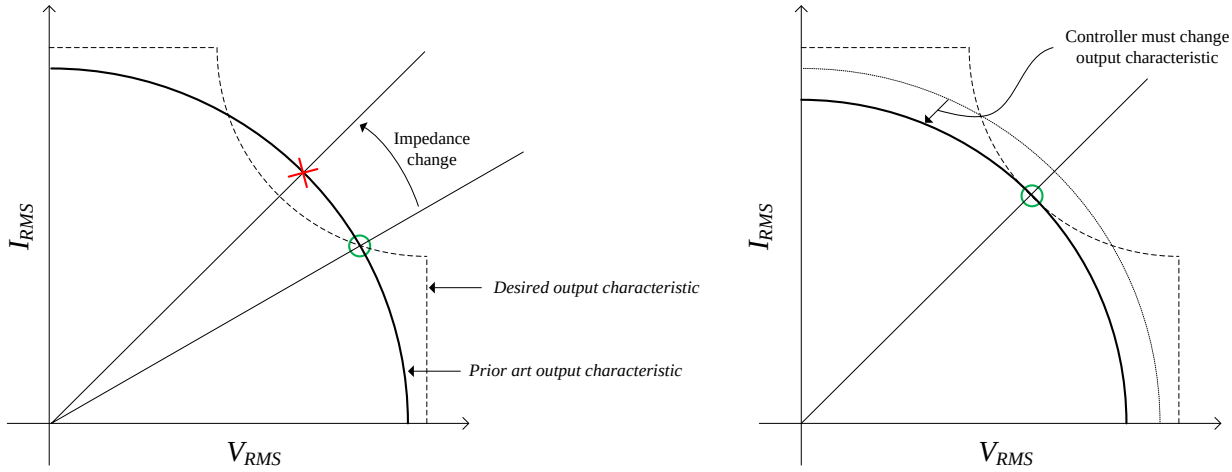


Fig. 1.9 – Regulation of output power in resonant-output converter

The design of the ESG of Fig. 1.8 is somewhat simplified. Some commercially-available ESGs further complicate the power stage by switching the resonant inverter at a fixed frequency and attempting to regulate output power by varying the DC input voltage via an upstream DC/DC converter. This introduces additional dynamics in the transient response, even further degrading transient performance.

Because of the need to measure many tens or hundreds of output cycles, along with the typically slow dynamics of the control loop and resonant inverter (and potential upstream DC/DC converter), the speed of the entire control system is often orders-of-magnitude slower

than the inverter AC output, with total control loop bandwidths often being less than 1 kHz (in a 500 kHz inverter). Figure 1.10 shows the response of a resonant inverter-based ESG to a step in load impedance, demonstrating the presence of a low-speed control loop.

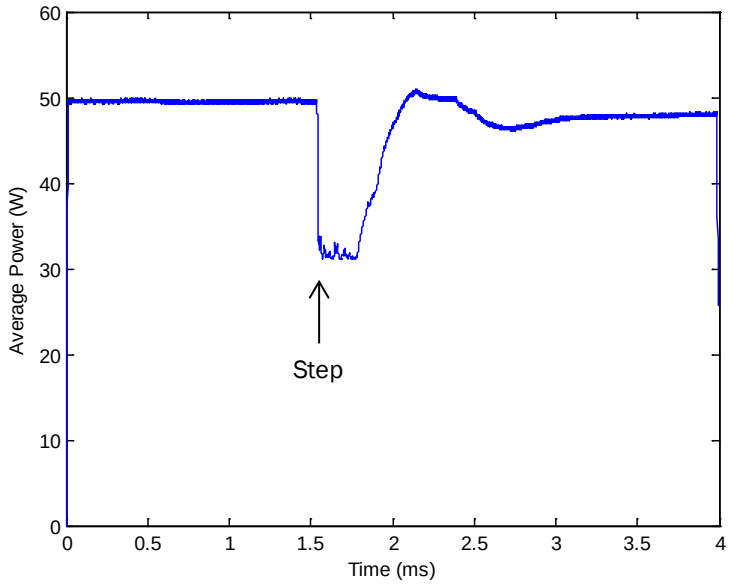


Fig. 1.10 – Transient response of resonant inverter-based ESG

In Fig. 1.10, a step change in load impedance occurs at the center of the plot, and the ESG takes ~2 ms, or about 1,000 cycles, to achieve regulation of output power. While the step response of Fig. 1.10 results in a ~40% undershoot in output power, load steps in the opposite direction result in a commensurate overshoot in output power, which causes undesirable heating and/or charring of tissue.

## 1.5 – Motivation

The use of this slow, low-bandwidth control system results in the desired output power not being delivered in each cycle. While the average power delivered over many thousands of cycles may be correct, any individual AC output cycle is unlikely to accurately deliver the requested output power. Figure 1.11 shows a histogram of the power delivered in each output cycle from a popular, state-of-the-art ESG employing a resonant output stage and control loop, as previously described. While the power requested (50 W) was correct when averaged over several thousand output cycles, the standard deviation in power delivered by any individual output cycle was 13 W, with some cycles delivering in excess of 120 W.

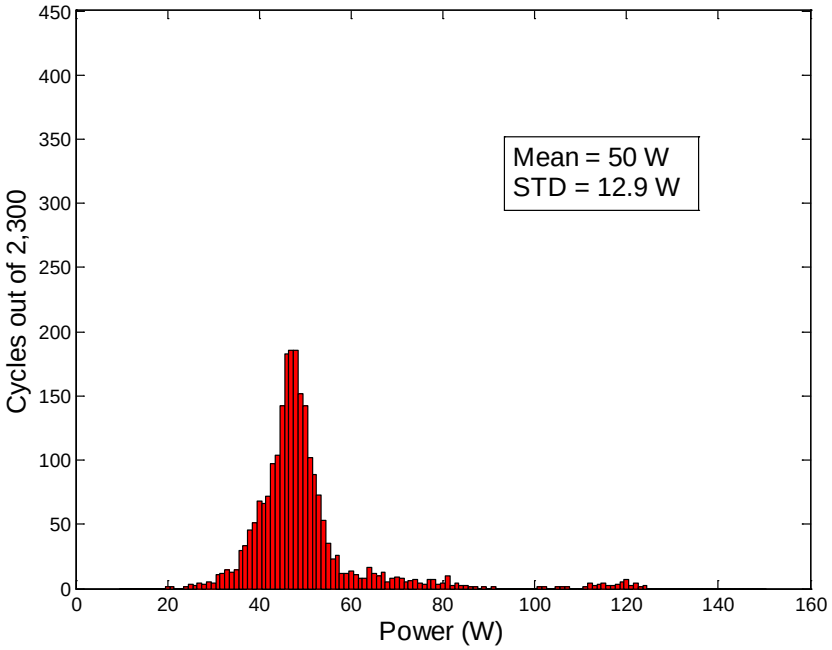


Fig. 1.11 – Histogram of cycle-by-cycle output power

The clinical implications of this error are significant. Excessive power delivery leads to increased thermal spread. Variation in delivered power causes inconsistent speed of cutting and drag force.

Excessive peak voltages lead to undesirable tissue carbonization (charring), as shown in Fig. 1.12, where human tissue analogs were dissected using the same average power, but different peak voltages. Parameters such as depth of cut, thermal margins, and presence of carbonization are all directly affected by output power regulation and peak output voltage.

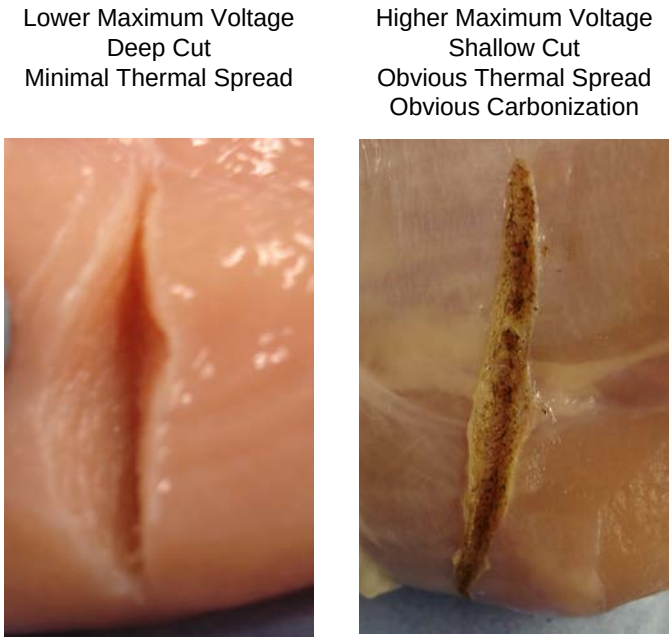


Fig. 1.12 – Dissection of human tissue analogs

Thus, it is clear that improvement in the performance of ESGs can be realized by improving cycle-by-cycle compliance between the requested and desired output power.

## 1.6 – Objectives and Outline

The object of this work is to improve the transient response of ESGs, simplify the system architecture, and offer a greater variety of functions and clinical effects. Specifically, CPM-based control schemes are explored as a means to achieve all of these outcomes.

Chapter 2 develops CPM-based converters and control systems capable of realizing the ideal ESG output characteristic with near-deadbeat response. It is shown that the ideal ESG output characteristic is realized using a buck converter series connected to a boost inverter, with a CPM control system that employs fixed duty cycles, fixed control current limits, and a nonlinear control current limit.

Chapter 3 models the constant power sources developed in Chapter 2, to assess causes of non-idealities. Expressions are derived for both steady-state and transient errors, revealing which parameter values most affect the ideality of the constant power sources. Small-signal models used to predict transient errors are experimentally verified.

Chapter 4 presents a prototype of the proposed system architecture, and compares the results to the prior-art. It is shown that the prototype exhibits improved transient response and a simpler system architecture. Additionally, tissue analysis demonstrates an improved clinical effect.

Chapter 5 shows a method of extending the functionality of the prototype to achieve a greater variety of clinical effects using the same converter and control system.

Finally, Chapter 6 provides conclusions and gives a summary of how the stated objectives are met.

## 1.7 – Review of Power Electronics Concepts

This section briefly reviews several power electronics concepts employed in this thesis. Basic explanations are provided for the buck converter, boost inverter, current-programmed mode ("CPM") control, nonlinear carrier-control, and averaged switch modeling.

This thesis discusses two basic power converters. The *buck* converter, shown schematically in Fig. 1.13, reduces a fixed DC input voltage ($V_g$) to a lower DC output voltage ($V$). It achieves this by switching a transistor with a waveform, δ, as shown in Fig. 1.14.

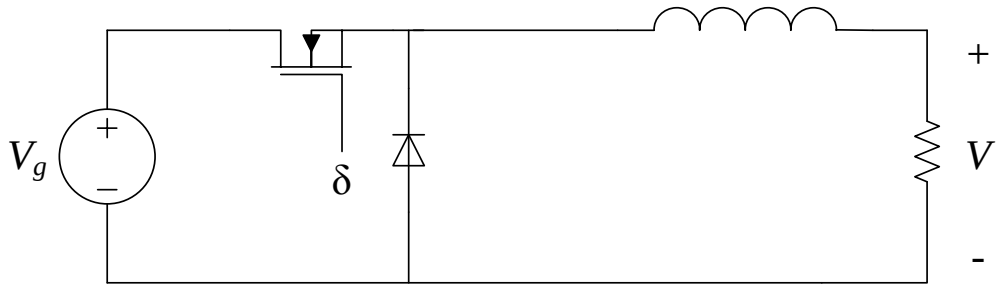


Fig. 1.13 – Buck converter

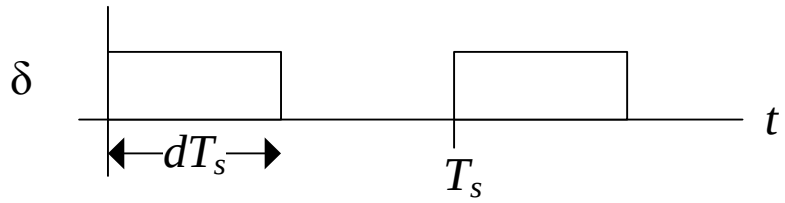


Fig. 1.14 – Buck converter switching waveform

The duty ratio of δ is defined as *d*, and this duty ratio relates the output voltage (*V*) to the input voltage ($V_g$) as given by (1.1).

$$V = \frac{1}{T_s}\int_0^{T_s} v(t)dt = d \cdot V_g \tag{1.1}$$

Thus, if *d* is 0%, the output voltage is zero volts, and if *d* is 100%, the output voltage is $V_g$. Between these limits, the output voltage is the fraction of $V_g$ given by *d*. The duty cycle of any power converter is also often expressed in terms of its complement, denoted *d′*, where *d′*=1-*d*.

The *boost* inverter, shown schematically in Fig. 1.15, performs the opposite function of the buck converter by increasing the magnitude of a DC input voltage, and performs the additional function of inverting the output voltage to deliver an AC (rather than DC) output.

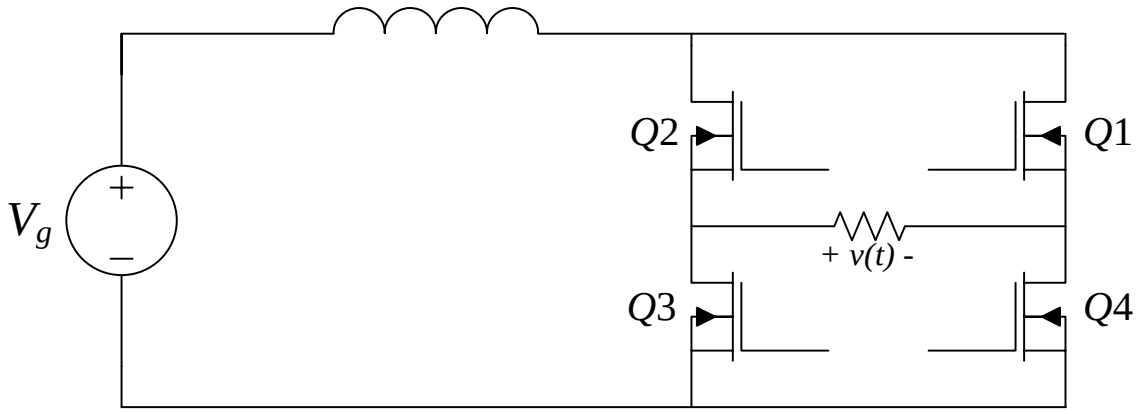


Fig. 1.15 – Boost inverter

While the buck converter contains a single transistor, the boost inverter contains four. A signal, δ, switches the four transistors in a specific pattern, and the duty ratio of δ is again *d*. The switching pattern employed is shown in Fig. 1.16. Figure 1.17 shows a typical method of realizing the switching waveforms of Fig. 1.16.

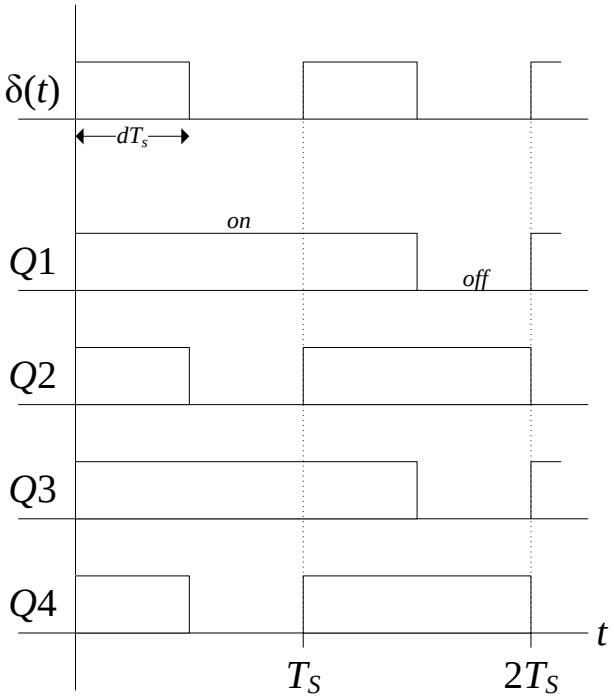


Fig. 1.16 – Switching pattern for transistors in boost inverter

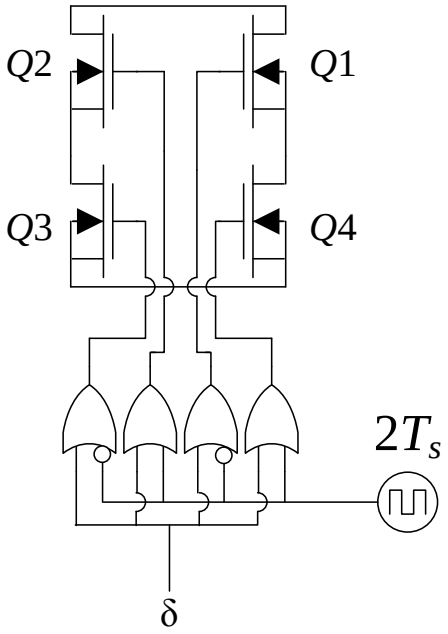


Fig. 1.17 – Hardware realization of switching pattern of Fig. 1.16

Larger values of *d* result in higher output voltages. The peak output voltage of the boost inverter is given by (1.2), and the RMS output voltage is (1.3). The switching waveform and output voltage produced by the boost inverter are shown in Fig. 1.18.

$$V_{PK} = \frac{V_g}{(1-d)} \tag{1.2}$$

$$V_{RMS} = \frac{V_g}{\sqrt{1-d}} \tag{1.3}$$

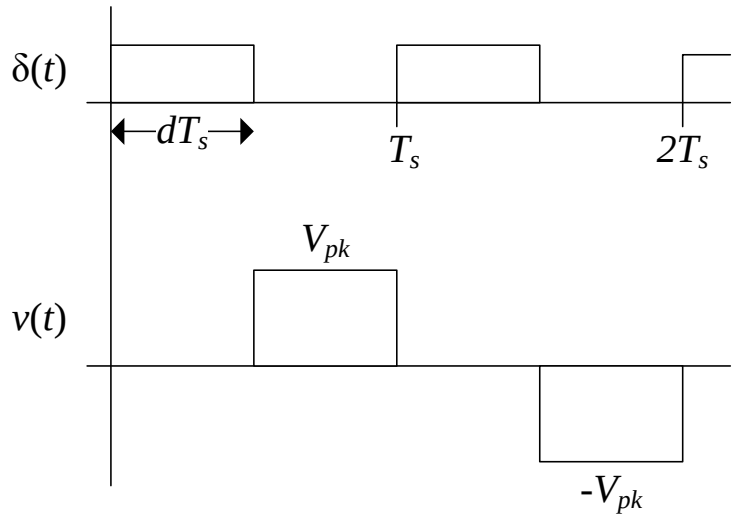


Fig. 1.18 – Boost inverter switching waveform and output voltage waveform

This thesis makes use of a power electronics control concept known as *current-programmed mode* ("CPM") control. CPM control refers to a method of regulating a current of interest in a power converter. In this thesis *CPM control* exclusively refers to peak current-

programmed mode control of an inductor current. By measuring an inductor current ($i_L(t)$) and comparing its peak value to a known limit ($i_C$), the switching waveform ($\delta$) for a power converter is determined, as illustrated in Fig. 1.19.

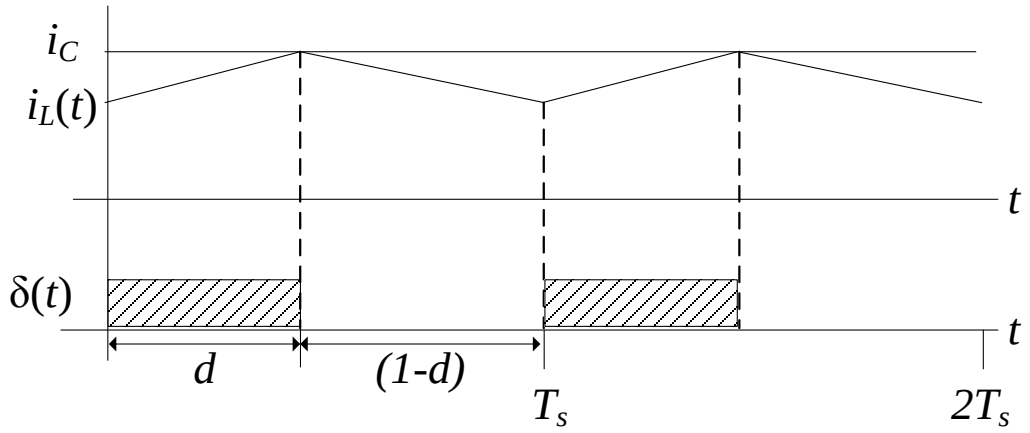


Fig. 1.19 – Waveforms in CPM control

In the waveforms shown in Fig. 1.19, small inductor current ripple results in the average value of the inductor current being approximately equal to the control current limit. As the magnitude of the inductor current ripple increases, so does the difference between the average value of $i_L(t)$ and the value of $i_C$.

A simple method of realizing a CPM controller is illustrated in Fig. 1.20.

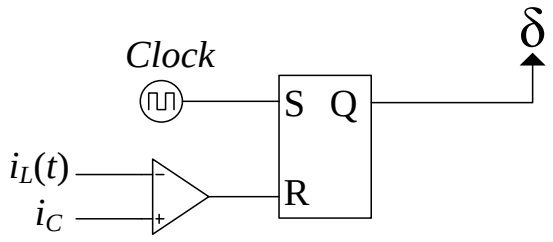


Fig. 1.20 – Realization of CPM controller

In Fig. 1.20, an S/R latch generates the switching waveform δ. A periodic clock provides the *set* input, initiating the *d* interval. A comparator resets the latch once the inductor current value exceeds the control current limit, ending the *d* interval.

CPM control is known to be unstable for duty cycles greater than 50% [22]. Figure 1.21 illustrates how attempts to operate at duty cycles greater than 50% fail to establish a stable operating point as a result of the geometry of the inductor current waveform.

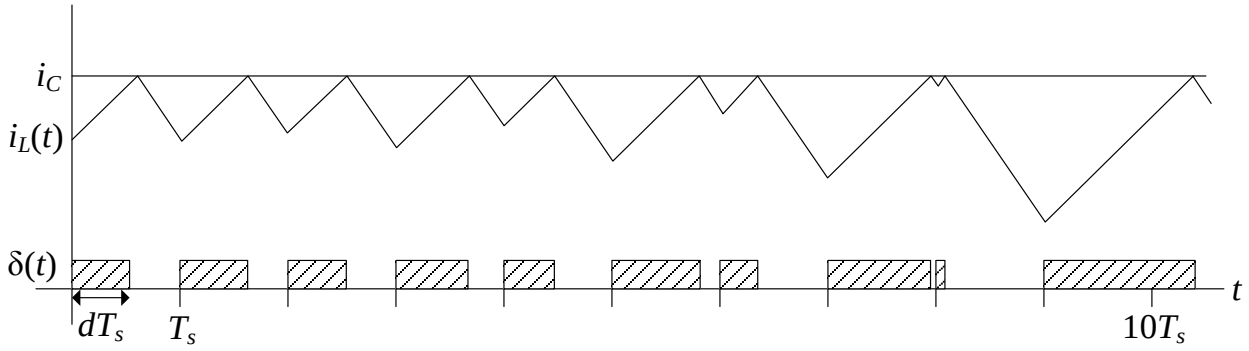


Fig. 1.21 – CPM control waveforms showing instability

Addition of an artificial compensating ramp to the sensed inductor current (or, equivalently, subtraction of an artificial compensating ramp from the control current limit) can stabilize the converter for operation at duty cycles greater than 50%. Figure 1.22 illustrates this.

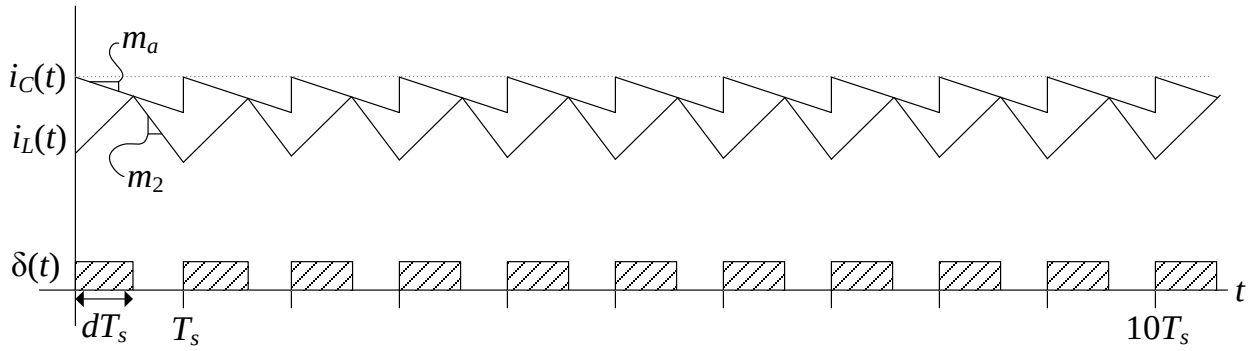


Fig. 1.22 – CPM controller stabilized by addition of artificial ramp

The minimum slope of the artificial ramp ($m_a$) necessary to establish stability is a function of the inductor current slope during the $d'$ interval ($m_2$), as given in (1.4).

$$m_{a,\min} = \frac{1}{2} m_2 \tag{1.4}$$

Figure 1.22 employs a linear artificial compensation ramp, but other waveshapes can be utilized to achieve different outcomes. For example, use of a judiciously selected nonlinear compensation ramp allows a converter to emulate a constant power sink [17, 18], which finds use in power factor correctors. Use of a nonlinear artificial compensation ramp is termed *nonlinear carrier-control*. Figure 1.23 illustrates typical waveforms encountered in nonlinear carrier-control.

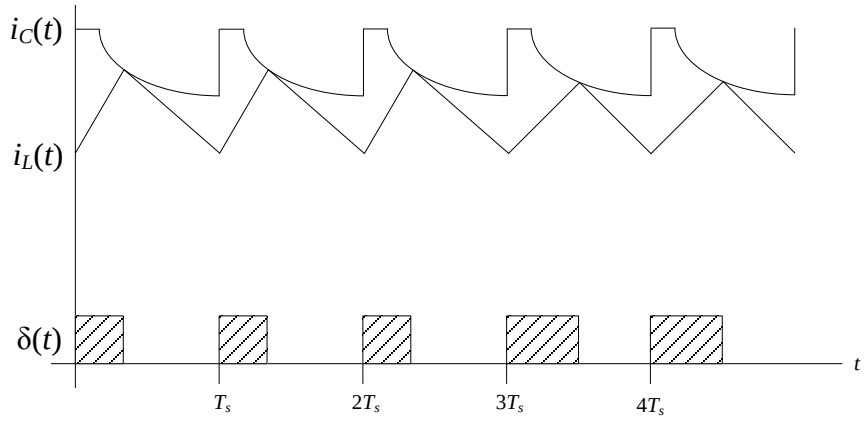


Fig. 1.23 – Typical waveforms in nonlinear carrier-control

When nonlinear carrier-control is used in a power factor corrector to emulate a constant power sink, the function describing the shape of the nonlinear carrier is chosen to cause the input port of the converter to emulate a resistive load. Judicious selection of the nonlinear carrier produces different desirable effects.

Finally, this thesis employs averaged switch modeling, where time-varying converter quantities are averaged over a full switching period to ascertain their low-frequency behavior. Angled brackets are used to denote this averaging step, as shown in (1.4).

$$\left\langle x(t)\right\rangle_{Ts} = \frac{1}{T_s}\int_0^{T_s} x(t)dt \tag{1.4}$$

# CHAPTER 2

# REALIZATION OF THE IDEAL ESG OUTPUT CHARACTERISTIC

Having established the shape of the ideal ESG output characteristic as a constant power source with voltage and current limits, this chapter proposes various converters and control systems as means to achieve this output characteristic, treating each of the three output regions (constant current, constant power, and constant voltage) separately. Emphasis is placed on designing systems that exhibit the potential for very high speed output power regulation, and utilize minimum parts.

A CPM buck converter is shown to produce a constant current DC source; when series connected to a full-bridge inverter, a constant current AC source is realized. CPM control of the full-bridge inverter realizes a constant power AC source, however, the dynamic range of this source is insufficient for the wide range of load impedances encountered in this application. A variation of CPM control of the buck converter, using a nonlinear carrier as the CPM control current limit, is presented as a means of producing a constant power source from a buck converter. When the CPM boost and nonlinear carrier buck are series connected, the dynamic range is ideal for use in electrosurgical applications. A constant voltage AC source is realized by limiting the duty cycle of the CPM controlled boost inverter, or by using a standard voltage-mode controller. Transitions between the four operating modes are achieved by observing duty cycle and employing a finite state machine, or by directly measuring the output quantities.

## 2.1 – Constant Current Output

It is known that CPM control of a buck converter produces a DC current source output characteristic [15]. This is physically intuitive, as the CPM controller attempts to vary the buck converter duty cycle to regulate the output current to a fixed value; to the extent that the controller is well-designed and inductor current ripple is low, it will realize a constant current source output. Figure 2.1 shows a CPM controlled buck converter series connected to a DC-AC boost inverter. By operating the DC-AC boost inverter at 0% duty cycle, the output is an AC current source with magnitude unchanged, as shown in Fig. 2.2. Thus, the desired AC constant current source is realized.

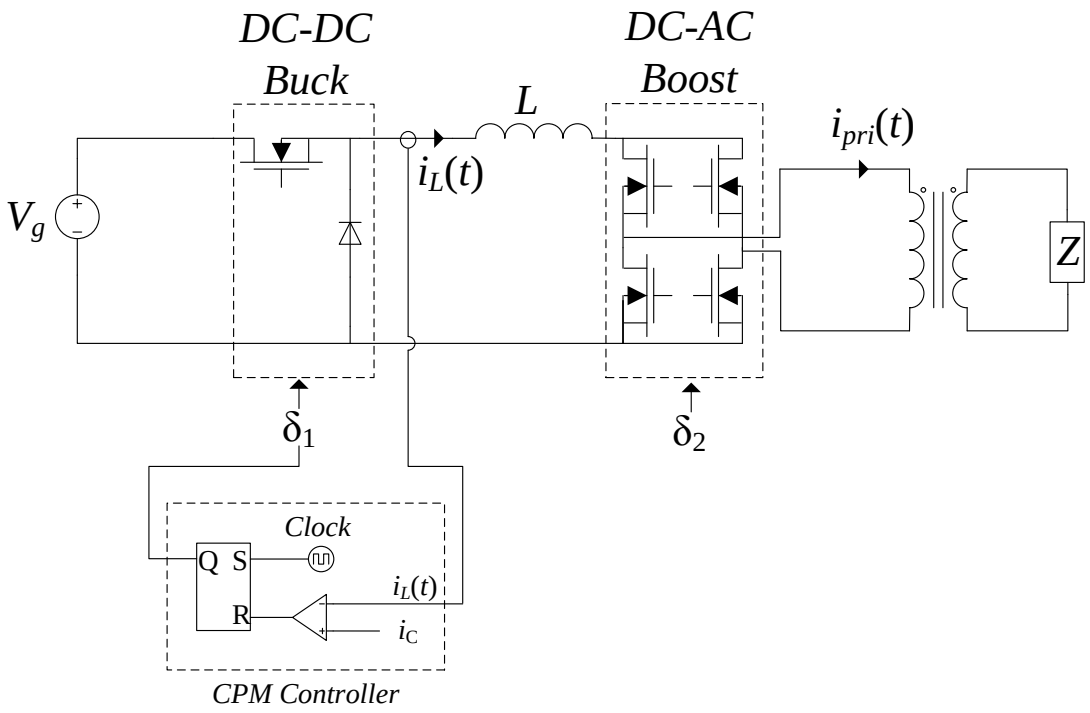


Fig. 2.1 – CPM controlled buck converter series connected to inverter

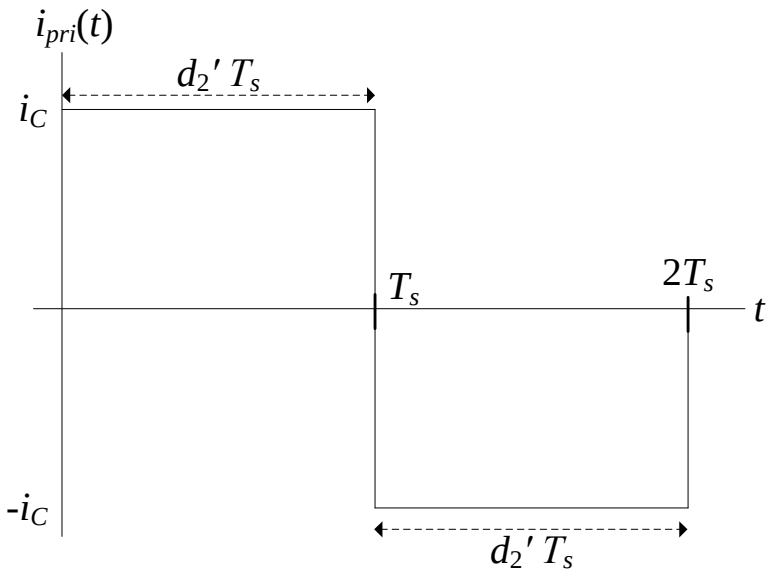


Fig. 2.2 – CPM buck output current waveform

Averaged switch modeling also demonstrates that the output of a CPM buck converter is a constant current source. Equation (2.1) lists the averaged expressions for the buck converter switch network terminal quantities identified in Fig. 2.3 and illustrated in Fig. 2.4.

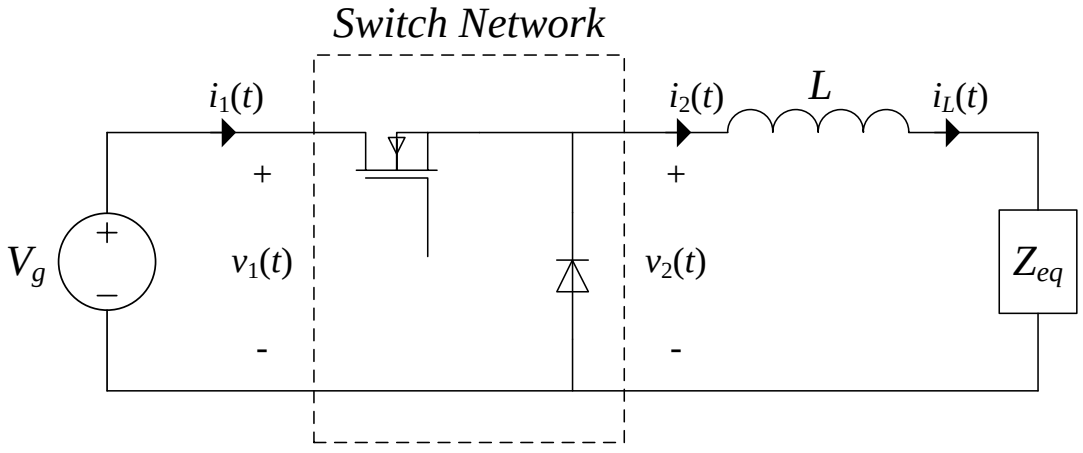


Fig. 2.3 – Switch network terminal quantities of buck converter identified

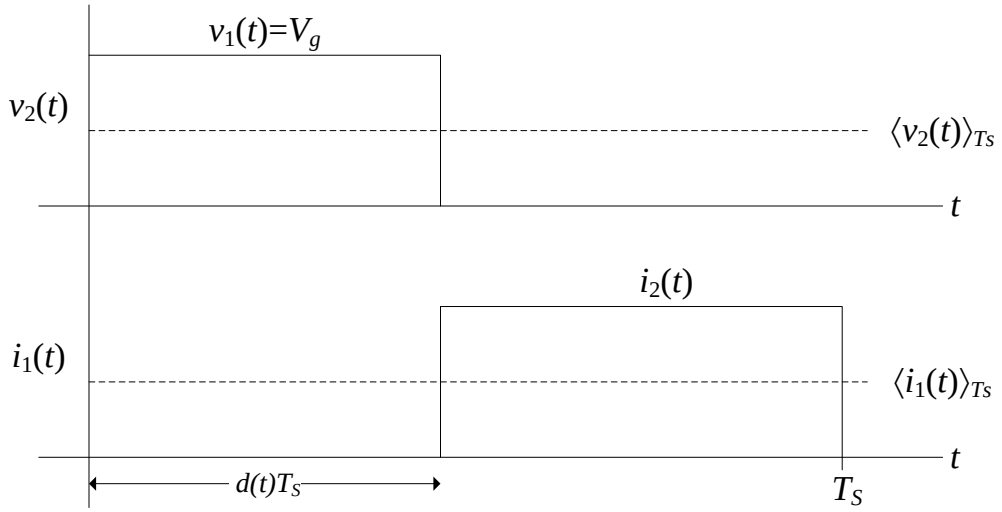


Fig. 2.4 – Example waveforms from circuit of Fig. 2.3

$$\begin{aligned} \left\langle i_1(t)\right\rangle_{Ts} &= d(t)\cdot\left\langle i_2(t)\right\rangle_{Ts} \\ \left\langle v_2(t)\right\rangle_{Ts} &= d(t)\cdot\left\langle v_1(t)\right\rangle_{Ts} \end{aligned} \tag{2.1}$$

The inductor current, $i_L(t)$, is the same as the switch network output current, $i_2(t)$, thus the average value of these quantities is the same. If the CPM controller successfully regulates the average inductor current to the average value specified by the control current limit, then:

$$\left\langle i_2(t)\right\rangle_{Ts} = \left\langle i_L(t)\right\rangle_{Ts} = \left\langle i_C(t)\right\rangle_{Ts} \tag{2.2}$$

Duty cycle can be eliminated from (2.1) to write (2.3).

$$\left\langle i_1(t)\right\rangle_{Ts} = \frac{\left\langle v_2(t)\right\rangle_{Ts}}{\left\langle v_1(t)\right\rangle_{Ts}}\cdot\left\langle i_2(t)\right\rangle_{Ts} \tag{2.3}$$

The value of $\left\langle i_2(t)\right\rangle_{Ts}$ can be substituted from (2.2) to write (2.4).

$$\left\langle i_C(t)\right\rangle_{Ts}\cdot\left\langle v_2(t)\right\rangle_{Ts} = \left\langle p(t)\right\rangle_{Ts} = \left\langle i_1(t)\right\rangle_{Ts}\cdot\left\langle v_1(t)\right\rangle_{Ts} \tag{2.4}$$

Equation (2.4) describes the terminal characteristics of the buck switch network in CPM control. The input port absorbs a fixed average power $\langle p(t) \rangle_{Ts}$, and for a fixed value of $\langle i_C(t) \rangle_{Ts}$, the CPM controller must vary the duty cycle such that the output voltage $\langle v_2(t) \rangle_{Ts}$ varies to deliver all input power to the load. Thus, the input port of the switch network behaves as a constant power sink, and the output port behaves as a constant current source, as shown in Fig. 2.5.

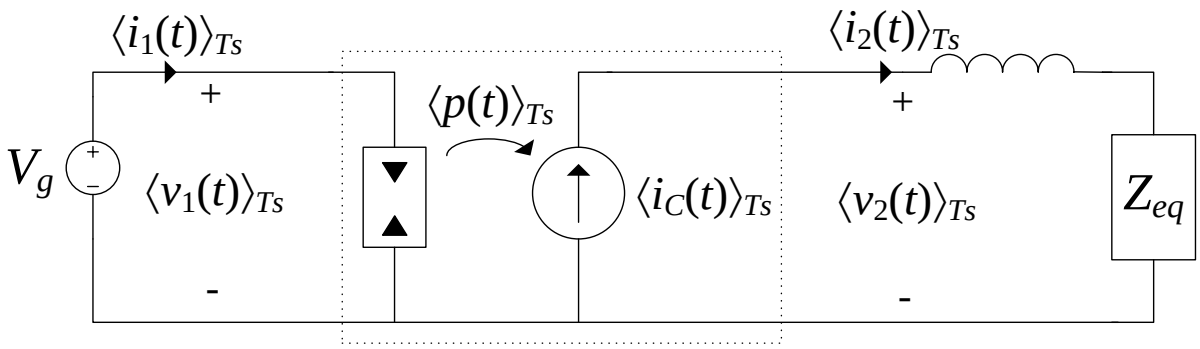


Fig. 2.5 – Averaged switch network derived from (2.4)

The model of Fig. 2.5 is idealized in several respects. Notably, inductor current ripple is ignored, and the inductor current only models the dominant low-frequency bandwidth limitations of the converter. Artificial ramp is also neglected, but could be modeled by a duty cycle-dependent variation in the value of the current source. Nonetheless, the model clearly illustrates that a constant current source is produced by CPM control of a buck converter.

## 2.2 – Constant Power Output from CPM Boost

It is known that CPM control of a DC-DC boost converter produces a DC power source output characteristic [16]. By extension, CPM control of a DC-AC boost inverter produces an AC power source output characteristic, where the waveforms of such a constant power AC source are illustrated in Fig. 2.6.

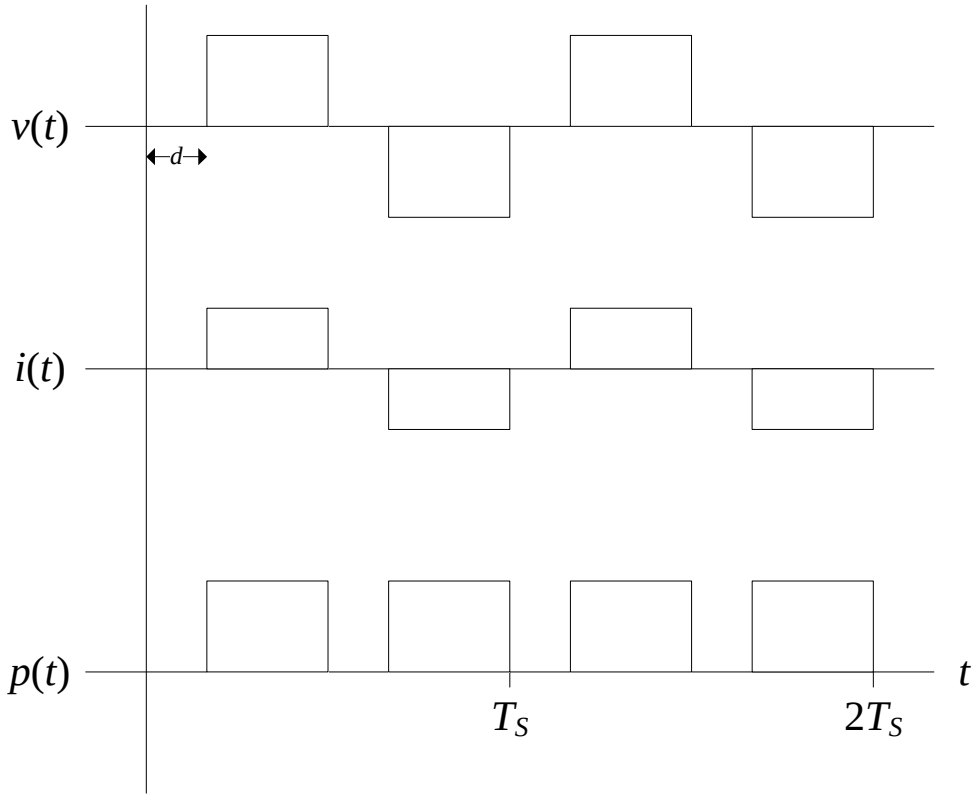


Fig. 2.6 – Waveforms in AC power source

In Fig. 2.6, voltage and current are square waves with variable duty cycle. Assuming a purely resistive load, no reactive power is present, and the output is a pulsating source of real power.

The production of such a constant power AC source from a CPM boost inverter is demonstrated by observing the switch network terminal quantities identified in Fig. 2.7.

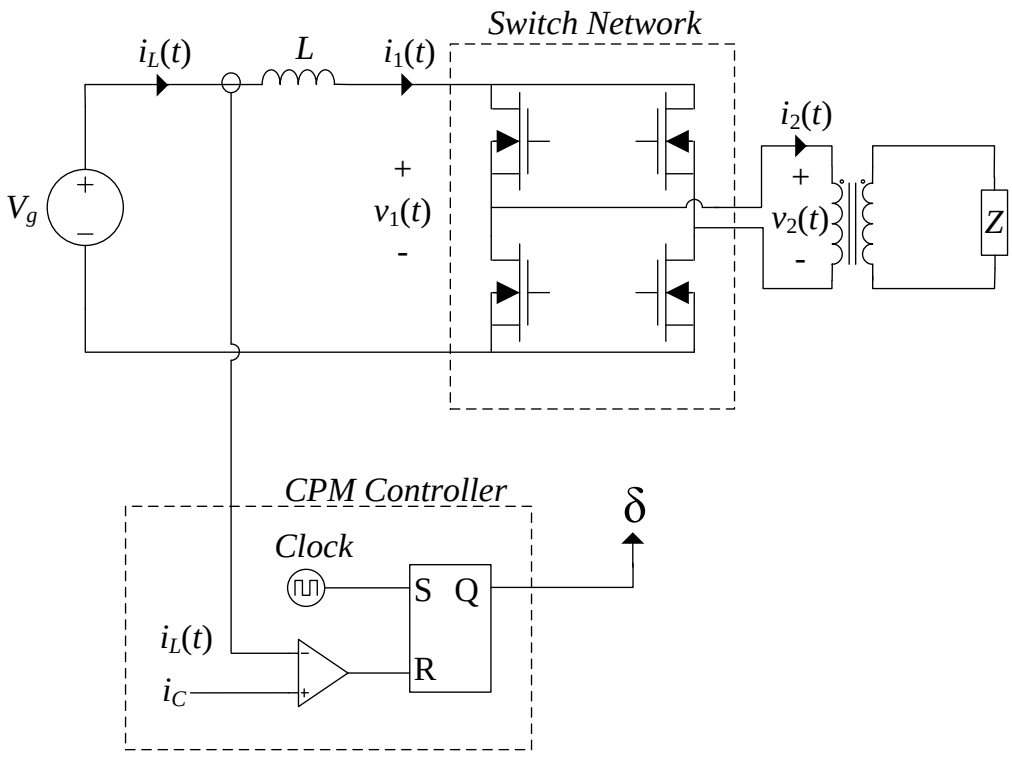


Fig. 2.7 – CPM controlled DC-AC boost inverter

The voltage into the switch network, $v_1(t)$, has a constant average value, as no average voltage can be applied across inductor $L$, and the input voltage, $V_g$, is fixed. Thus $\langle v_1(t) \rangle_{Ts} = V_g$.

To the extent that the CPM controller is well-designed and capable of regulating the inductor current, the input current to the switch network, $i_L(t)=i_1(t)$, is fixed and approximately equal to the control current limit, $i_C$. Thus, constant average voltage and constant average current are applied to the switch network of Fig 2.7, regardless of load, $Z$. The switch network absorbs a constant power, (2.5).

$$P_{in} = \langle i_1(t) \rangle_{Ts} \cdot \langle v_1(t) \rangle_{Ts} = i_C \cdot V_g \tag{2.5}$$

As the switch network contains no energy storage and is ideally lossless, all input power must be transferred to the output, resulting in the output being a constant power source, described by (2.6).

$$P_{in} = P_{out} = \left\langle v_2(t) \cdot i_2(t) \right\rangle_{Ts} \tag{2.6}$$

Thus, CPM control of a full-bridge boost inverter realizes a constant power AC source.

## 2.2.1 – Deficiency of Single-Stage Power Source

Typical specifications on an ESG require constant power output over the load range of 64 Ω to 4096 Ω for the nominal power setting of 50 W. As the lowest load impedance is relatively low (64 Ω), the input voltage ($V_g$) is also relatively low, as shown in Fig. 2.8.

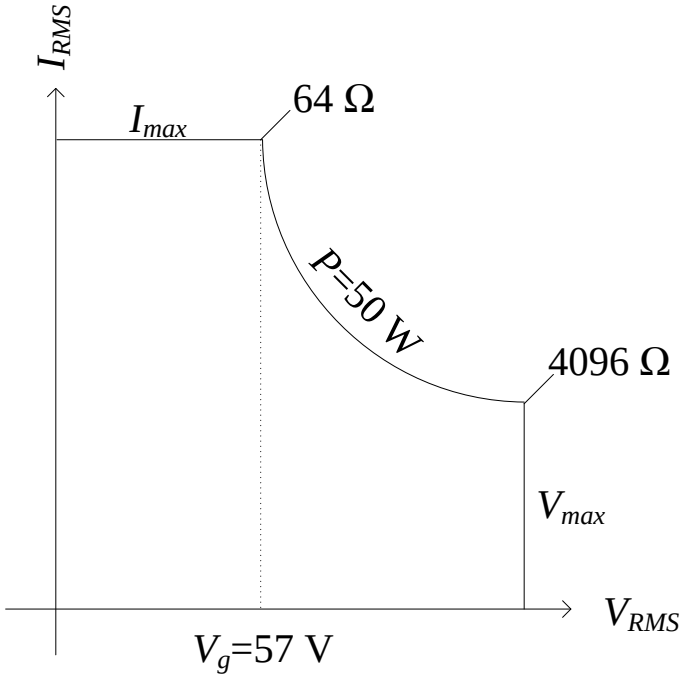


Fig. 2.8 – Typical ESG output specifications

To span the full range of desired load impedances, a single boost inverter would need to operate with a duty cycle between 0% and 98%. While it may be possible, although difficult, to design a boost inverter to achieve such high boost ratios, it would result in very high peak output voltages. Figure 2.9 shows this effect using the typical ESG specifications given in Fig. 2.8.

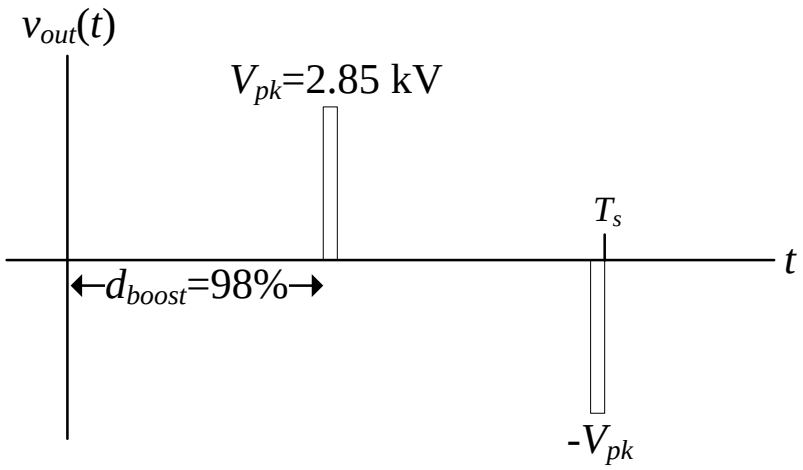


Fig. 2.9 – Output voltage of boost inverter at high load impedance

In addition to the obvious problem of designing the ESG, instruments, and leads to insulate against high peak voltages, high peak voltages also allow the formation of long arcs between the electrosurgical instrument and the patient. Such arcs effectively increase current density by decreasing the contact area between the instrument and tissue. This results in increased carbonization of tissue, and generally negatively affects other parameters of interest, such as thermal spread and depth of cut. Thus, even if a single-stage boost inverter could be designed for the specified range of load impedance, it would not be clinically useful, suggesting that alternative methods of producing a wide-range constant power source are required.

## 2.3 – Constant Power Output from CPM Buck

Given that a DC-DC buck converter is already required for the constant current output mode, it is valuable if this stage is also employed to produce a constant power source. This minimizes additional parts count, and serves the desired purpose of significantly increasing the constant power stage dynamic range.

To ascertain how a buck converter is adapted to produce a constant power source, consider the waveforms identified in Fig. 2.10.

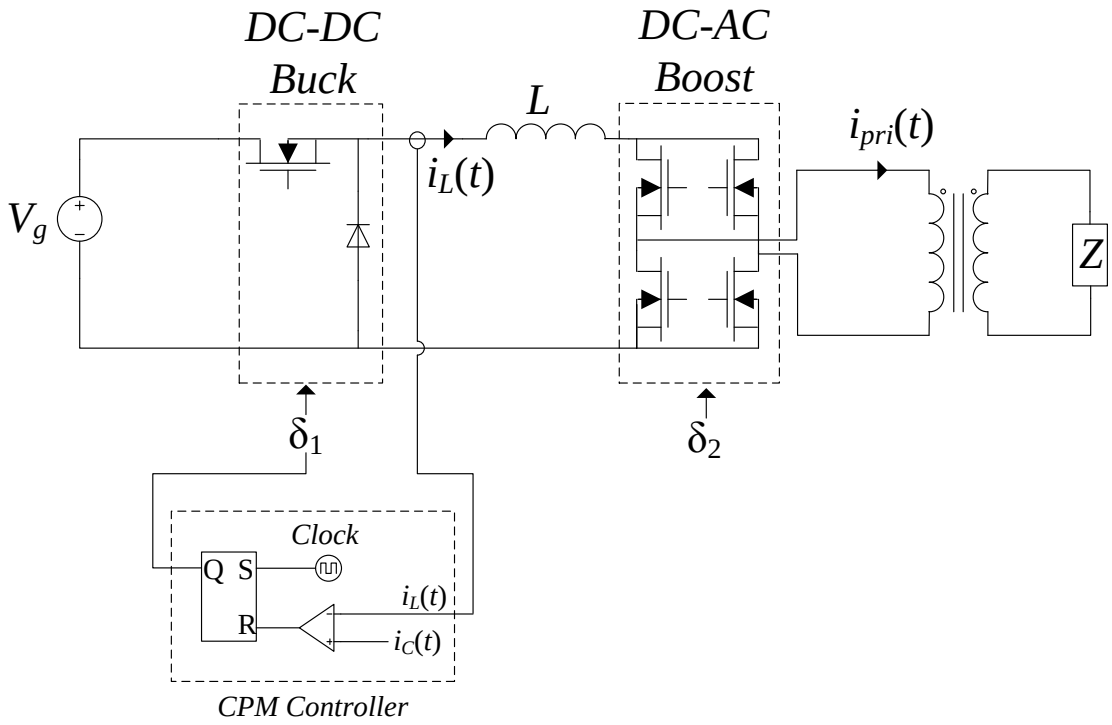


Fig 2.10 – Buck-based constant power source

Figure 2.10 shows a CPM controlled DC-DC buck converter series connected to full-bridge inverter: the same circuit used to realize a constant current AC source in Section 2.1. While Fig. 2.10 realizes a constant current AC source when the control current limit, $i_C(t)$, is a fixed value,

use of a nonlinear carrier as the control current limit results in the production of a constant power AC source. The value of said nonlinear carrier is herein derived.

The CPM controller of Fig. 2.10 regulates $i_L(t) = i_C$, and the average value of the DC-DC buck converter output voltage is $d_1 V_g$. The power into the DC-AC boost switch network is then (2.7).

$$P = i_L(t) \cdot d_1 \cdot V_g = i_c \cdot d_1 \cdot V_g \tag{2.7}$$

The DC-AC boost with $d_2$=0% achieves inversion without changing the magnitude of the DC-DC buck stage output. Thus, $\left| i_{pri}(t) \right| = i_L(t) = i_C$. Output current must change with changing load impedance to maintain constant output power, so both inductor current and the value of the control current limit must also change. However, for fixed $P$ and $V_g$, (2.7) contains two time-varying parameters ($i_C$ and $d_1$). Equation (2.7) can be simplified by substituting the definition of duty cycle, (2.8), where $0 \le t \le T_S$.

$$d_1 = \frac{t}{T_s} \tag{2.8}$$

Equation (2.8) is substituted into (2.7), and the value of $i_C(t)$ is solved for. The result is given in (2.9).

$$i_C(t) = \frac{P}{V_g} \cdot \frac{T_s}{t} \tag{2.9}$$

Equation (2.9) thus describes the average value of inductor current necessary to achieve constant power output for a given duty cycle. Use of $i_C(t)$ as the control current limit in a peak CPM

controller results in constant output power from a buck converter. Figure 2.11 illustrates the shape of the control current limit, showing that this is a nonlinear carrier, and demonstrates how use in a peak CPM controller establishes duty cycle. Note that while the value of the nonlinear carrier approaches infinity at $t$=0, Fig. 2.11 limits it to an arbitrary maximum value.

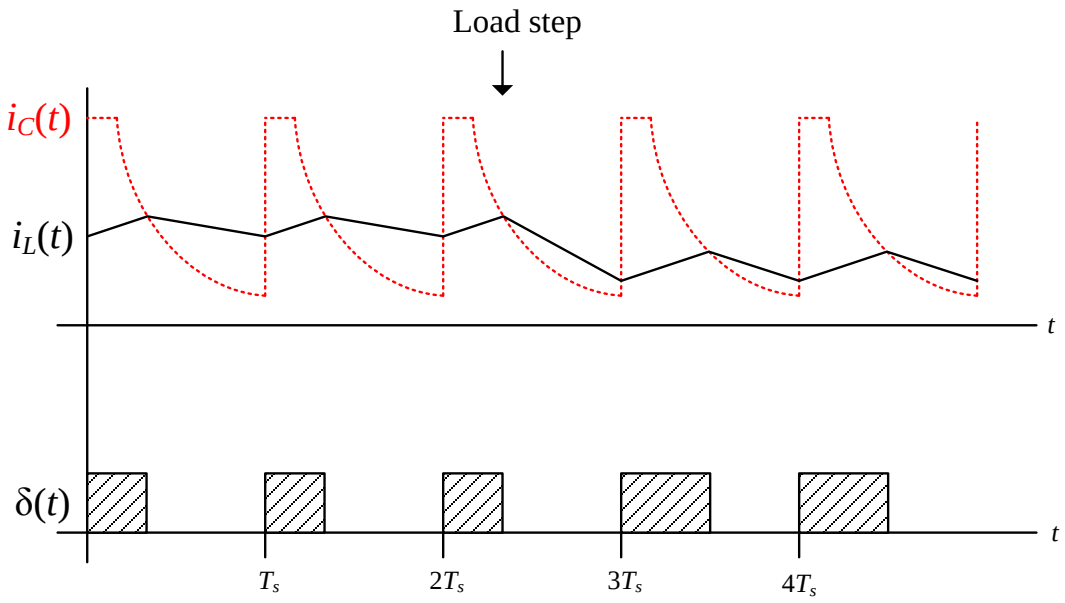


Fig. 2.11 – Use of nonlinear carrier control current limit

The use of nonlinear carrier control ("NLC") has seen previous use in power factor correction circuits to emulate a power sink [17, 18]. This work is the first known use of NLC to produce a power source.

### 2.3.1 – Combined Wide-Range Constant Power Source

Combination of the CPM boost stage with a NLC buck stage produces a wide-range constant power source without relying on high peak boost ratios (and the associated undesirable peak voltages). Figure 2.12 illustrates how these two stages might be series connected to span the full range of desired load impedances. A switch directs the output of the CPM controller to either the NLC buck ("$P_1$") or CPM boost ("$P_2$") stage, and a second switch selects the correct control current limit within the CPM controller.

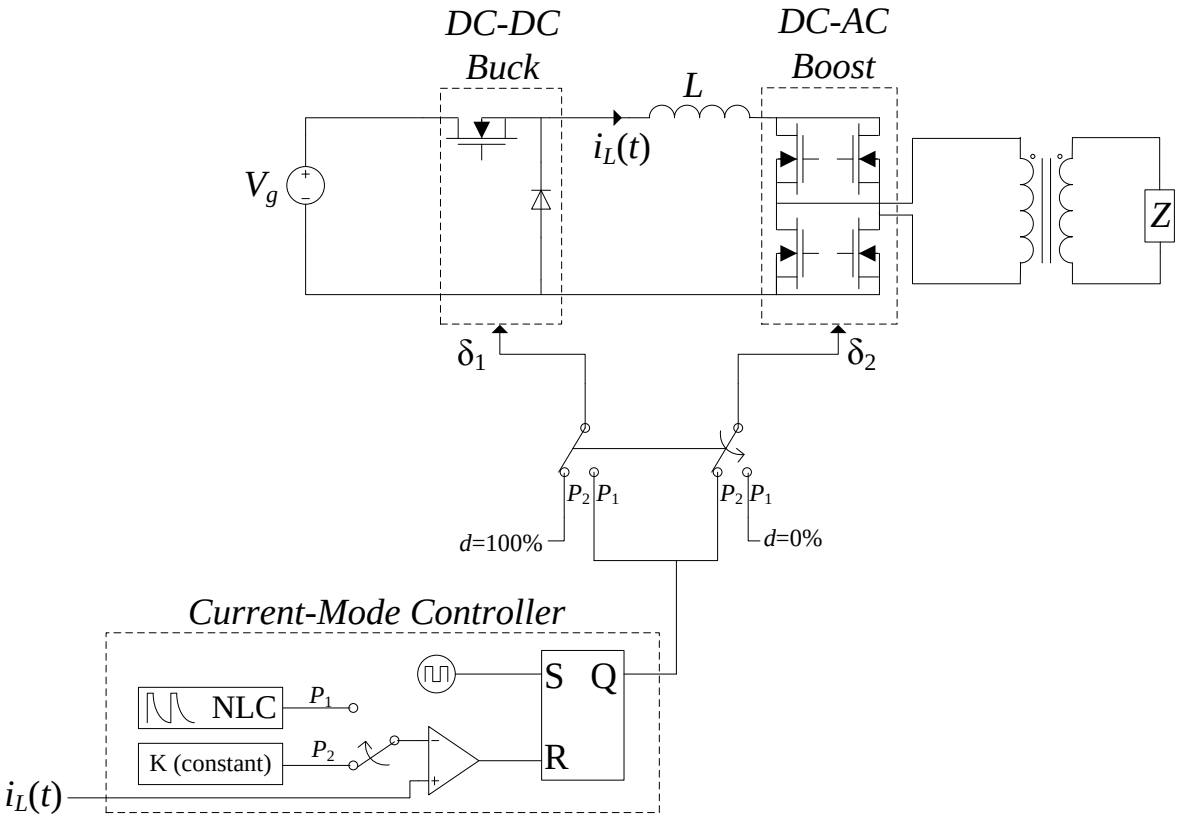


Fig. 2.12 – Series connection of NLC buck and CPM boost constant power stages

Using the typical specifications for monopolar ESGs given in Fig. 2.8, Fig. 2.13 illustrates how the series combination achieves the desired output without high peak voltages and duty cycle.

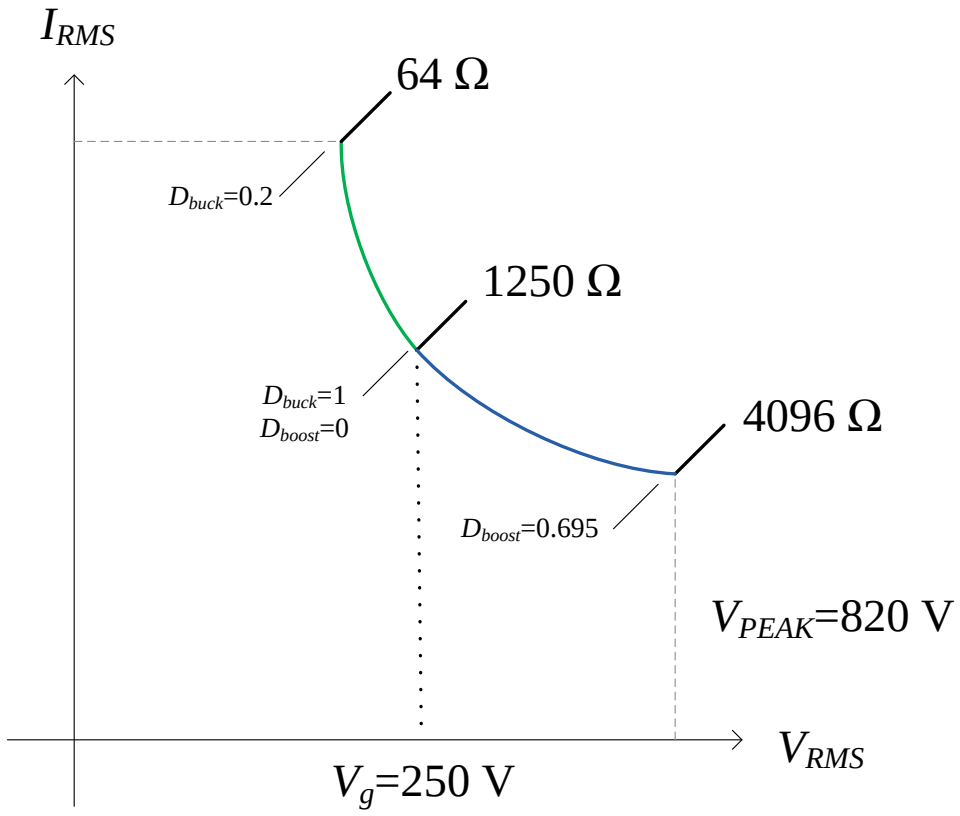


Fig. 2.13 – Output of series connected NLC buck (green) and CPM boost (blue)

Table 2.1 summarizes the difference between utilizing a single constant power stage versus two series-connected constant power stages when using the typical ESG specifications of Fig. 2.8.

Table 2.1 – Comparison between single- or dual-stage constant power source

| | CPM Boost alone | NLC Buck + CPM Boost |
|---|---|---|
| $V_{RMS\_MAX}$ | 453 V | 453 V |
| $d_{BOOST\_MAX}$ | 98% | 69.5% |
| $V_{PEAK}$ | 2,850 V | 820 V |

An additional benefit of series connecting the two constant power stages is the ability to adjust the value of $V_{PEAK}$ without adjusting the value of $V_{RMS\_MAX}$. This is accomplished by simultaneously changing the input voltage, $V_g$, and the maximum boost duty cycle, $d_{BOOST\_MAX}$, with the resulting output voltages given by (1.2) and (1.3). The ratio of $V_{PEAK}$ to $V_{RMS\_MAX}$ is defined as the *crest factor*, and the ability to adjust the crest factor at the maximum load impedance is clinically useful, as crest factor is often used as a proxy to describe the ability to achieve certain clinical effects (such as amount of carbonization and depth of cut).

## 2.4 – Constant Voltage Output

Finally, it is necessary to produce a constant voltage source to generate the maximum voltage limit. This voltage limit is frequently invoked during arc cutting, so an efficient source with fast transient response is required. This section presents two methods of generating the constant voltage AC source: use of voltage-mode control, and duty cycle limiting a CPM controller.

## 2.4.1 – Constant Voltage via PWM

One method of realizing a constant voltage output is to pulse-width-modulate a DC-AC boost inverter, using a standard voltage-mode control loop, as illustrated in Fig. 2.14.

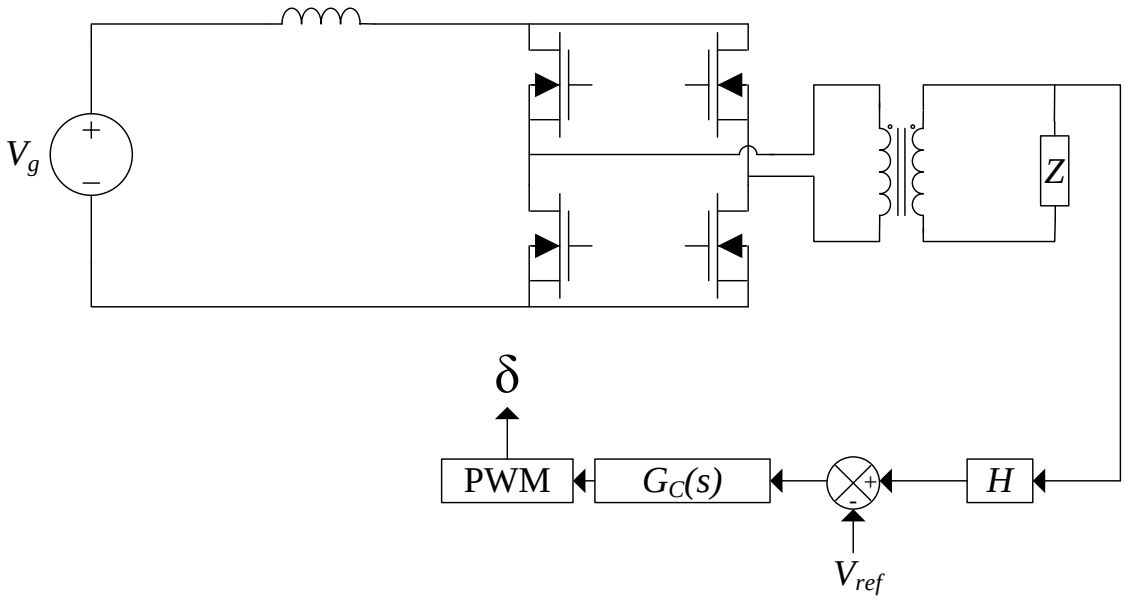


Fig. 2.14 – Maximum voltage limit using voltage-mode control

The sensor block, *H*, takes a measurement of the magnitude of the AC output voltage before feeding it to a voltage-mode controlled feedback loop. While this voltage-mode control loop can provide excellent steady-state regulation, high-speed arc processes may cause the apparent load impedance to change much more quickly than the control loop can respond. Transients may thus cause the peak voltage to exceed the maximum desired value. Also, use of this voltage-mode controlled solution requires a sensor to measure output voltage, which is otherwise unnecessary.

Thus, while use of voltage-mode control is intuitive when a constant voltage source is desired, the voltage-mode controlled solution suffers several limitations that result in less-than-ideal performance in this particular application.

## 2.4.2 – Constant Voltage via CPM Duty Cycle Limit

Given that a CPM controlled DC-AC boost inverter is already required for one-half of the constant power output mode, another option for realizing a constant voltage output is to duty cycle limit the existing CPM controller, as illustrated in Fig. 2.15.

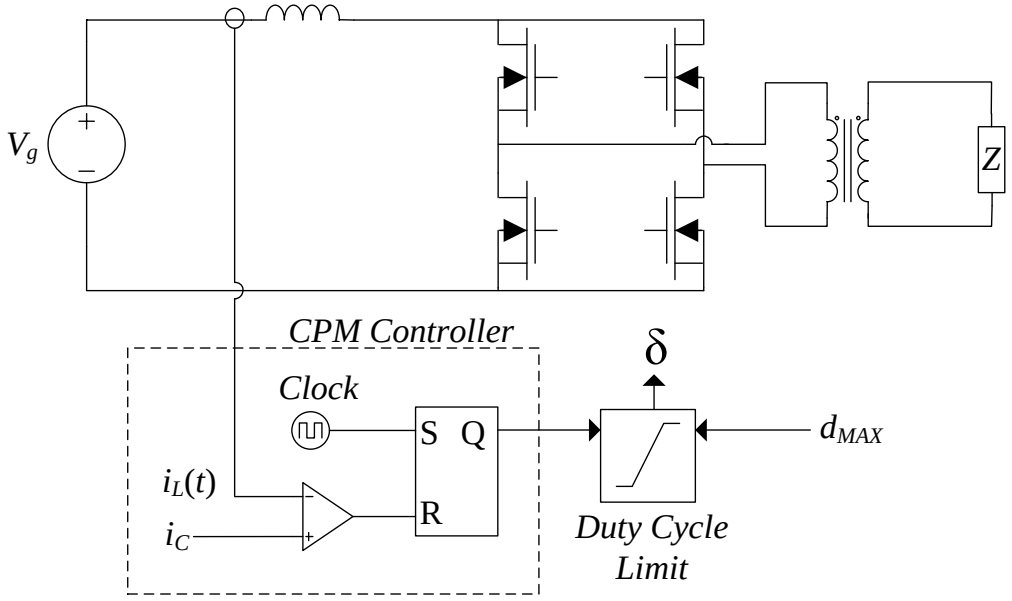


Fig. 2.15 – Maximum voltage limit using duty cycle limiting of CPM controller

Employing a duty cycle limit on the CPM controller amounts to running the DC-AC boost inverter open-loop. This results in poorer steady-state output voltage regulation, but provides the significant advantage of limiting the peak output voltage on a per-cycle basis, with no risk of transient overshoot. For this electrosurgical application, the steady-state value of the maximum output voltage is not especially important, as it would be unusual to operate in this output mode

for any length of time. Per-cycle transient voltage limiting, however, is highly useful as a means to limit potential undesirable arcing. Additionally, the maximum duty cycle is easily varied without the need to linearize an output voltage measurement or tune a compensator, and no sensor is required on the output.

## 2.5 – Mode Transitions

Methods are presented to realize individual portions of the desired ESG output characteristic. In a complete system, a mechanism must exist to allow the converter to choose which of the converters and control systems ought to be employed such that the ESG is operating in the correct output mode for any given load impedance. Two mechanisms for transitioning between operating modes are presented in this section: a method which determines the correct mode based on a direct measurement of output quantities, and a method which determines the correct mode based on duty cycle. The duty cycle method is shown to offer superior transient performance, and reduces additional hardware requirements.

### 2.5.1 – Mode Transitions via Direct Measurement

One method of determining the appropriate output mode for a given load impedance is to directly observe the average output voltage and current. Figure 2.16 shows how these measurements specify mode transitions for a converter that utilizes a buck converter to realize a maximum current limit ("$I_{max}$") and a constant power source ("$P_1$") and a boost inverter to realize a constant power source ("$P_2$") and a maximum voltage limit ("$V_{max}$").

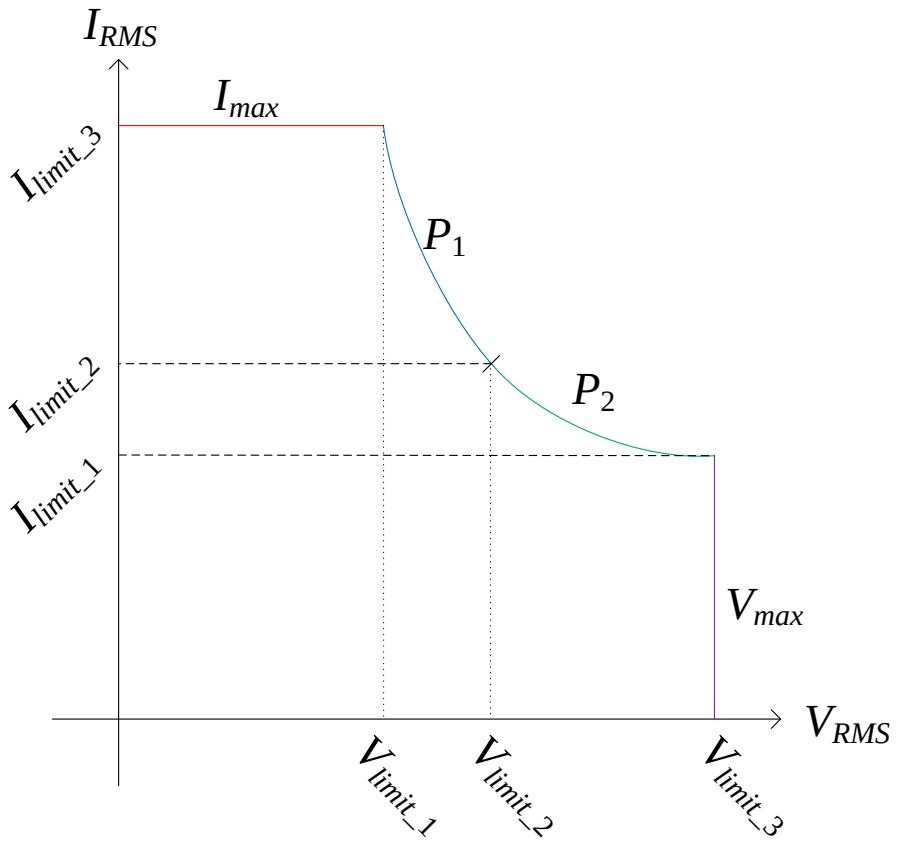


Fig. 2.16 – Specifying mode transitions by direct output voltage and current measurement

Since the output voltage is AC, with varying duty cycle, the magnitudes of the output voltage and current over a full cycle needs to be computed. Computing a true RMS value is time- and processor-intensive, and unnecessarily accurate for this application; any crude average which increases as the true RMS increases is sufficient.

Alternately, inductor current measurement (already required by the CPM controller) can be substituted for the output current measurement, as the average inductor current decreases as output voltage increases. Making this substitution eliminates the need for an output current sensor, but still requires the computation of a per-cycle average value of inductor current.

Figure 2.17 illustrates how a series of comparators can determine the operating mode.

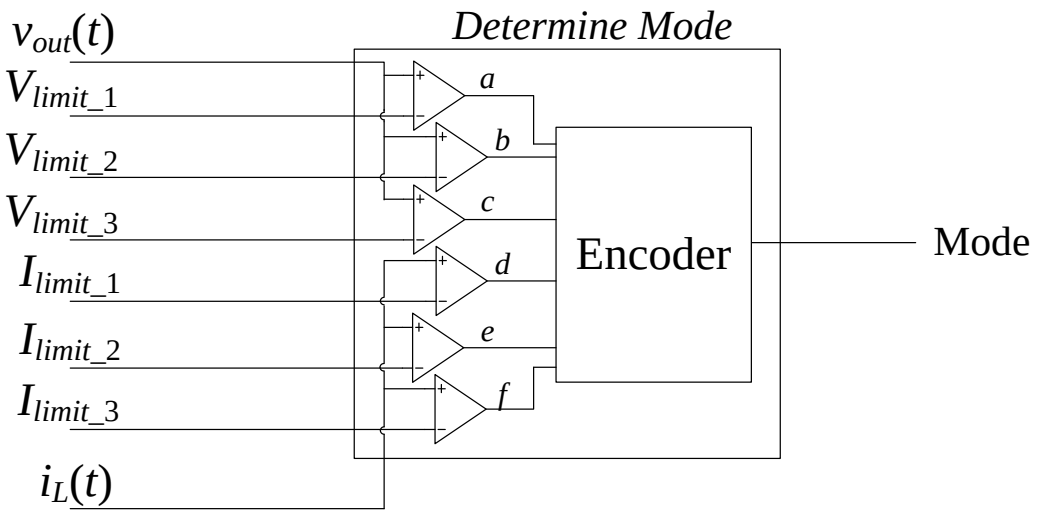


Fig. 2.17 – Logic to determine operating mode by direct measurement

The "Encoder" block of Fig. 2.17 performs the function specified in Table 2.2.

Table 2.2 – Function of "Encoder" block of Fig. 2.15

| ***a*** | ***b*** | ***c*** | ***d*** | ***e*** | ***f*** | **Mode** |
|---|---|---|---|---|---|---|
| 1 | 1 | 1 | 0 | 0 | 0 | $\boldsymbol{I_{max}}$ |
| 1 | 1 | 0 | 1 | 0 | 0 | $\boldsymbol{P_1}$ |
| 1 | 0 | 0 | 1 | 1 | 0 | $\boldsymbol{P_2}$ |
| 0 | 0 | 0 | 1 | 1 | 1 | $\boldsymbol{V_{max}}$ |

Increasing output voltage triggers mode transitions in the $I_{max} \rightarrow P_1 \rightarrow P_2 \rightarrow V_{max}$ direction, and increasing output current (or average inductor current) triggers mode transitions in the opposite direction.

Triggering mode transitions by direct measurement of voltage and current is an intuitive method of setting the correct operating mode. The transient response, however, suffers from at least one cycle of errant output per transition – for instance, the output voltage must exceed $V_{max}$ to set comparator output *c* high which triggers the transition to voltage limited mode. Such errors occur for at least one cycle and cause excessive power delivery, and occur for all six possible mode transitions.

### 2.5.2 – Mode Transitions via Duty Cycle

An alternative method of determining the appropriate output mode for a given load impedance is to observe the duty cycle generated by the CPM controller. This duty cycle command, combined with knowledge of the present operating mode, completely specifies the correct operating mode. Thus, it is possible to use a state machine to determine the correct operating mode, without any need to directly make any voltage or current measurements. For instance, when the $I_{\max}$ and $P_1$ regions are both realized using a buck converter, the intersection between these regions occurs at some fixed duty cycle. Figure 2.18 illustrates how knowledge of present operating mode and duty cycle can provide all necessary information to trigger mode transitions.

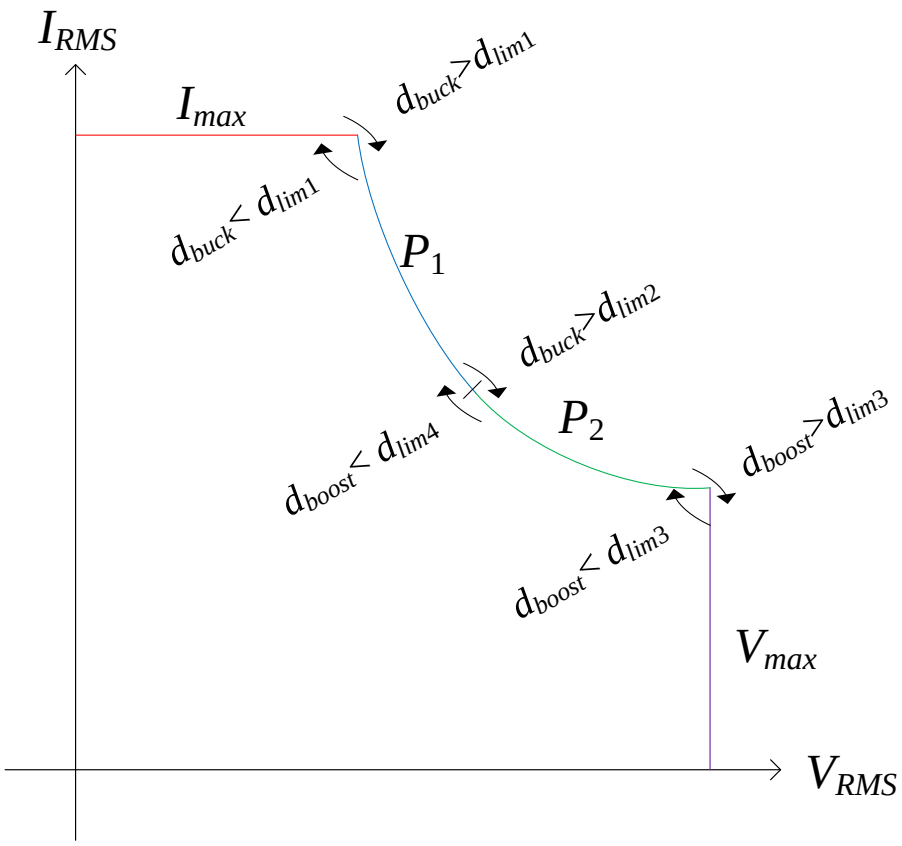


Fig. 2.18 – Mode transitions by knowledge of operating mode and duty cycle

Figure 2.19 Shows how a simple finite state machine and timer added to the CPM controller accomplishes the mode transitions illustrated in Fig. 2.18.

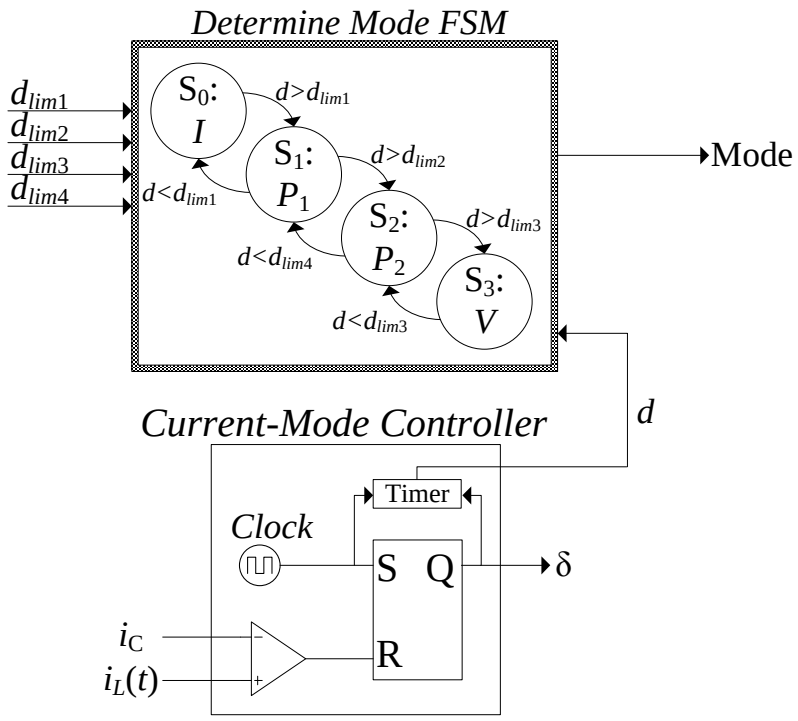


Fig. 2.19 – Finite state machine and timer to determine output mode by duty cycle

Using a state machine and duty cycle measurement to determine operating mode has several advantages over determining operating mode by direct measurement of voltage and current. First, no additional sensing of output voltage or current is necessary. Second, no need exists for computing an average of any voltages or currents. The transient performance of the state machine-based mode transitions is superior, as well. For instance, if the maximum voltage limit is established using a duty cycle limit on the CPM controlled boost inverter, the transition from constant power region $P_2$ to maximum voltage limit region $V_{max}$ occurs at the instant the duty cycle reaches the duty cycle limit, resulting in not even a single cycle of error. Likewise, transitions to and from the constant current limit occur without any error, as they occur at the instant the duty cycle reaches $d_{lim1}$. Transitions between constant power regions $P_1$ and $P_2$ exhibit

the potential for one cycle of error, as a transition from $P_1$ to $P_2$ will cause one cycle of deficient power delivery, and transition from $P_2$ and $P_1$ will cause one cycle of excessive power delivery. Overall, the transient response is superior, and especially notable is errorless transition to the maximum voltage limit, which is important to minimize arcing.

## 2.6 – Conclusions

To realize the ideal ESG output characteristic with near-deadbeat response, various implementations of CPM control are presented. A constant current AC output is realized using a CPM controlled DC-DC buck converter series connected to a DC-AC inverter. A constant power AC source is realized using two series-connected stages: a CPM controlled DC-AC boost inverter, and a NLC controlled DC-DC buck converter. Finally, a constant voltage output is realized using either a voltage-mode controlled DC-AC boost inverter, or by using a maximum open-loop duty cycle on a DC-AC boost inverter. Combination of these stages allows production of the ideal ESG output characteristic with high-speed control and output power regulation.

Transitions between operating modes are accomplished by either direct measurement of output voltage and current, or with a finite state machine and measurement of duty cycle. While direct measurement of output voltage and current is a logical, intuitive implementation, the state machine approach provides superior transient response. Notably, it is possible to invoke the maximum voltage limit with deadbeat response, resulting in perfect voltage limiting, which provides the important clinical benefit of regulating the length of arcs produced.

# CHAPTER 3

# MODELING AND ANALYSIS OF THE POWER SOURCE OUTPUT CHARACTERISTICS

The previous chapter provides a brief analysis of methods of producing constant power AC sources and claims that these methods achieve near-deadbeat output power regulation. This chapter expands on the analysis of the two previously-presented constant power AC sources, deriving analytical expressions and models useful for designing and optimizing the performance of these stages, and further justifying the claim that near-deadbeat output power regulation is realized.

Practical power sources deviate from ideality in several ways, with error in both transient and steady-state power delivery. This chapter describes three mechanisms by which the CPM boost and NLC buck constant power sources deviate from ideal power sources: peak-to-average error, artificial ramp-induced error, and transient error.

## 3.1 – Peak-to-Average Error

The proposed constant power source control schemes employ peak current-programmed mode control, which effectively regulates the maximum value of inductor current on a per-cycle basis. For low inductor current ripple, the maximum value of inductor current is approximately equal to the average value of inductor current. However, with large inductor current ripple, appreciable error can exist between the maximum and average value of inductor current, and this error is termed “peak-to-average error” [19].

In some applications of CPM control, peak-to-average error can be minimized or eliminated through a variety of compensation schemes [20, 21]. In applications where the converter operating point varies considerably, these schemes are generally not applicable.

### 3.1.1 – Peak-to-Average Error in the CPM Boost Stage

The boost inverter steady-state inductor current waveform is shown in Fig. 3.1. By integrating the waveform and dividing by the length of the switching period, the average value of the inductor current is found to be (3.1).

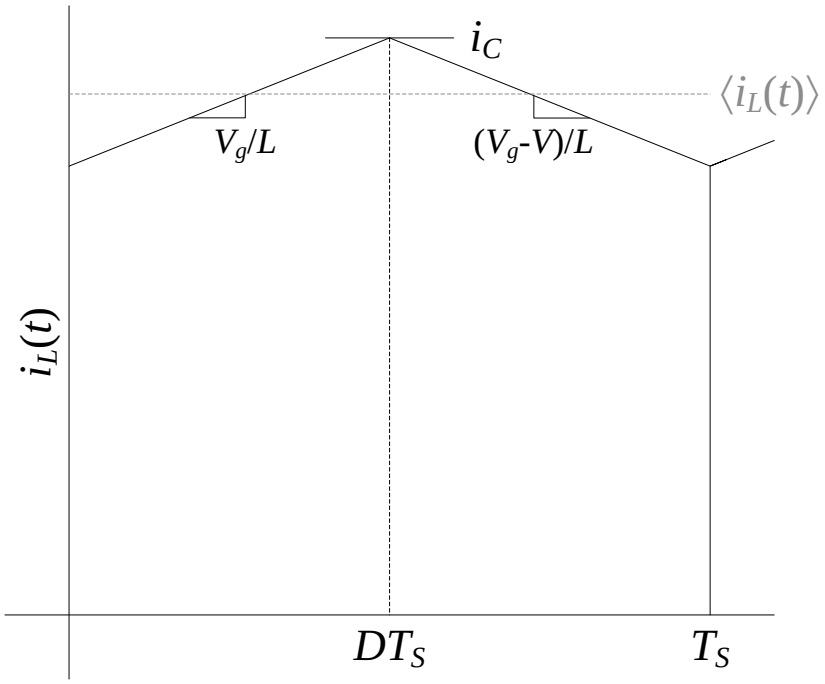


Fig. 3.1 – Boost inductor current in steady-state

$$\left\langle i_L(t) \right\rangle_{Ts} = i_c - \frac{V_g T_S}{2L} D \tag{3.1}$$

In peak CPM control, ripple in the inductor current causes an operating point-dependent error to exist between the peak and average inductor current. This peak-to-average error thus causes output power to vary with operating point, which is undesirable and should be minimized by minimizing the magnitude of the inductor current ripple. Given that the output power from the ideal boost inverter is $V_g \cdot \left\langle i_L(t) \right\rangle_{Ts}$, algebraic manipulation shows that the maximum peak-to-average error in steady-state output power delivery is (3.2).

$$\Delta P_{out} = \frac{V_g{}^2 D T_s}{2L} \tag{3.2}$$

As expected (and shown by (3.2)), increasing the size of the boost inductor minimizes peak-to-average error. Figure 3.2 illustrates the effect peak-to-average error in the CPM boost inverter has on the steady-state output characteristic of the series NLC buck – CPM boost wide-range constant power source.

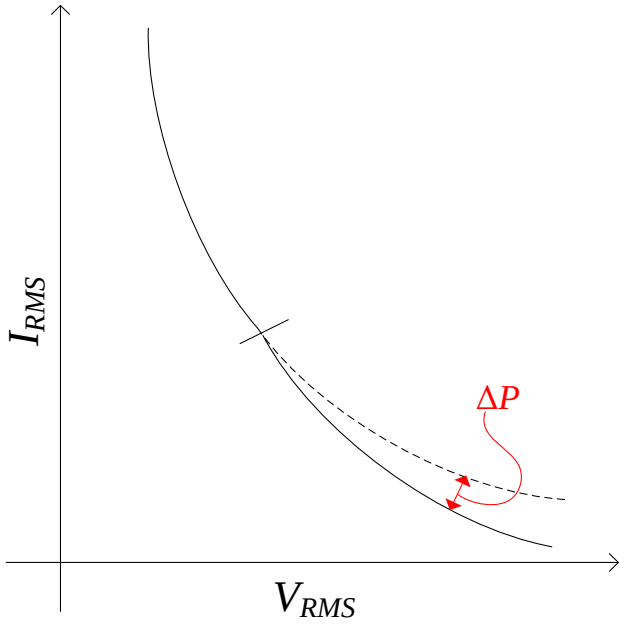


Fig. 3.2 – Peak-to-average error from CPM boost

## 3.1.2 – Peak-to-Average Error in the NLC Buck Stage

Section 2.3 derives an equation for a nonlinear carrier for use with a CPM buck converter, repeated here as (3.3).

$$i_C(t) = \frac{P \cdot T_s}{V_g \cdot t} \tag{3.3}$$

When used as the control current limit in a peak CPM controller with low inductor current ripple, the value of $i_C(t)$ given in (3.3) establishes the correct duty cycle to set the steady-state inductor current equal to the value needed to obtain constant power output over varying load impedances. However, $i_L(t) \neq i_C(t)$, rather, in the steady-state, $\frac{t}{T_S} = D$, and $\langle i_L \rangle_{Ts} = i_C = \frac{P}{DV_g}$.

Large ripple in the inductor current invalidates $\langle i_L \rangle_{Ts} = i_C$, because while the peak inductor current may equal the duty-cycle-dependent control current limit, the peak inductor current does not equal the average inductor current, as shown in Fig. 3.3. It is desired to specify the maximum allowable steady-state error between the peak and average inductor current, and size the buck inductor to meet this requirement.

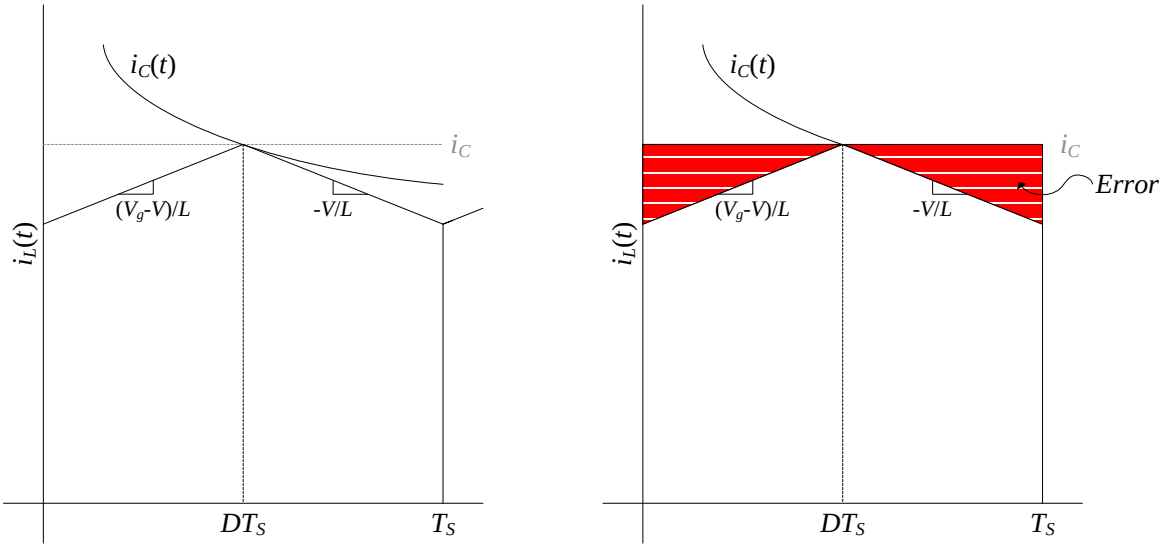


Fig. 3.3 – Steady-state buck inductor current waveform showing peak-to-average error

For the inductor current of Fig. 3.3, the error between the control current limit, $i_C$, and the average inductor current, $\langle i_L \rangle_{Ts}$, is given by (3.4).

$$\langle i_L(t) \rangle_{Ts} = i_c - \frac{V_g T_S}{2L} DD' \tag{3.4}$$

Since $\langle P_{OUT} \rangle_{Ts} = V \cdot \langle i_L \rangle_{Ts}$, the maximum steady-state output power error is (3.5).

$$\Delta P_{out} = \frac{V_g{}^2 D^2 D' T_s}{2L} \tag{3.5}$$

As expected (and predicted by (3.5)), larger values of $L$ decrease current ripple and reduce output power error in the steady-state. Figure 3.4 illustrates the effect peak-to-average error has on the steady-state output characteristic of the series NLC buck – CPM boost wide-range constant power source.

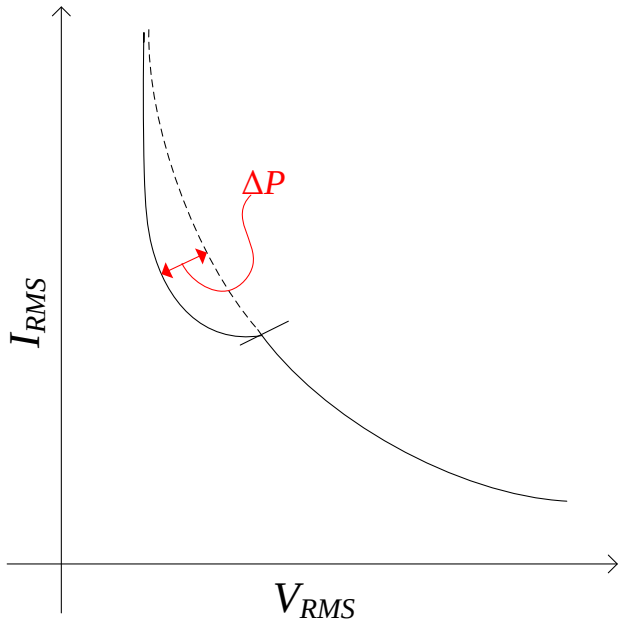


Fig. 3.4 – Peak-to-average error from NLC buck

## 3.2 – Artificial Ramp-Induced Error

A variation of peak-to-average error exists when an artificial compensating ramp is added to the CPM controller. Addition of an artificial ramp is known to be necessary for stability of CPM converters operating at $D$=50% or greater [22], and is also beneficial for improving noise immunity in the sensed inductor current signal. In this work, the CPM boost inverter employs a substantial artificial ramp for noise immunity, while the NLC buck does not require any artificial ramp, as the large magnitude of the nonlinear carrier satisfies both the stability and noise immunity functions.

Addition of an artificial ramp effectively introduces a duty cycle-dependent variation in the value of $i_C(t)$, as shown in Fig. 3.5.

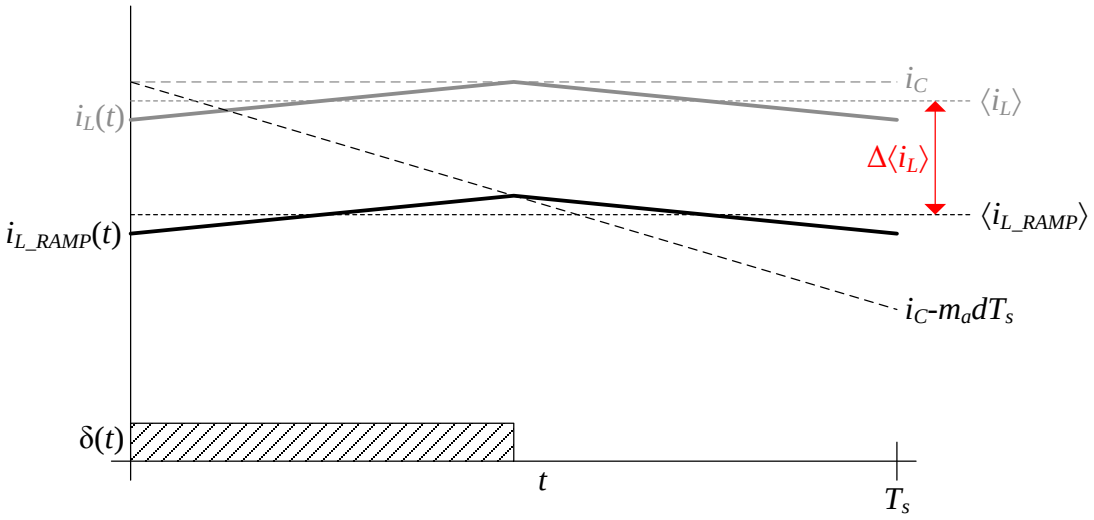


Fig. 3.5 – CPM control with and without artificial ramp

Note that a difference between the average values of $i_L(t)$ is present which depends on the magnitude of the artificial ramp. The artificial ramp-induced error in delivered output power for the CPM boost is given by (3.6).

$$\Delta P_{out} = V_g M_a D T_s \tag{3.6}$$

Thus, artificial ramp-induced error can be minimized in the CPM boost power source by minimizing the magnitude of artificial ramp employed.

Figure 3.7 shows the effect that this error has on the combined NLC buck – CPM boost wide-range constant power source. Note that no artificial ramp-induced error is present in the NLC buck portion of the constant power curve, but an error which increases with duty cycle is present in the CPM boost portion.

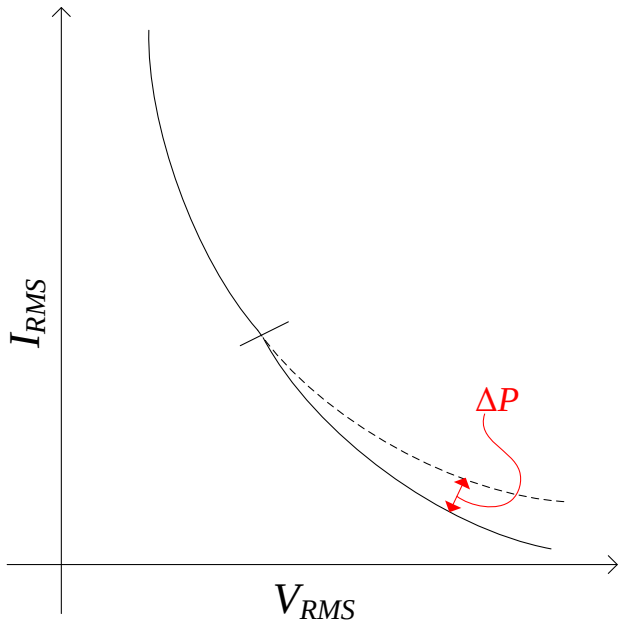


Fig. 3.6 – Artificial ramp-induced error

## 3.3 – Transient Error

In addition to steady-state errors, the constant power sources exhibit transient errors whenever the load impedance changes and the converters establish new steady-state operating points. To predict transient variations in output power, small signal modeling is employed. For a resistive load, variation in output voltage predicts variation in output power. By injecting a test current into the loaded converter output, a transfer function can be written between the output voltage and the injection source, which is, by definition, output impedance. Calculation of the converter closed-loop output impedance can thus predict the transient response of the constant power source characteristics.

An ideal constant power source has a hyperbolic output characteristic in the ($i$, $v$) plane. Figure 3.7 shows the definition of the small-signal terminal quantities of an ideal constant power source, and Fig. 3.8 shows the ideal output curve linearized about a steady-state operating point to ascertain the small-signal output impedance.

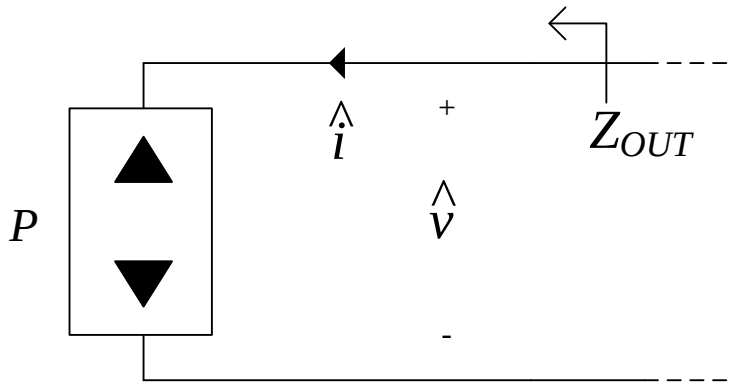


Fig. 3.7 – Definition of small-signal terminal quantities of constant power source

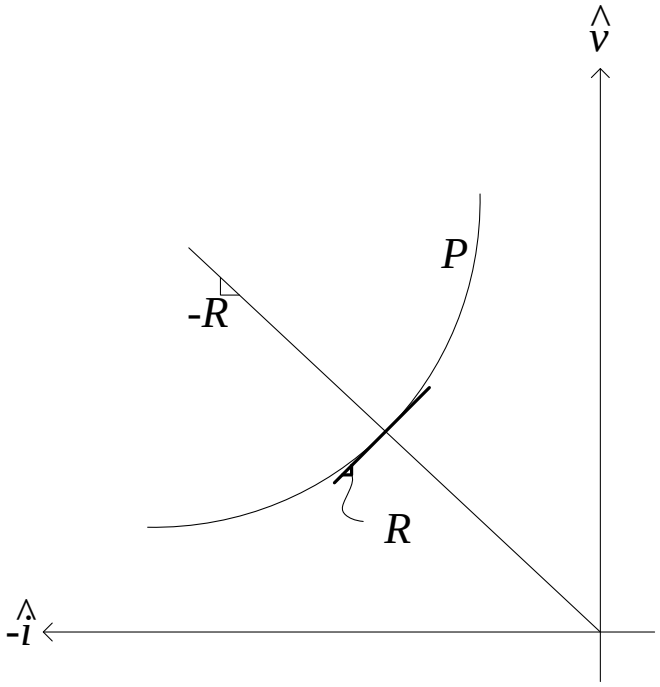


Fig. 3.8 – Linearized output characteristic of constant power source

In Fig. 3.8, constant output power is represented by a hyperbola in the (*i*,*v*) plane. The line with slope –*R* intersects the constant power hyperbola to set the steady-state operating point. A segment of the constant power hyperbola linearized about the steady-state operating point has slope *R*, showing that the small-signal output impedance of the ideal constant power source is *R*.

Output impedances are often defined as being *outside* output impedances if they are measured including the load which sets the steady-state operating point, or *inside* output impedances if they exclude the load. Since the incremental output resistance of an ideal constant power source is *R*, the ideal inside output impedance is *R*, and the ideal outside output impedance is *R*/2, as shown in Fig. 3.9.

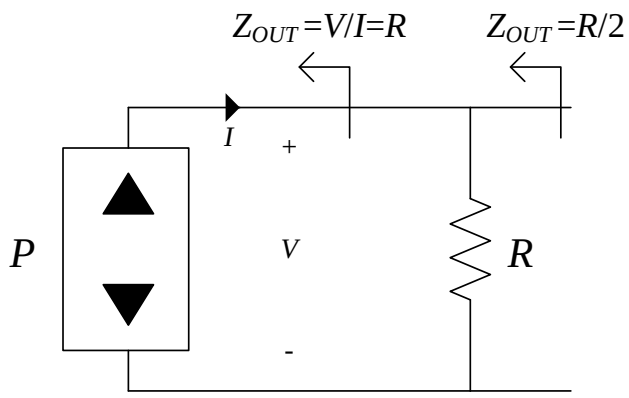


Fig. 3.9 – Inside and outside output impedances of constant power source

Thus, a circuit which behaves as an ideal constant power source should exhibit the output impedances shown in Fig. 3.9. Deviation from these ideal output impedances is evidence of the non-ideality of a practical constant power source.

### 3.3.1 – Output Impedance of CPM Boost

Figure 3.10 shows a simplified small-signal model of a boost converter with CPM control system, derived by perturbing and linearizing the expression for the averaged inductor current. Values of the modulator gain block ($F_m$) and output voltage feedback block ($F_v$) are calculated following the procedure of [25], and are given as (3.7) and (3.8), respectively.

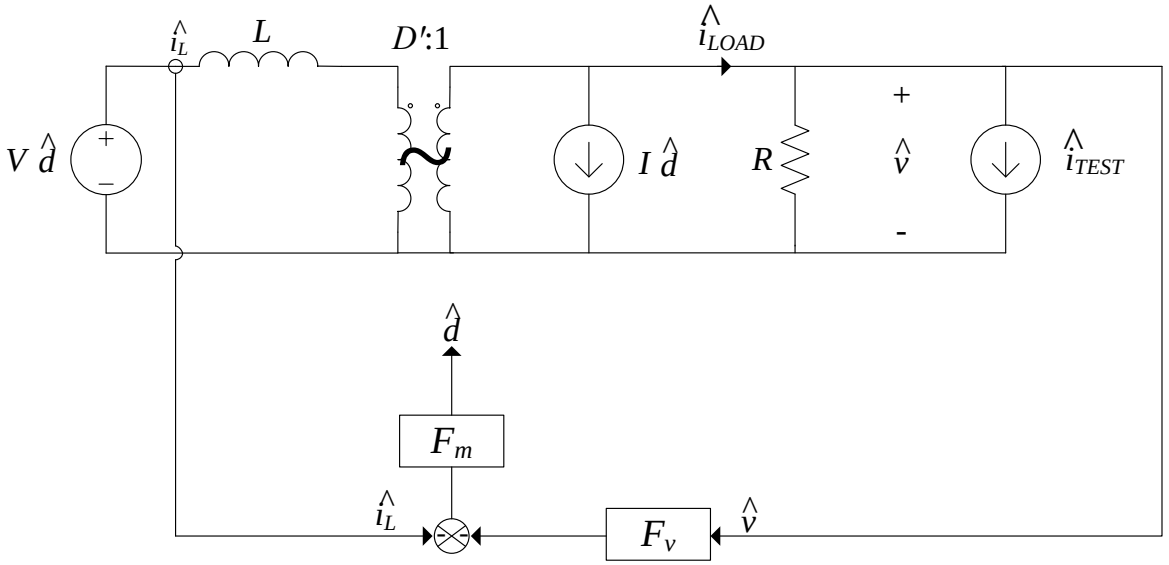


Fig. 3.10 – Simplified small-signal model of CPM boost converter

$$F_m = \frac{2L}{VT_s(D' - D)} \tag{3.7}$$

$$F_v = \frac{DD'T_s}{2L} \tag{3.8}$$

Note that in the actual CPM boost converter, no physical feedback from the output voltage exists. This feedback loop appears in the small-signal model because of the dependence of the inductor current slope on the output voltage.

In the model of Fig. 3.10, the outside output impedance is defined by (3.9), and the inside output impedance is defined by (3.10).

$$Z_{OUT\_OUTSIDE} = \frac{-\hat{v}}{\hat{i}_{TEST}} \tag{3.9}$$

$$Z_{OUT\_INSIDE} = \frac{-\hat{v}}{\hat{i}_{LOAD}} \tag{3.10}$$

The expression for the inside output impedance is calculated by evaluating (3.10). Three equations (3.11) are written by inspection of the circuit of Fig. 3.10.

$$\hat{d} = F_m(-\hat{i}_L - F_v\hat{v})$$

$$\hat{i}_L = \frac{I}{D'}\hat{d} + \frac{\hat{i}_{LOAD}}{D'} \tag{3.11}$$

$$\hat{v} = \left(\frac{R}{R + \frac{sL}{D'^2}}\right)\frac{V}{D'}\hat{d} - \left(\frac{R\frac{sL}{D'^2}}{R + \frac{sL}{D'^2}}\right)I\hat{d} - \left(\frac{R\frac{sL}{D'^2}}{R + \frac{sL}{D'^2}}\right)\cdot\left[\hat{i}_{LOAD} - \frac{\hat{v}}{R}\right]$$

Through algebraic manipulation of (3.11), the final result for the output impedance transfer function in standard pole-zero form is given by (3.12).

$$Z_{OUT}(s) = \frac{-\hat{v}}{\hat{i}_{LOAD}} = \left(\frac{1}{\frac{1}{R} + F_vD' + \frac{D'^2}{F_mV}}\right)\cdot\frac{1 + \frac{s}{\omega_z}}{1 + \frac{s}{\omega_p}} \tag{3.12}$$

$$\text{where } \omega_z = \frac{2}{T_s(D' - D)}$$

$$\text{and } \omega_p = \frac{RT_sD'^3 + 2L}{DLT_s}$$

The closed-loop inside output impedance of the CPM boost converter thus contains a single pole and a single zero. For large $L$, the modulator gain ($F_m$) becomes large and the output voltage feedback ($F_v$) becomes small, and the DC gain of (3.12) approaches $R$, as expected. For reasonable circuit parameter values, the frequency of the zero is much lower than the frequency of the pole; thus, the zero frequency defines the bandwidth of the constant power region, as it specifies where the inside output impedance stops being equal to $R$. Notably, the expression in (3.12) for the zero frequency is independent of the value of $L$ – the size of the inductor can be made arbitrarily large without affecting the transient response of the inverter. This is shown in Fig. 3.11, where the output impedance is plotted for two different values of $L$.

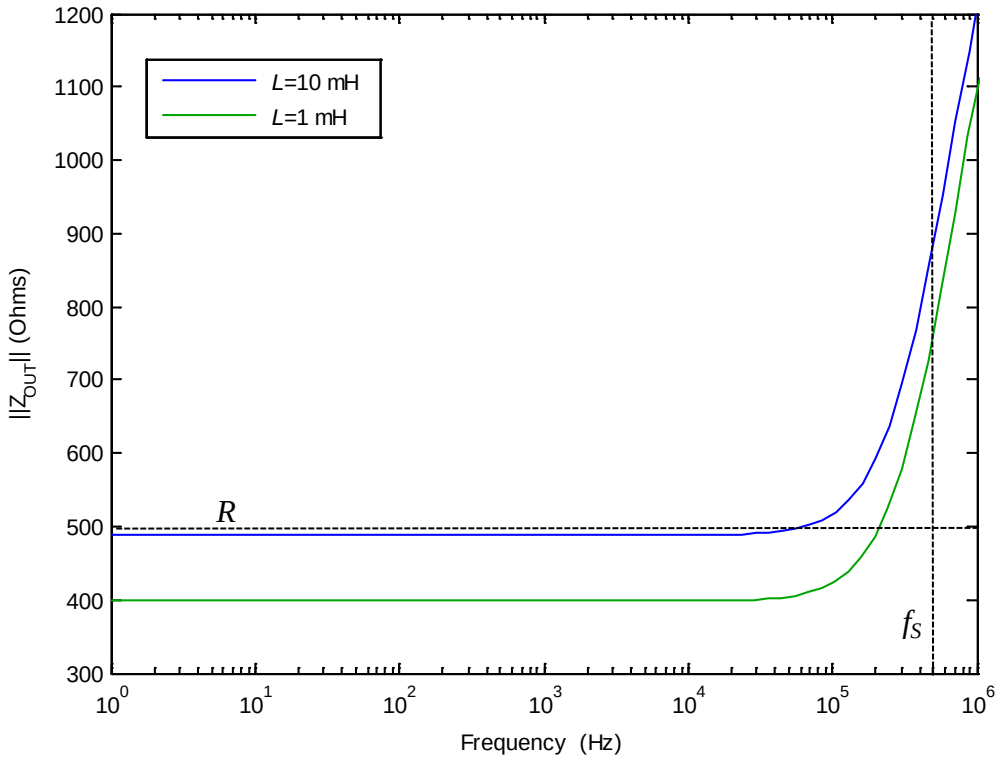


Fig. 3.11 – CPM boost output impedance for different values of $L$

Figure 3.12 shows the average output power from a prototype CPM boost inverter constructed with two different inductor values, where average output power is calculated as a moving average over one switching cycle (at 472 kHz).

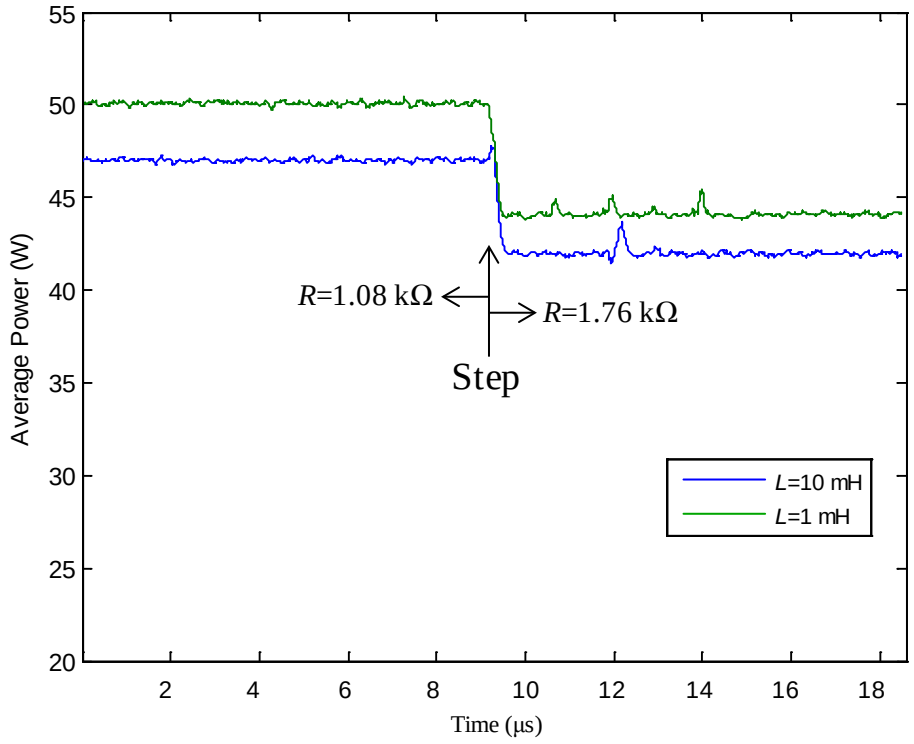


Fig. 3.12 – Load step in prototype CPM boost inverter showing transient responses

At the center of Fig. 3.12, a load step occurs from 1.08 kΩ to 1.76 kΩ, and the transient response of the converter is shown to be the same for both values of *L*. Thus, it is experimentally confirmed that the transient response of the CPM boost inverter is not affected by the size of the inductor. However, (3.12) does indicate that the transient response is dependent on duty cycle. This is experimentally demonstrated in Fig. 3.13, where a prototype CPM boost inverter is shown to exhibit an output power overshoot and longer settling time when operated at lower duty cycles.

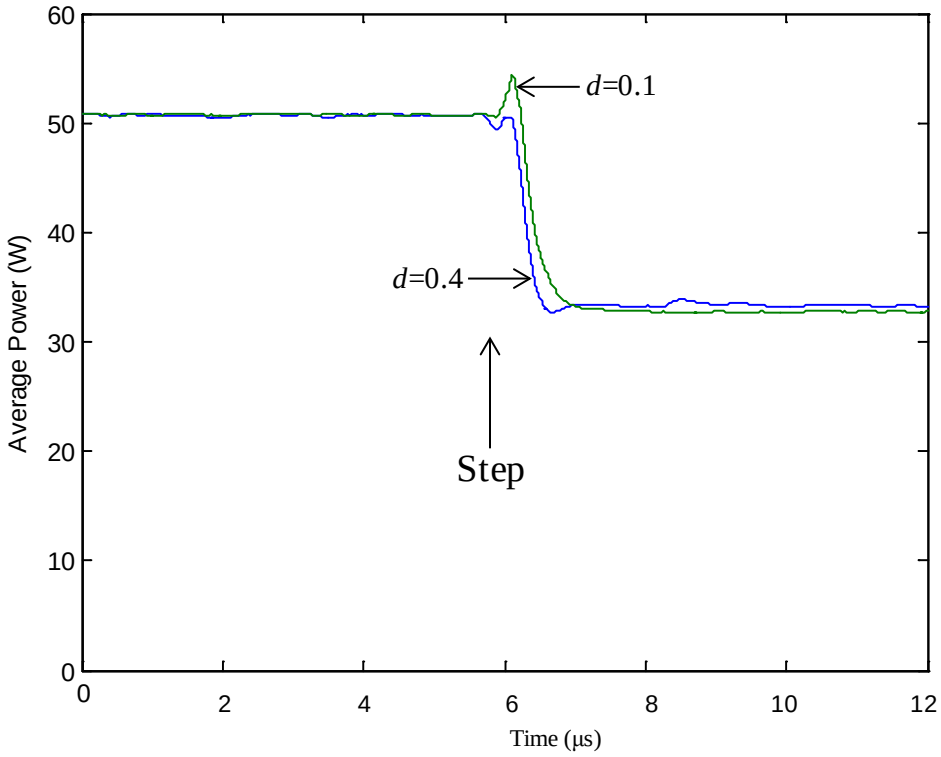


Fig. 3.13 – Load steps in CPM boost for different duty cycles

## 3.3.2 – Output Impedance of NLC Buck

The derivation of the closed-loop inside output impedance of the NLC buck proceeds in the same manner as the CPM boost, except that the model does not include effective feedback of the output voltage, but does include a minor feedback loop (with gain $F_c$) accounting for the duty cycle variation excited by the nonlinear carrier, which is herein derived. The expression for the nonlinear carrier, (3.3), can be written in terms of duty cycle as (3.13).

$$i_C = \frac{P}{DV_g} \tag{3.13}$$

The value of the nonlinear carrier, linearized about a small-signal operating point, is found by taking the derivative of (3.13) with respect to duty cycle, as shown in (3.14).

$$\frac{\hat{i}_C}{\hat{d}} = \frac{P}{V_g}\frac{d}{dD}\left(\frac{1}{D}\right) = \frac{P}{V_g}\left(\frac{-1}{D^2}\right) \tag{3.14}$$

Substituting the buck converter steady-state conversion ratio, $V=DV_g$, a simple expression for the value of the small-signal gain block $F_c$ is found as (3.15).

$$F_c = \frac{\hat{i}_C}{\hat{d}} = \frac{-P}{DV} \tag{3.15}$$

The simplified small-signal model of the NLC buck converter, derived by perturbing and linearizing the expression for the averaged inductor current, is shown in Fig. 3.14. The values for $F_m$ and $F_c$ are given by (3.13) and (3.14), respectively.

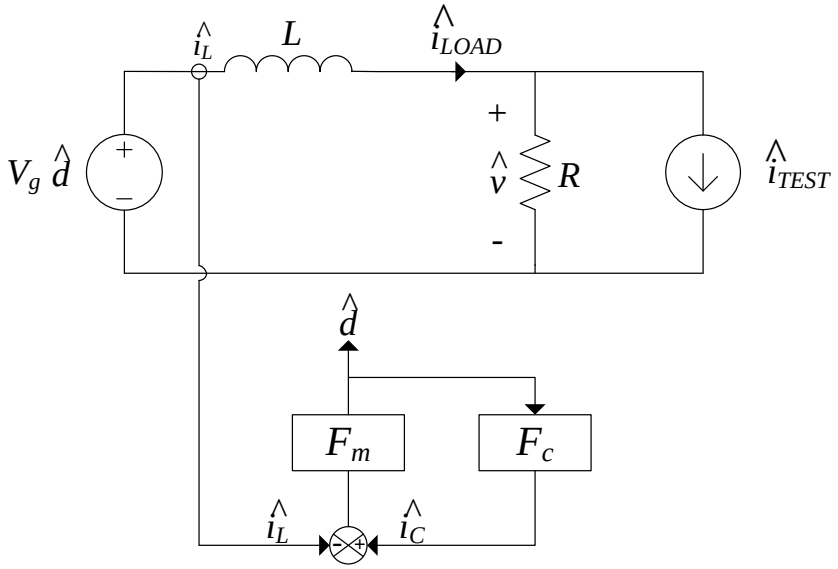


Fig. 3.14 – Small-signal model for calculating NLC buck output impedance

$$F_m = \frac{2L}{V_g T_s (D' - D)} \tag{3.13}$$

$$F_c = \frac{-P}{DV} \tag{3.14}$$

From the circuit of Fig. 3.13, Equations (3.15) are written.

$$\hat{d} = F_m(\hat{i}_C - \hat{i}_L)$$

$$\hat{i}_C = F_c \hat{d} \tag{3.15}$$

$$\hat{i}_{LOAD} = -\hat{i}_L + \frac{\hat{v}}{R}$$

$$\hat{v} = \left(\frac{R}{R+sL}\right) V_g \left(\frac{-F_m}{1 - F_m F_c}\right) \hat{i}_L + \left(\frac{sLR}{R+sL}\right) \frac{\hat{v}}{R} - \left(\frac{sLR}{R+sL}\right) \hat{i}_L$$

Equations (3.15) are algebraically manipulated to arrive at the expression for the inside output impedance of the NLC buck, (3.16).

$$Z_{OUT}(s) = \frac{R}{1 + \left(\frac{T_s(D' - D)}{2L}\right)} \cdot \left(1 + \frac{s}{\omega_z}\right) \tag{3.16}$$

$$\text{where } \omega_z = \frac{1}{\frac{T_s(D' - D)}{2} + \frac{L}{R}}$$

The closed-loop inside output impedance of the NLC buck thus contains a single zero. For large *L*, the denominator of the DC gain term goes to 1, causing the DC gain to approach *R* (as expected). The zero frequency defines the bandwidth of the constant power region. For large *L*, the zero frequency reduces to approximately *R*/*L*. Unlike in the CPM boost, all energy stored in the inductor must be discharged into load *R* (there is no alternative path), so under- and over-shoots in output power are expected (and predicted by (3.16)). Figure 3.15 shows the frequency response for different values of *L*.

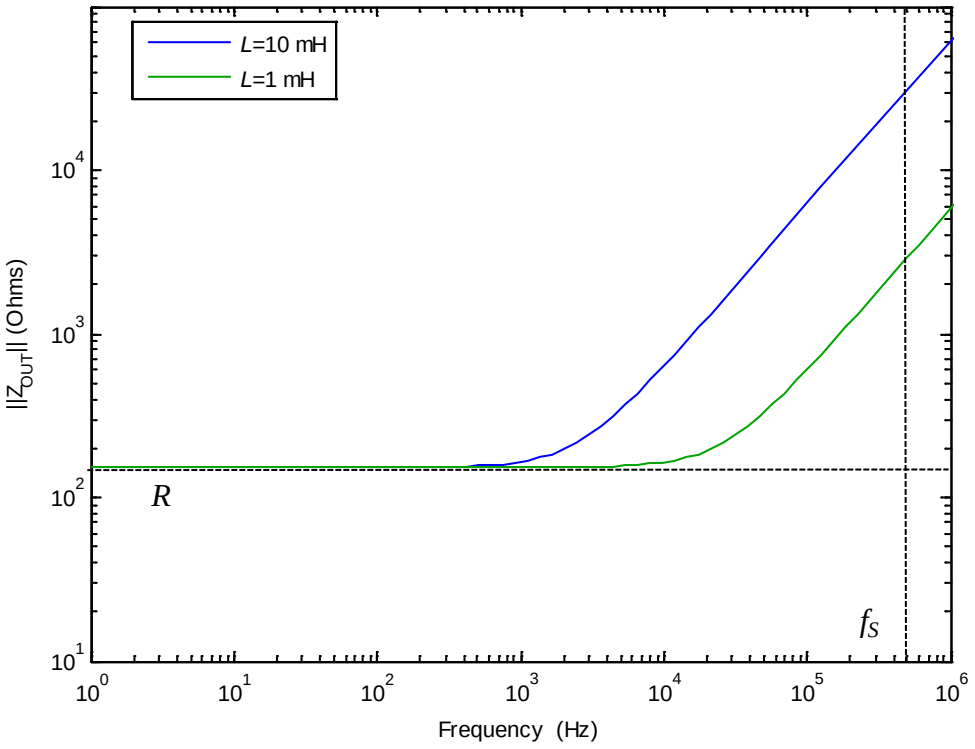


Fig. 3.15 – NLC buck output impedance for different values of *L*

Figure 3.15 shows how the size of the inductor specifies the corner frequency, and thus, larger *L* decreases the bandwidth of the NLC buck constant power source. Figure 3.16 shows the moving average of the output power from a prototype NLC buck converter constructed with two different

inductor values. At the center of the plot, a load step occurs, and a power overshoot occurs, which is larger for the larger value of *L*.

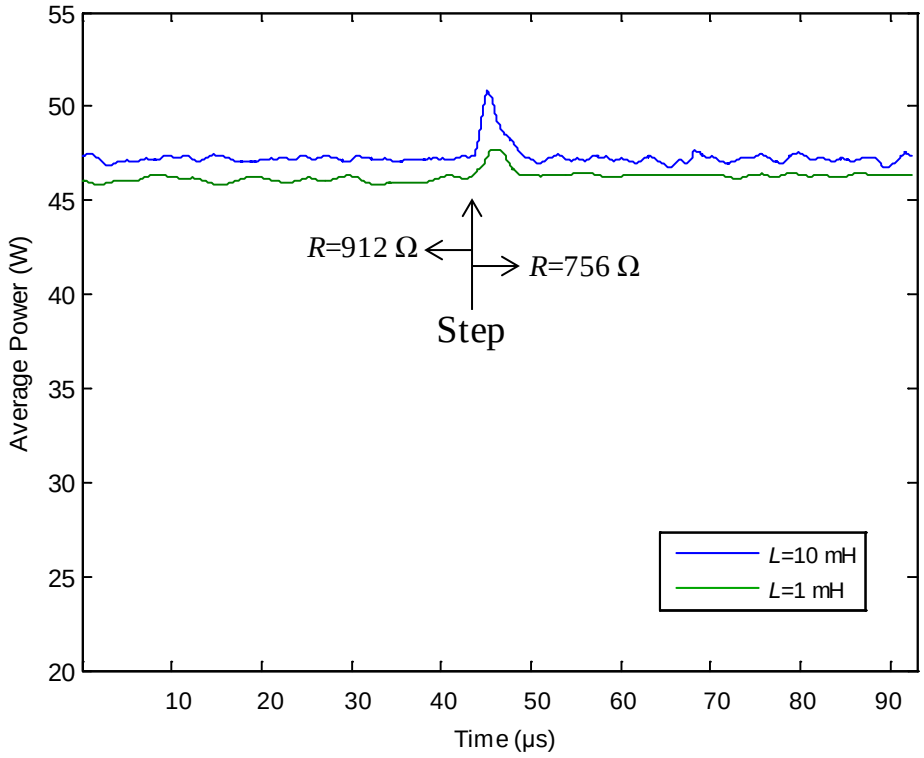


Fig. 3.16 – Load step in prototype NLC buck showing varying transient response

Thus, it is experimentally confirmed that the size of the inductor does affect the transient response of the NLC buck constant power source. As predicted by (3.16), the load resistance also affects the transient response. This is experimentally demonstrated in Fig. 3.17, where the load steps to 171% of the initial value for two different initial values: one relatively low and one relatively high. For the relatively low values, the transient response is significantly poorer.

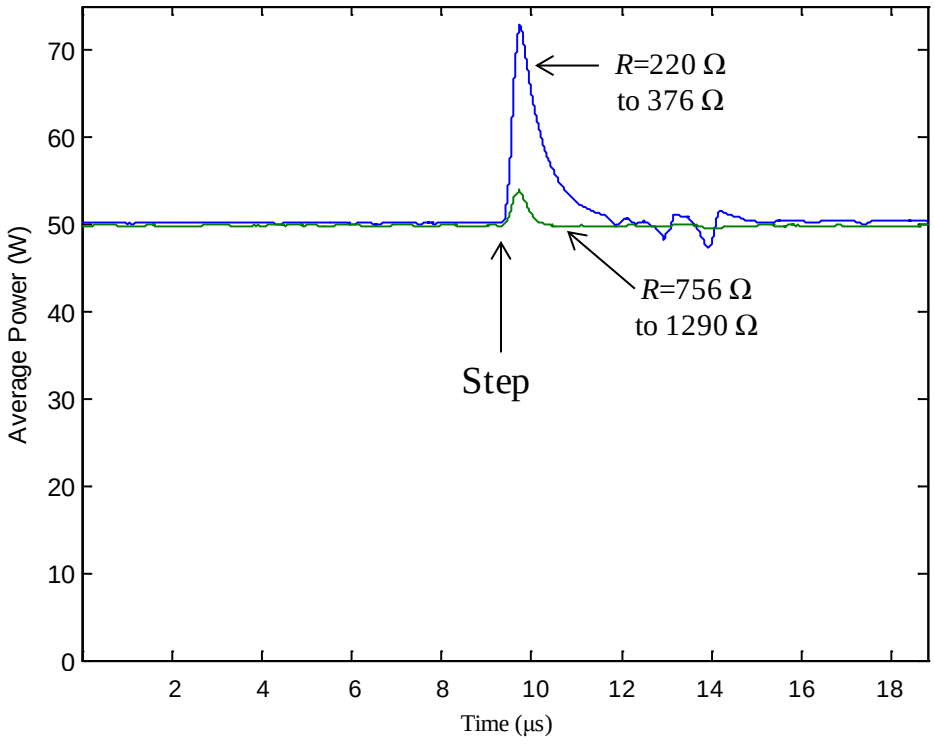


Fig. 3.17 – Load steps in NLC buck for different values of resistance

### 3.3.3 – Sampling Effects

Both constant power source stages establish their respective duty cycles only once per switching cycle. This introduces a discrete-time sampling effect into the system dynamics. Figure 3.18 illustrates addition of this sampling effect to the CPM boost small-signal model of Fig. 3.10, and Fig. 3.19 illustrates the effect in the NLC buck small-signal model of Fig. 3.14.

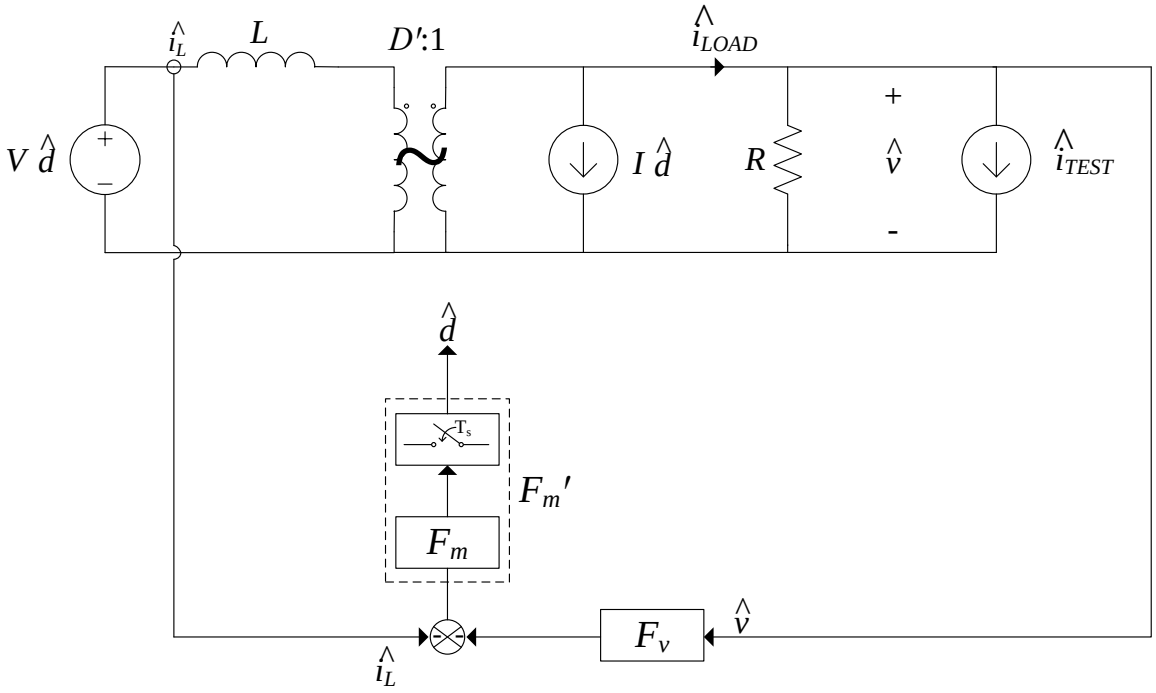


Fig. 3.18 – CPM boost small-signal model with sampling effect added

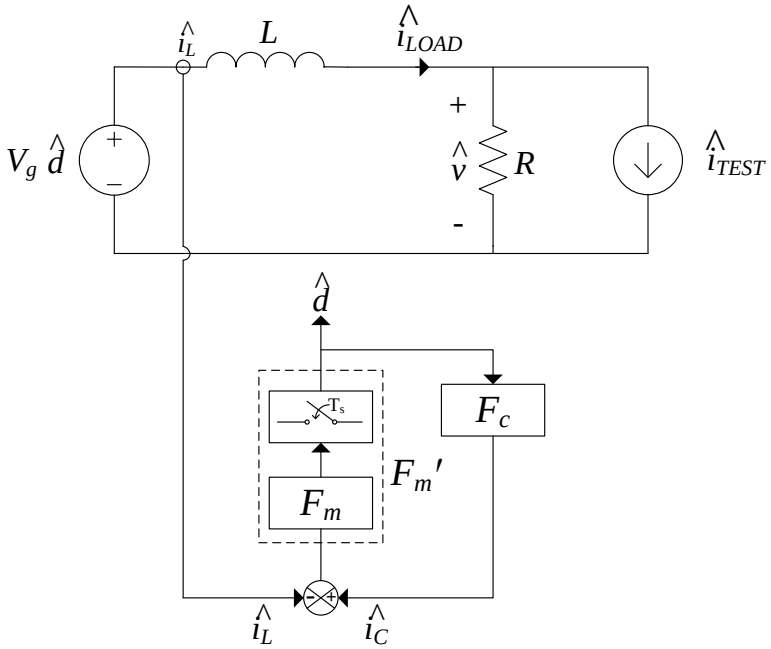


Fig. 3.19 – NLC buck small-signal model with sampling effect added

One of several methods [23, 24] of accounting for this behavior is to model the sampling effect as an added pole in the modulator gain block ($F_m$) [25]. The modified modulator gain is given as (3.17), where $V_{off}$ represents the maximum switch blocking voltage (equal to $V_g$ in the buck converter and $V$ in the boost converter) [26].

$$F_m{}' = \frac{2L}{V_{off} T_s (D' - D)\left(1 + \frac{s}{\omega_{ps}}\right)} \tag{3.17}$$

The pole frequency is (3.18), in which $D'_{\min}$ is the smallest value of $D'$ for which the converter will maintain stability for a given magnitude of artificial ramp.

$$\omega_{ps} = \frac{\pi \omega_s (D'_{\min} / D - 1)}{4} \tag{3.18}$$

Figure 3.20 shows the output impedance of the NLC buck with and without the sampling effect included, and Fig. 3.21 does the same for the CPM boost. Both cases are shown for a nominal inductor value of 1 mH.

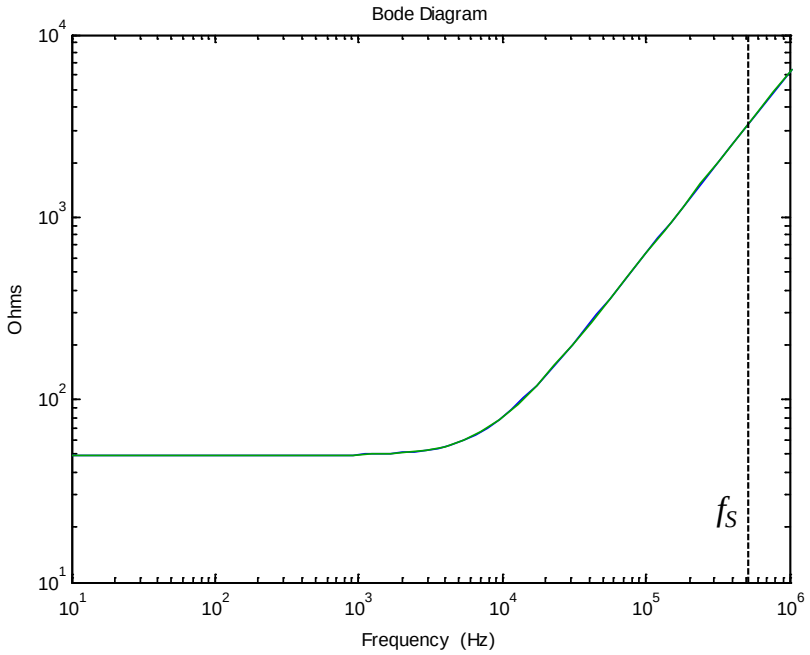


Fig. 3.20 – NLC buck output impedance with (green) and without (blue) sampling effect

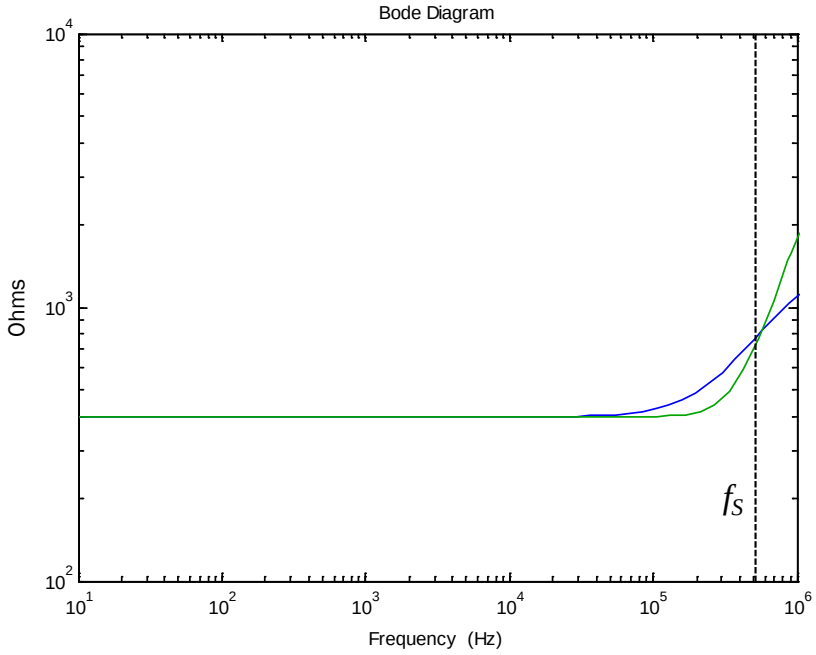


Fig. 3.21 – CPM boost output impedance with (green) and without (blue) sampling effect

For the parameter values used in this work, the high-frequency sampling effect has no discernable impact on the transient response of the NLC buck, and only a minor very high-frequency effect in the CPM boost.

## 3.4 – Conclusions

This chapter presents models and analysis of the CPM boost and NLC buck constant power AC sources, and identifies three major sources of non-idealities encountered in practical power sources. These errors are the peak-to-average error, the artificial ramp-induced error, and the transient error.

Peak-to-average error can be minimized in both converters by selecting a large value of inductor. Artificial ramp-induced error can be minimized by using as small of ramp as possible to maintain stability and provide sufficient noise immunity. In the case of the CPM boost, the bandwidth of the constant power region is not a function of the inductor size, so selecting a large value of $L$ has no impact on the transient response. For the NLC buck, all energy stored in the inductor must be discharged into the load, so minimization of the value of $L$ improves transient response.

# CHAPTER 4

# EXPERIMENTAL VERIFICATION

This chapter presents a hardware prototype of an ESG designed using the converters and control systems introduced in Chapter 2, and further analyzed in Chapter 3. The prototype exhibits the desired steady-state ESG output characteristic at a 50W nominal power setting, and demonstrates excellent transient response. Compared to prior-art resonant inverters, the prototype is shown to have markedly improved per-cycle output power regulation.

An experiment is presented which allows a controlled comparison of tissue results realized using the prototype versus prior-art ESGs. Histological analysis of cut tissue demonstrates a reduction in collateral tissue damage, which is attributed to the prototype's improved transient performance.

## 4.1 – Prototype

Figure 4.1 shows a prototype ESG block diagram. It consists of a DC-DC buck converter which shares an inductor with a DC-AC boost inverter. The input voltage is a constant DC, the converter is non-resonant, and there is an isolation transformer on the output. The prototype utilizes CPM control of the buck converter to produce the desired constant current output ("*I*"), NLC control of the buck converter to produce one portion of the constant power output ("$P_1$"),

CPM control of the boost inverter to produce the remainder of the constant power output ("$P_2$"), and a duty cycle limit on the CPM boost inverter to produce the constant voltage output ("$V$"). The prototype shown here is an improvement over previous prototypes presented in [27, 28].

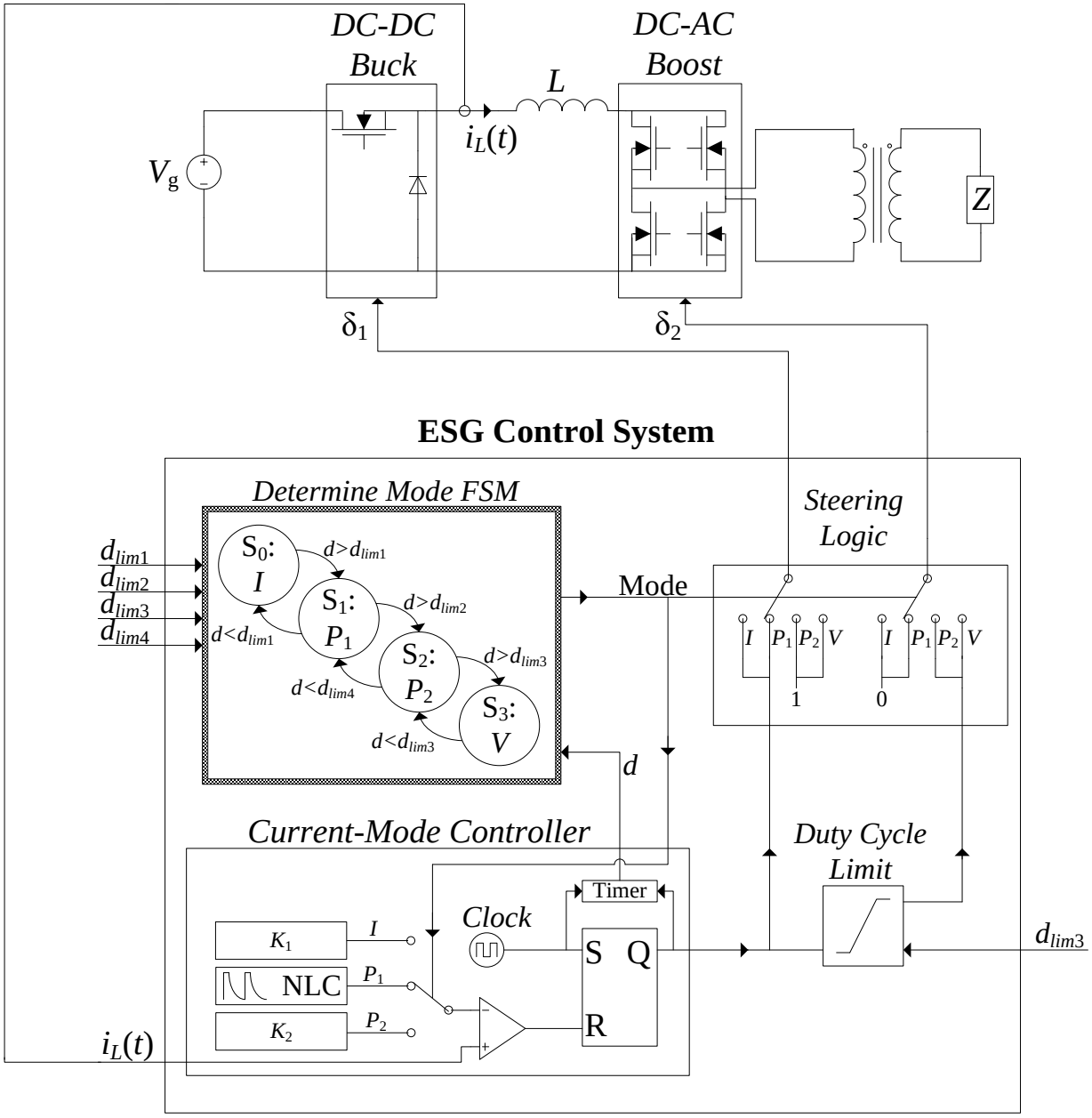


Fig. 4.1 – Block diagram of prototype ESG

Major components in the prototype's power stage are described in Table 4.1.

Table 4.1 – Description of components in power stage of Fig. 4.1

| | |
|---|---|
| $V_g$ | 125 VDC |
| Buck FET | IRFS5620, 200 V, 4.5 A, $R_{ON}$=78 mΩ |
| Buck diode | STTH102A, 200 V, 1 A, $V_f$=0.78 V, $t_{rr}$=20 ns |
| Inductor | 875 μH |
| Boost FETs | SPB04N60C3, 650 V, 4.5 A, $R_{ON}$=0.95 Ω |
| Transformer | 1:2, interleaved |

The power stage components are chosen to achieve a continuous output power of 50 W, and particular attention is given to selecting high-speed switching elements. The value of the shared buck-boost inductor is selected as a reasonable compromise between the conflicting requirements explained in Chapter 3 (large *L* for low peak-to-average error, small *L* for good transient response from buck stage, and large *L* for good transient response from boost stage). The output transformer is interleaved, with a single primary layer sandwiched between two secondary layers, to minimize leakage inductance and the associated ringing against the output capacitance of the boost FETs.

The "ESG Control System" of Fig. 4.1 contains four major blocks. First, a "Current-Mode Controller" block generates a duty cycle command using a periodically clocked S/R latch. It selects between using either a nonlinear carrier or fixed values as the control current limit, depending on which output region the converter is operating in. Second, this duty cycle command is routed to a "Duty Cycle Limit" block, and also to a "Steering Logic" block. The "Duty Cycle Limit" truncates the length of the *d* switching interval to limit the maximum output

voltage to a peak value when in voltage limited mode. Third, the “Steering Logic” block directs the buck and boost stage duty cycles to either the unlimited output of the current-mode controller, the limited output from the duty cycle limiter, or a fixed value (100% or 0%) depending on which mode the converter is operating in. Finally, the “Determine Mode FSM (Finite State Machine)” determines which output mode the converter should be operating in, based on the present mode setting and the value of the converter duty cycle (reported by the current-mode controller, via an ancillary timer).

Figure 4.2 is a photograph of the laboratory prototype constructed to realize Fig. 4.1. The dimensions of the prototype circuit board are 8.1” x 5.25”, the DC input voltage is 125 VDC, and the output power is 50 W.

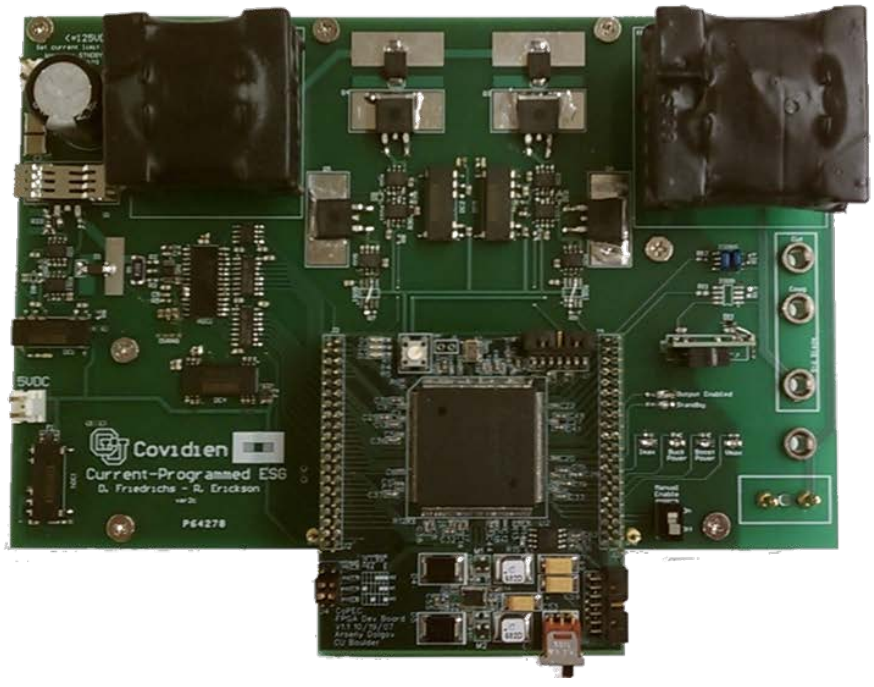


Fig. 4.2 – Photograph of laboratory prototype ESG

The prototype of Fig. 4.2 employs an FPGA to realize all logic contained in the “ESG Control System” block of Fig. 4.1. Figure 4.3 shows a signal-flow diagram of the Verilog code used to realize this functionality.

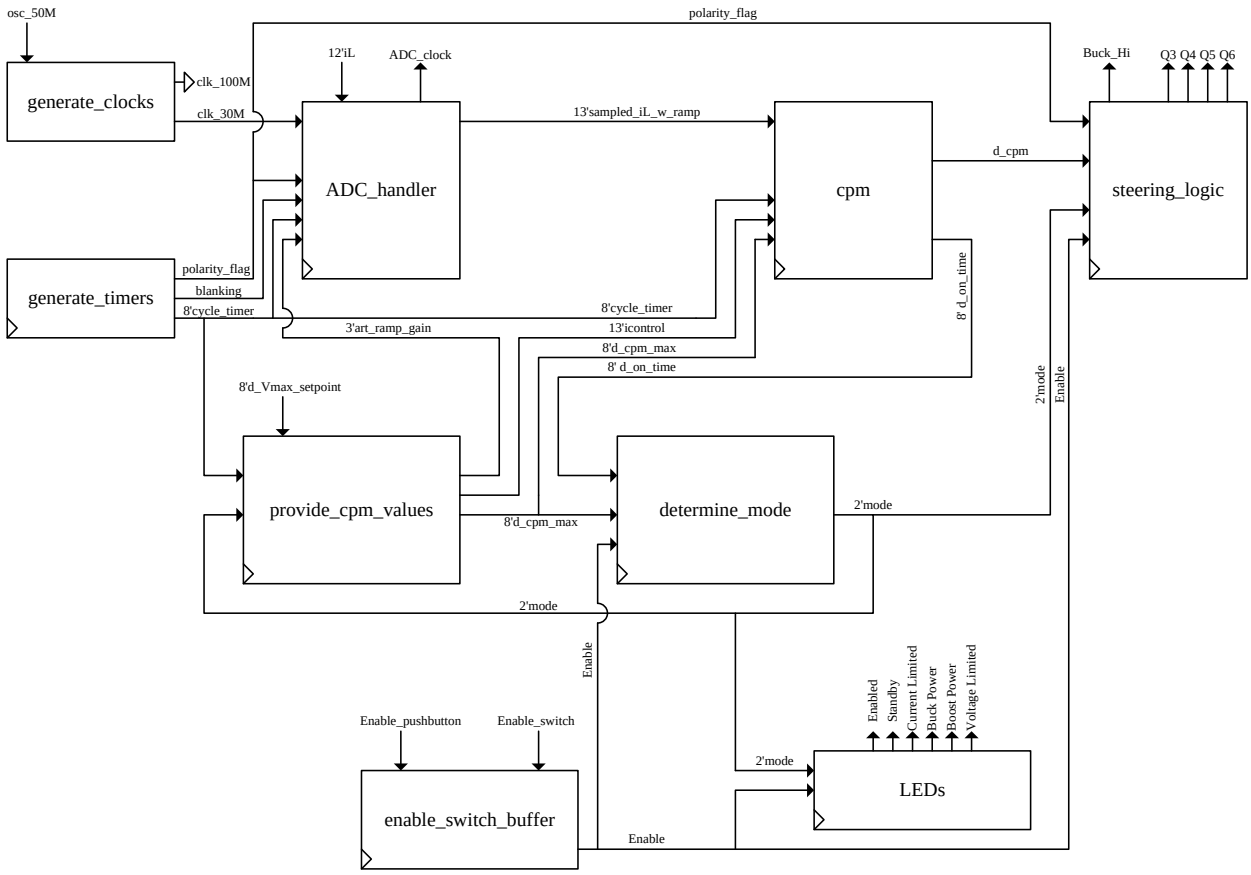


Fig. 4.3 – Signal-flow diagram of Verilog code

The “ADC_handler” block in Fig. 4.3 samples the value of inductor current provided by the ADC and adds an artificial ramp to this signal, depending on which mode the converter is operating in. The “cpm” block compares this signal to the control current limit, which is

provided by the “provide_cpm_values” block. The “provide_cpm_values” block switches between fixed control current limits or the nonlinear carrier control current limit, depending on the operating mode. The operating mode is determined by the “determine_mode” block, which is a finite state machine realizing the same function as the “Determine Mode FSM” block of Fig. 4.1. Finally, the “steering_logic” block realizes the same function as the “Steering Logic” block of Fig. 4.1 by directing either the CPM controller output or a constant value to the power switches, depending on the operating mode.

The Verilog code is synthesized into approximately 365,000 logic gates, filling approximately 75% of the Spartan 3E FPGA. Figures 4.4 and 4.5 illustrate how the sampled inductor current measurements are compared within the FPGA to the control current limit to generate the duty cycle command in NLC buck mode. Figures 4.6 and 4.7 do the same for the prototype operating in CPM boost mode.

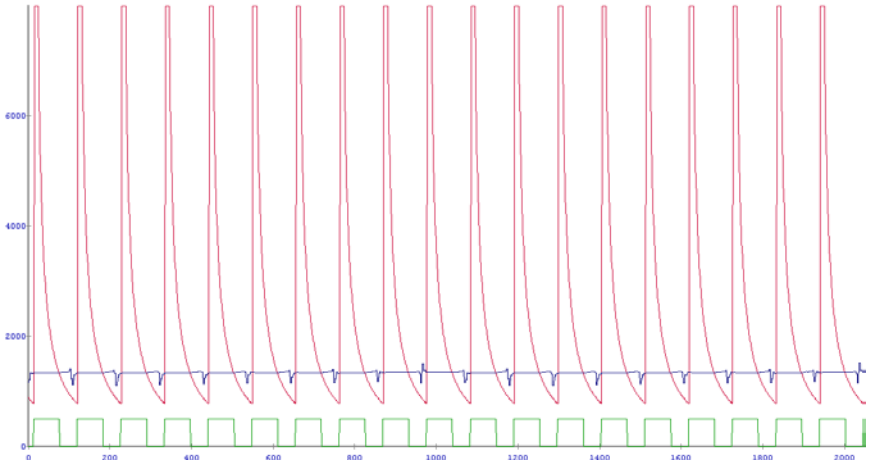


Fig. 4.4 – Nonlinear carrier (red) compared to sampled current (blue) to generate duty cycle command (green)

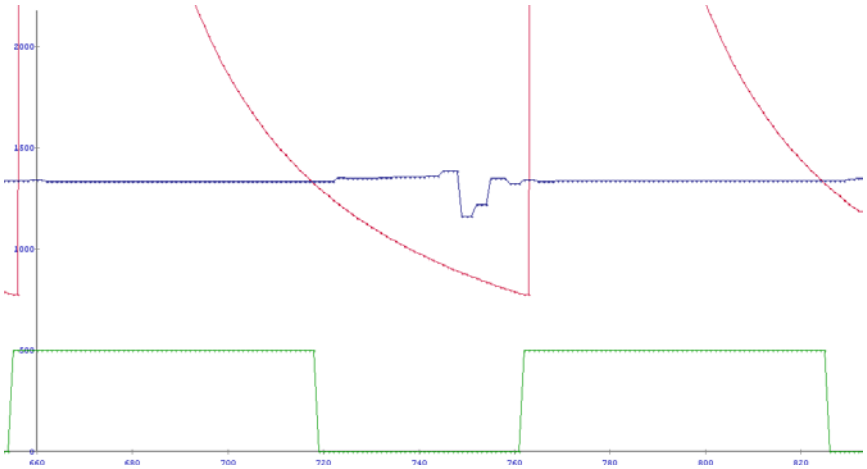

Fig. 4.5 – Zoom of Fig. 4.4 showing number of samples employed

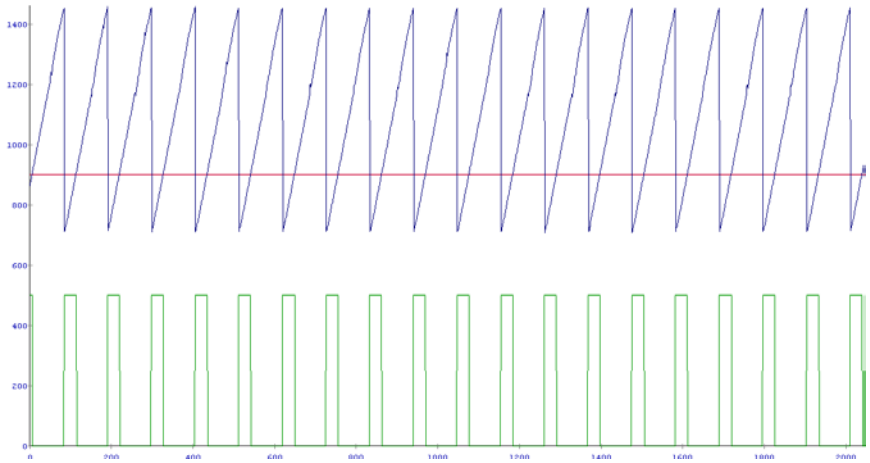

Fig. 4.6 – Control limit (red) compared to sampled current with added ramp (blue) to generate duty cycle command (green)

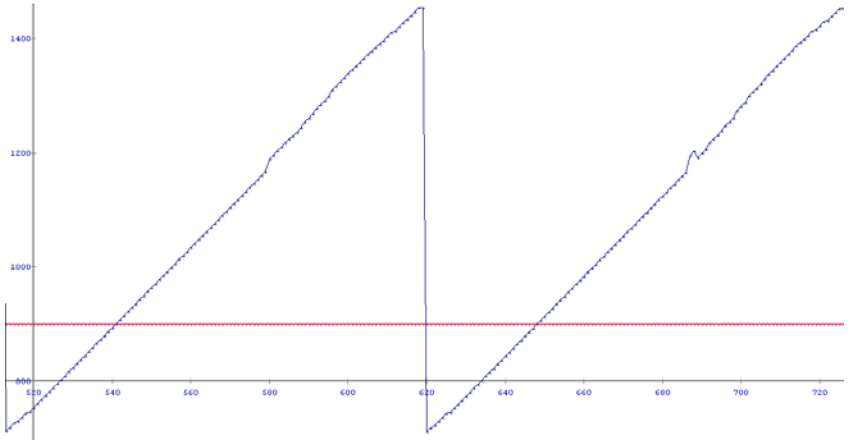


Fig. 4.7 – Zoom of Fig. 4.6 showing number of samples employed

### 4.1.1 – High Speed / High Voltage Gate Drive

The proposed control system relies on the ability to sense inductor current and respond very quickly to achieve output power regulation. Lags or delays in the control system response would introduce undesirable error in output power regulation.

The system of Fig. 4.1 contains five MOSFETs which need to be switched at a high speed with very low propagation delay. Additionally, the voltage being switched by the MOSFETs can reach a peak value of several hundred volts for the chosen design. No commercially-available gate drivers exist which operate at a common mode voltage rage in excess of 400V while simultaneously offering sufficiently high speed switching and low propagation delay. Thus, to utilize the proposed control system, an alternative high-voltage, high-speed, low-propagation-delay gate drive system is employed. For the prototype of Fig. 4.2, the high-side gate drive circuit of Fig. 4.8 is used.

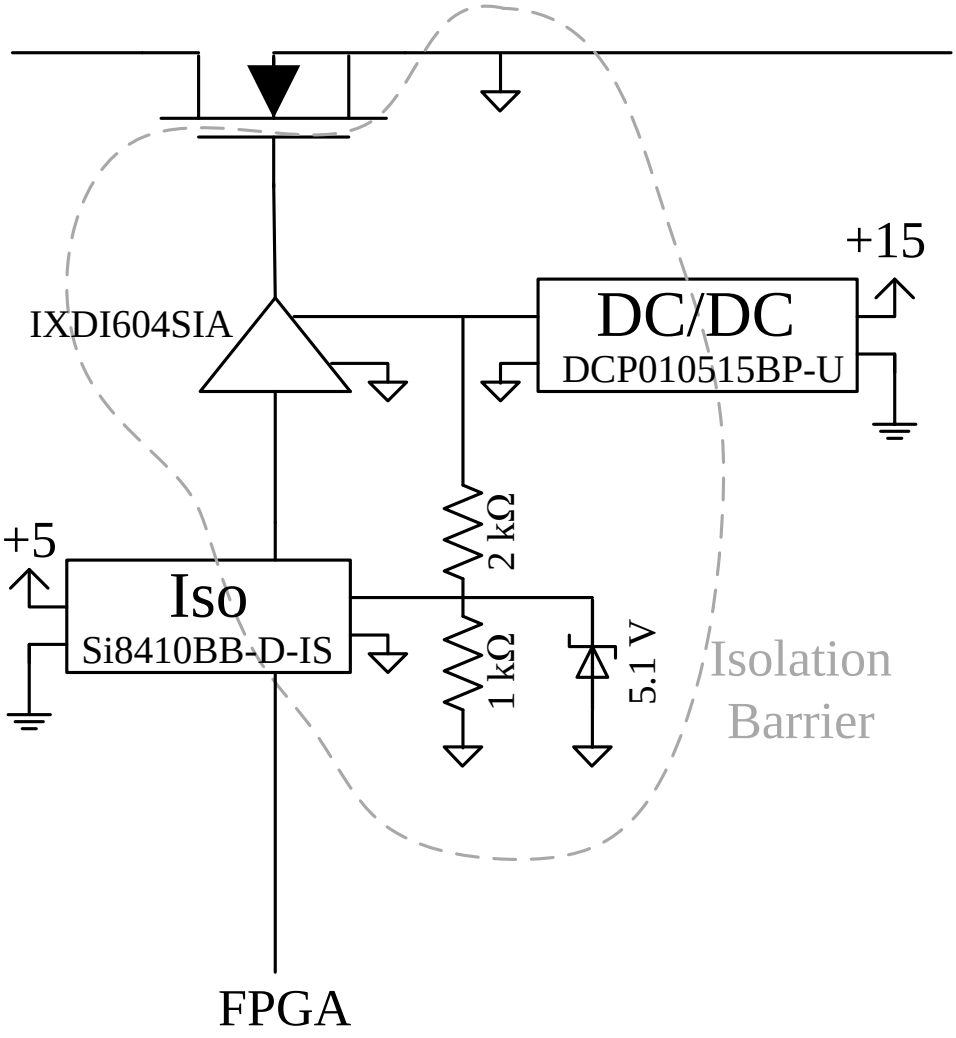


Fig. 4.8 – High speed, high voltage isolated gate drive circuit

In Fig. 4.8, a high-current, high-speed, low-side gate driver is connected to the MOSFET gate. A 1.5kV-isolated DC/DC converter is used to float the gate driver supply above earth ground by supplying +15VDC (relative to the MOSFET source) to the gate driver supply pin. The logic signal to the gate driver cannot be directly connected, as the gate driver ground is now

uncommon with the FPGA ground. Instead, a 2.5kV-isolated RF isolator is employed to pass the FPGA logic signal. This isolator exhibits only minor (~1ns) propagation delay.

The RF isolator requires an isolated +5V supply (relative to the MOSFET source). A second isolated DC/DC converter could be employed for this purpose, but they are expensive and bulky. Because the power consumption of the RF isolator is very low, a linear regulator could reasonably be connected to the output of the +15V DC/DC converter to generate a +5V supply. Given the very low power consumption of the RF isolator, an equally reasonable solution is to use a resistor divider and zener shunt to supply the +5VDC.

Figure 4.9 shows the FPGA gate drive logic signal going high (magenta), and the MOSFET gate-source voltage (blue) responding within approximately 60ns. This demonstrates that high-speed low-latency gate driving is achieved using the circuit of Fig. 4.8.

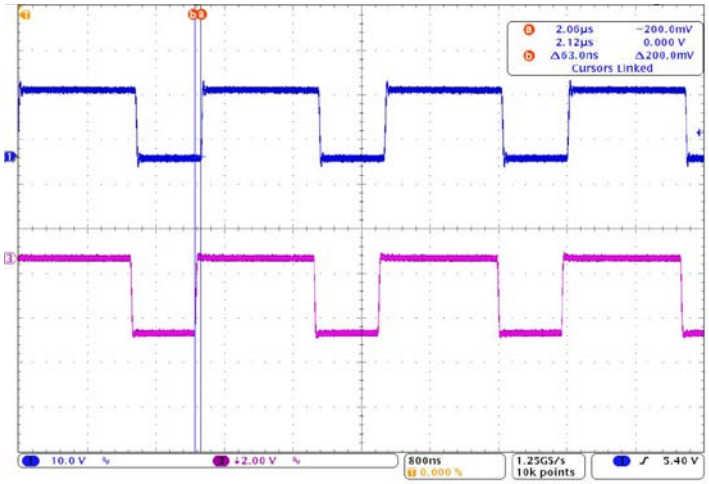


Fig. 4.9 – Gate drive logic (magenta) and MOSFET gate-source voltage (blue)

## 4.2 – Steady-State Response

The steady-state performance of the converter is evaluated by connecting to load impedances ranging from 0 Ω to 7.5 kΩ and recording RMS output voltage and current measurements, to produce the (*i*, *v*) plot shown in Fig. 4.10.

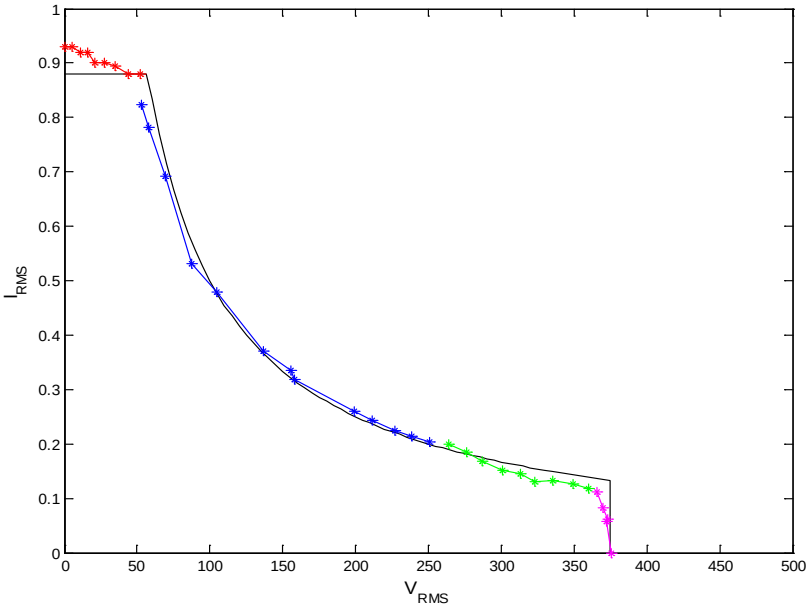


Fig. 4.10 – Output (*i*, *v*) plot for laboratory prototype ESG

As shown in Fig. 4.10, the prototype successfully produces the desired ESG output characteristic (shown in black) using a CPM buck converter to produce a constant current limit (red line), a NLC buck converter to produce a portion of the constant power source (blue line), a CPM boost inverter to produce the remainder of the constant power source (green line), and a duty cycle limit on the CPM boost inverter to produce the maximum voltage limit (magenta line).

Figure 4.10 shows a maximum output current of approximately 0.88 $A_{RMS}$, a maximum output voltage of 375 $V_{RMS}$, a peak output voltage of 650 $V_{PK}$, and 50 W of power delivered over

a wide range of load impedances of interest in electrosurgery. These values are all typical and reasonable for monopolar ESGs operating at this power level.

## 4.3 – Transient Response

While Fig. 4.10 demonstrates the desired steady-state output ($i$, $v$) characteristic, other commercially-available ESGs can produce similar curves in the steady-state. To judge improvement in per-cycle output power regulation, transient response is evaluated. Figure 4.11 shows the result of a load step applied to the laboratory prototype ESG, where the loads are low-inductance resistors, and the step is manually effected using a knife switch.

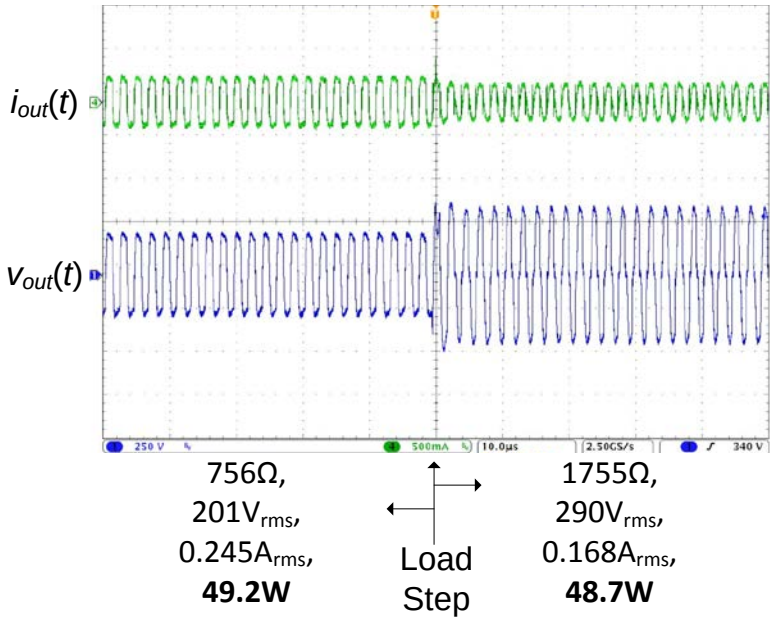


Fig. 4.11 – Load step of laboratory prototype ESG operating in CPM boost mode

In Fig. 4.11, the converter steps from 756 Ω to 1755 Ω and achieves regulation within 5 µs; only one or two output cycles appear even mildly distorted. The prototype ESG is operating in CPM boost mode for both load impedances in Fig. 4.11.

Figure 4.12 shows a load step where both loads are in the NLC buck region.

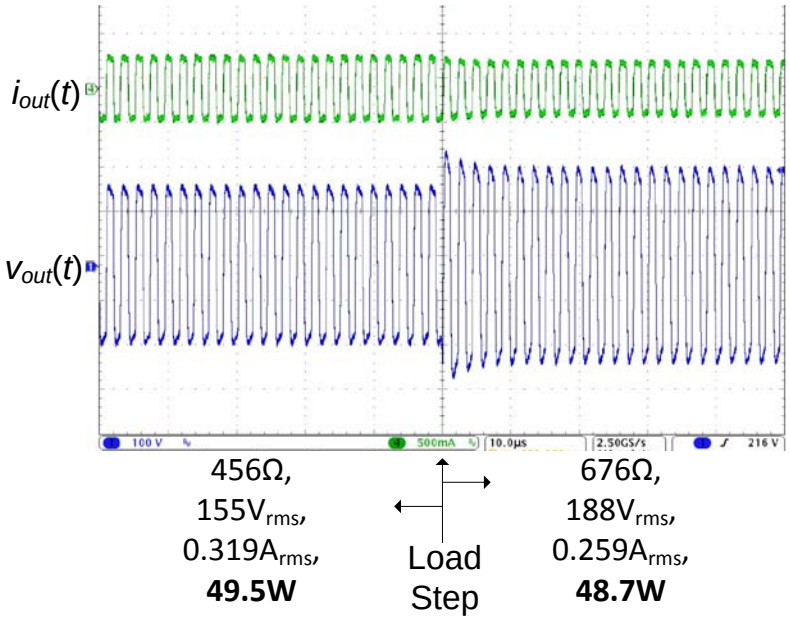


Fig. 4.12 – Load step of laboratory prototype ESG operating in NLC buck mode

In Fig. 4.12, the converter steps from 456 Ω to 676 Ω and the converter again achieves regulation within 5µs, or only a few output cycles.

Load steps that cause transitions between the two constant-power regions also occur quickly, and are demonstrated in Figs. 4.13 and 4.14.

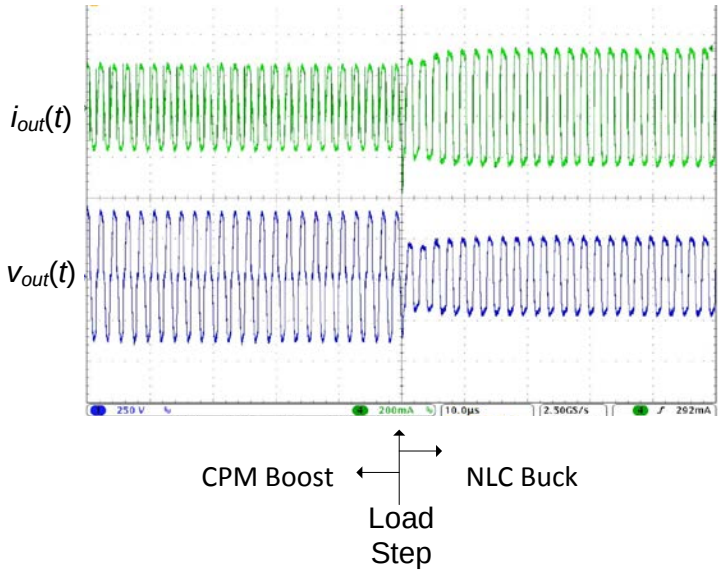


Fig. 4.13 – CPM boost to NLC buck load step

In Fig. 4.13, the prototype steps from 1755 Ω (CPM boost mode) to 676 Ω (NLC buck mode), and achieves regulation within 20 µs.

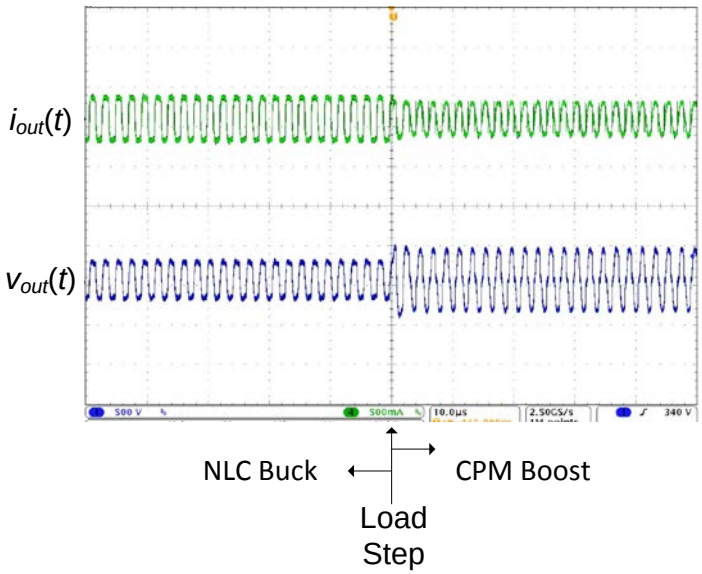


Fig. 4.14 – NLC buck to CPM boost load step

In Fig. 4.14, a step occurs in the opposite direction (676 Ω to 1755 Ω), triggering a transition from CPM boost mode to NLC buck mode which achieves regulation within 2 µs.

## 4.4 – Voltage and Current Limiting

Maximum voltage and current limits also occur quickly in response to a change in load impedance. Figure 4.15 shows load steps which cause transitions to and from voltage limited mode, and Fig. 4.16 shows load steps which cause transitions to and from current limited mode.

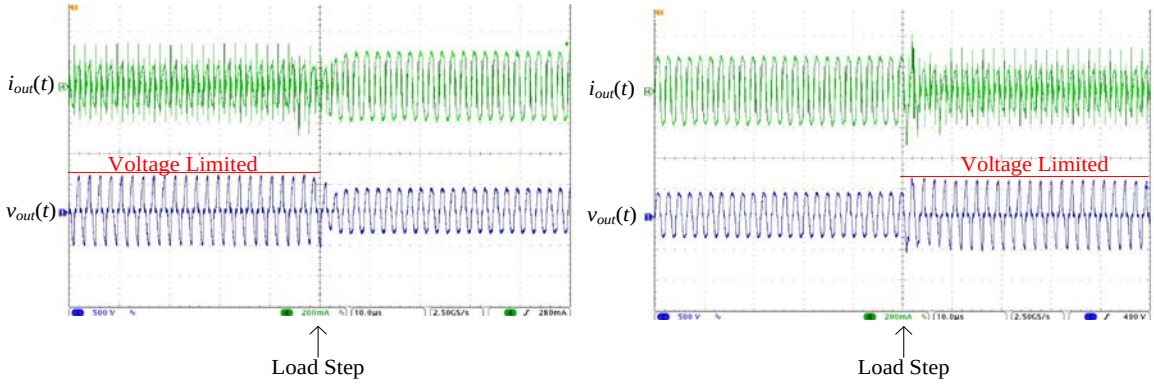


Fig. 4.15 – Transitions to and from voltage limited mode

In Fig. 4.15, the load switches between 5 kΩ (voltage limited) and 1755 Ω (CPM boost power source). When transitioning from voltage limited to constant power, the converter regulates within 10 µs. When transitioning from constant power into voltage limited mode, the converter achieves voltage limiting instantly, without any voltage overshoot.

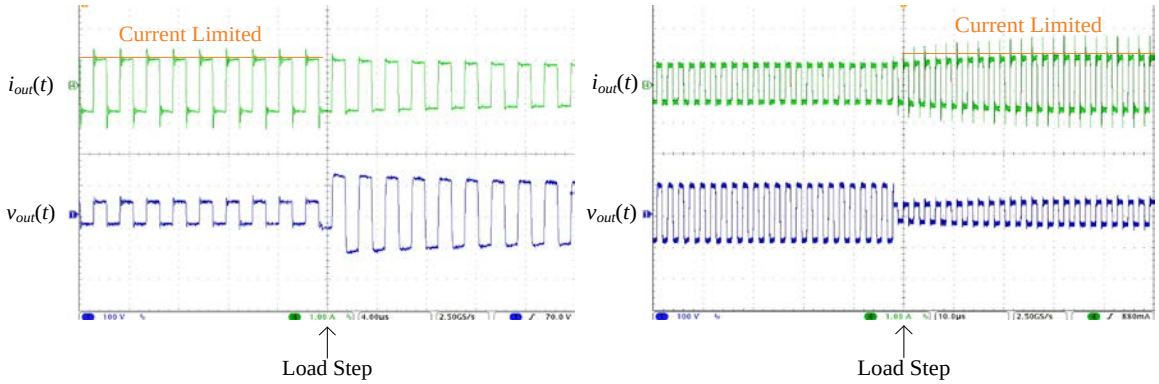


Fig. 4.16 – Transitions to and from current limited mode

In Fig. 4.16, the converter switches between 22 Ω (current limited) and 61 Ω (NLC buck power source). In both cases, regulation is achieved within 40 μs, with no overshoot in output current.

## 4.5 – Per-Cycle Output Power Analysis

The prototype converter demonstrates the desired steady-state output characteristic and very fast transient response to load steps. It is desired to evaluate how well the prototype converter regulates per-cycle output power when used in a clinical application, when load impedance rapidly changes in response to varying tissue impedance and arcing. Per-cycle output power regulation is a direct indicator of the consistency of the tissue effect, so quantifying this measure is useful.

To emulate tissue impedance changes similar to those encountered clinically, galline muscle tissue was dissected. Galline or porcine tissue is commonly used to evaluate the performance of ESGs, as it has similar electrical properties to other animal and human tissues. Dissection was manually done using a standard flats-coated monopolar electrosurgical blade,

using a typical cutting speed (approximately 10 cm/s) and depth-of-cut (approximately 1 cm). Output voltage and current measurements were simultaneously taken from the ESG and imported into MATLAB for post-processing. From this data, per-cycle output power is computed and expressed as a histogram. Data was taken for numerous activations of the ESG, until the per-cycle output power histogram ceased to change shape and the data is uniform enough to ensure repeatability.

This test was performed using two commercially-available ESGs, as well as the laboratory prototype. Figure 4.17 shows the per-cycle output power histogram of a Covidien ForceFX, which is a resonant inverter-based ESG (as described in Section 1.4), with a low-speed control loop.

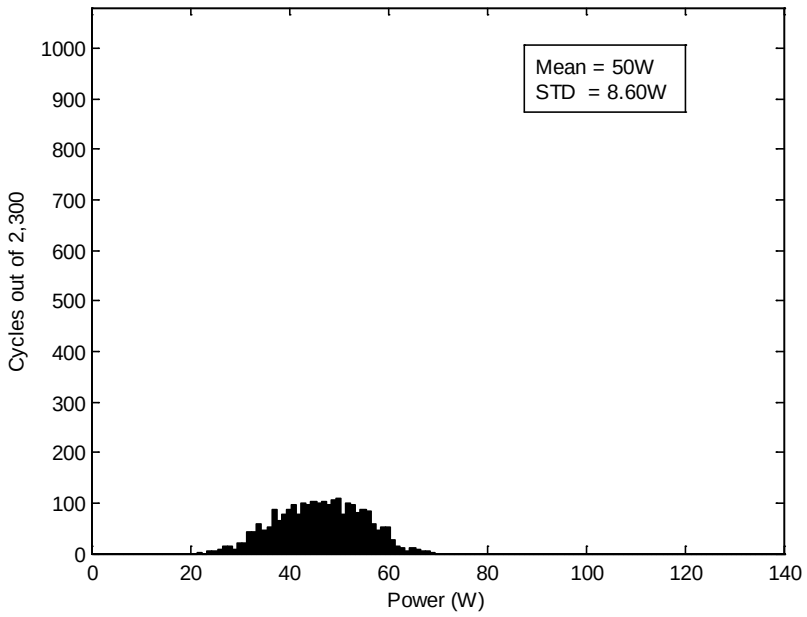


Fig. 4.17 – Per-cycle output power histogram from Covidien ForceFX

Figure 4.17 shows that the standard deviation in per-cycle output power delivered by this commercially-available ESG is 8.6 W, and shows crude clustering around the requested (50 W) output level. Figure 4.18 shows a per-cycle output power histogram from a Covidien ForceTriad, which is also a resonant inverter-based ESG, but employs a control loop operating at approximately twice the speed of the ForceFX.

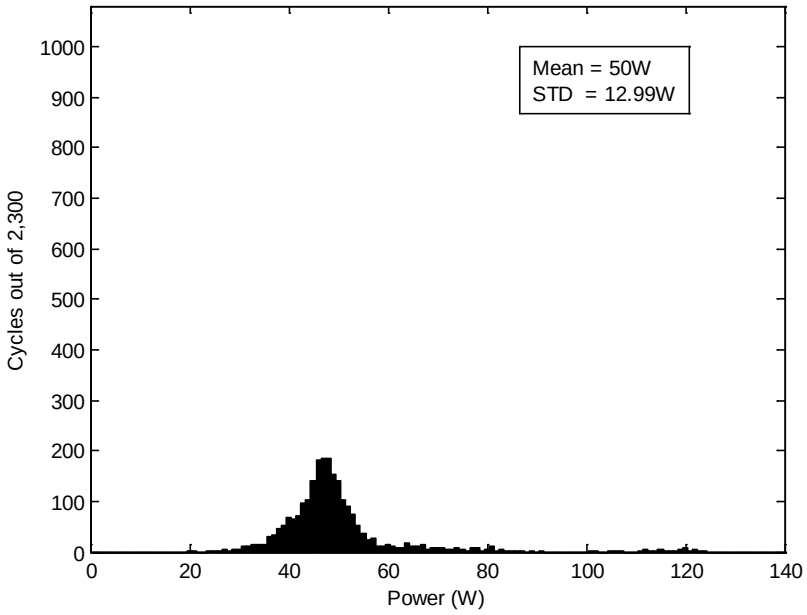


Fig. 4.18 – Per-cycle output power histogram from Covidien ForceTriad

For the ForceTriad, clustering around the request (50 W) power level is more obvious, but several outlying cycles (some in excess of 120 W) caused the standard deviation in output power to be higher, at 13 W. Figure 4.19 shows the per-cycle output power histogram from the laboratory prototype.

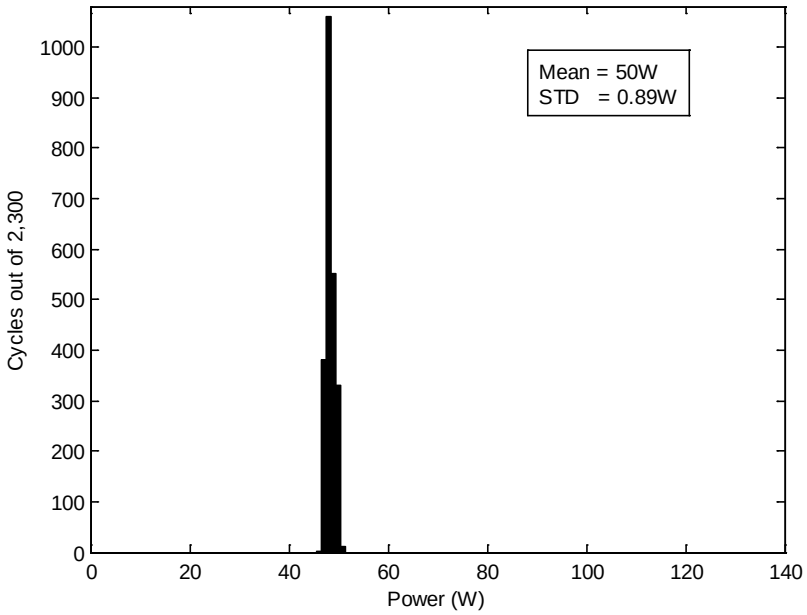


Fig. 4.19 – Per-cycle output power histogram from laboratory prototype

The laboratory prototype shows significant improvement in per-cycle output power regulation, with a standard deviation of only 0.89 W.

## 4.6 – Experimental Verification of Decreased Thermal Spread

This work argues that regulation of per-cycle output power is a major indicator of the degree of thermal spread evident in electrosurgically cut tissue. Sporadic excessive output power contributes little to the speed of cutting, but results in extra available energy which must be absorbed by the tissue, increasing the volume of tissue that is thermally coagulated. While some thermal coagulation is often desirable (for hemostasis), it is preferable to increase thermal spread by increasing the ESG maximum output voltage, rather than accepting thermal spread as an unavoidable by-product of poor output power regulation.

To test the hypothesis that improved per-cycle output power regulation leads to decreased thermal spread, an experiment is devised which allows direct measurement of thermal spread on test tissue. Tissue is cut using monopolar electrosurgery and then thermal spread identified and measured directly. Since thermal margins can be as shallow as a few cellular layers [29], this requires histological tissue analysis techniques.

Histological samples are prepared by slicing tissue to only several microns thick for microscopic examination. Minor variations in the speed- or depth-of-cut, or variations in tissue composition, could cause such a small section of tissue to show results that are inconsistent from the average appearance of all tissue in the sample. While the averaged appearance of many sections may lead to useful results, this may be an intractable problem if large numbers of tissue samples are needed to establish the average appearance of the sample. The problem can be simplified by attempting to restrict other variables in the experiment, such that only the ESG power regulation contributes to variations in cut tissue appearance. Variables which significantly affect thermal spread are speed of cut, depth of cut, and tissue composition.

To control tissue composition, porcine liver tissue was selected, as this tends to have a very uniform histological appearance. This selection still presents variable tissue impedance, though, as even consistent liver tissue contains uniformly-spaced lobules and veins. Established models recognize that thermal damage in such tissue will manifest as denaturation of collagen [30], which can be selectively stained for easy visual identification. To control speed- and depth-of-cut, the apparatus of Fig. 4.20 is used.

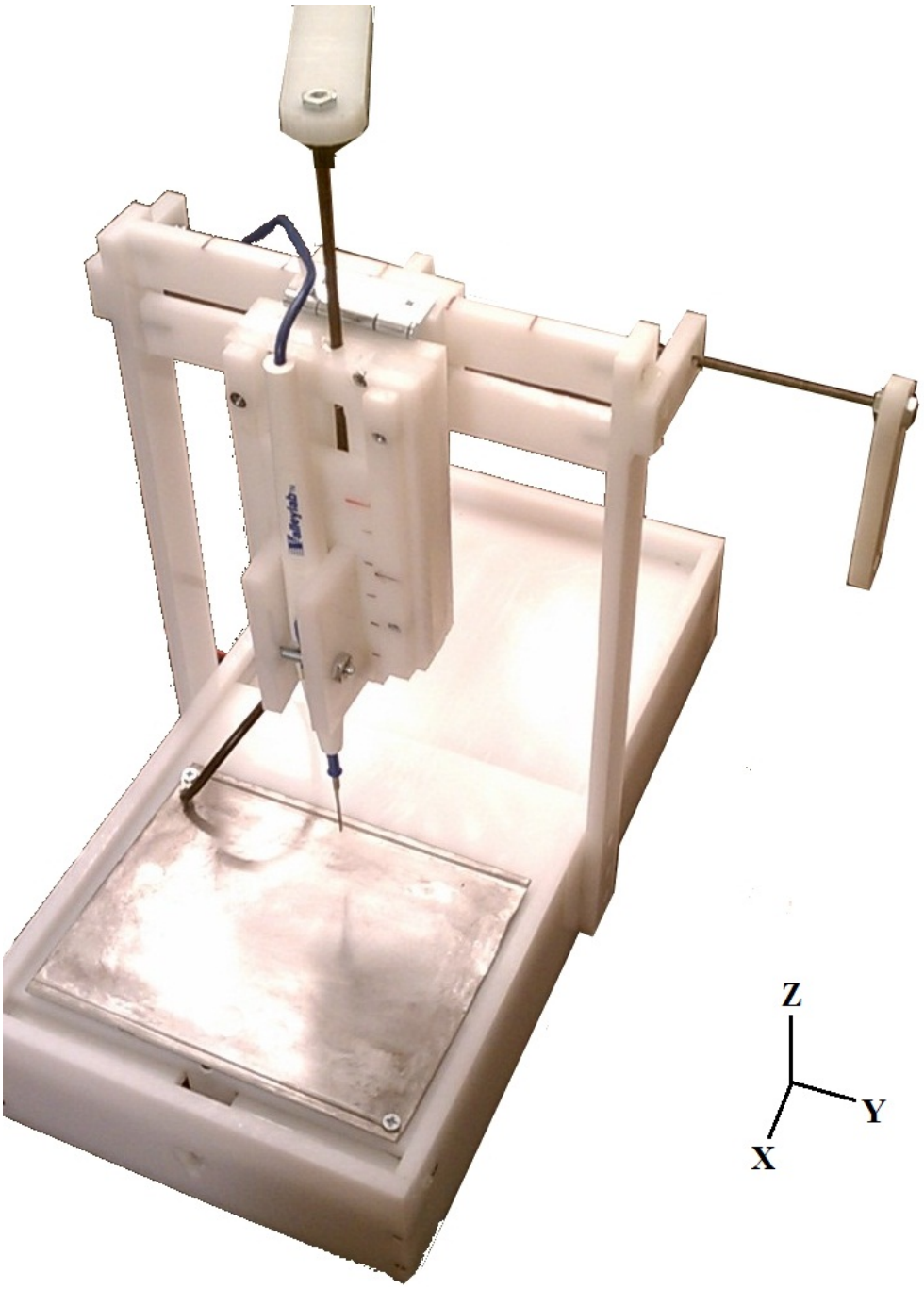


Fig. 4.20 – Photograph of constant-speed and -depth tissue cutting apparatus

The apparatus of Fig. 4.20 mounts a monopolar electrosurgical blade above a stainless steel table, upon which the tissue to be cut is placed. A DC motor mounted under the table moves the table along the x-axis at a constant speed of approximately 10 cm/s, typical of the speed used

by a human operator. The blade can be accurately and repeatably positioned in the y- and z-planes via positioning leadscrews and indexing marks. Use of this apparatus to produce cuts in test tissue significantly increases the consistency of the speed and depth of cuts over what could be achieved free handed, and use of such constant-cutting-speed apparatuses is a common technique in similar experiments [31].

A fresh porcine liver was acquired (fresh tissue is necessary to ensure that histologically observed tissue necrosis is the result of electrosurgical heating, not merely animal death), and uniform sections were excised and placed on the testing apparatus. Cuts of various depths (approximately 0.5 cm, 1 cm, and 1.5 cm deep) were made using the laboratory prototype and two commercially-available ESGs. The cut tissue sections (of approximately 15 $cm^3$ each) were then excised with a scalpel, placed in 90mL Formalin-filled sample containers, and stored for 24 hours at 4°C. After formalin fixing, tissues were washed in phosphate-buffered saline solution, and stored at room temperature in 70% histological-grade ethanol for shipment to the histology facility.

Figs. 4.21 – 4.23 show the result of histological analysis of the tissue, as prepared by the collaborating histology laboratory [33]. The samples were stained with a pentachrome staining agent, where necrotic (thermally damaged) tissue appears as a yellow or blue color, and undamaged tissue appears red. Comparisons are shown between the laboratory prototype, a Covidien ForceTriad, a Covidien ForceFX, and a cold scalpel, and magnifications are shown at 4x, 10x, and 20x.

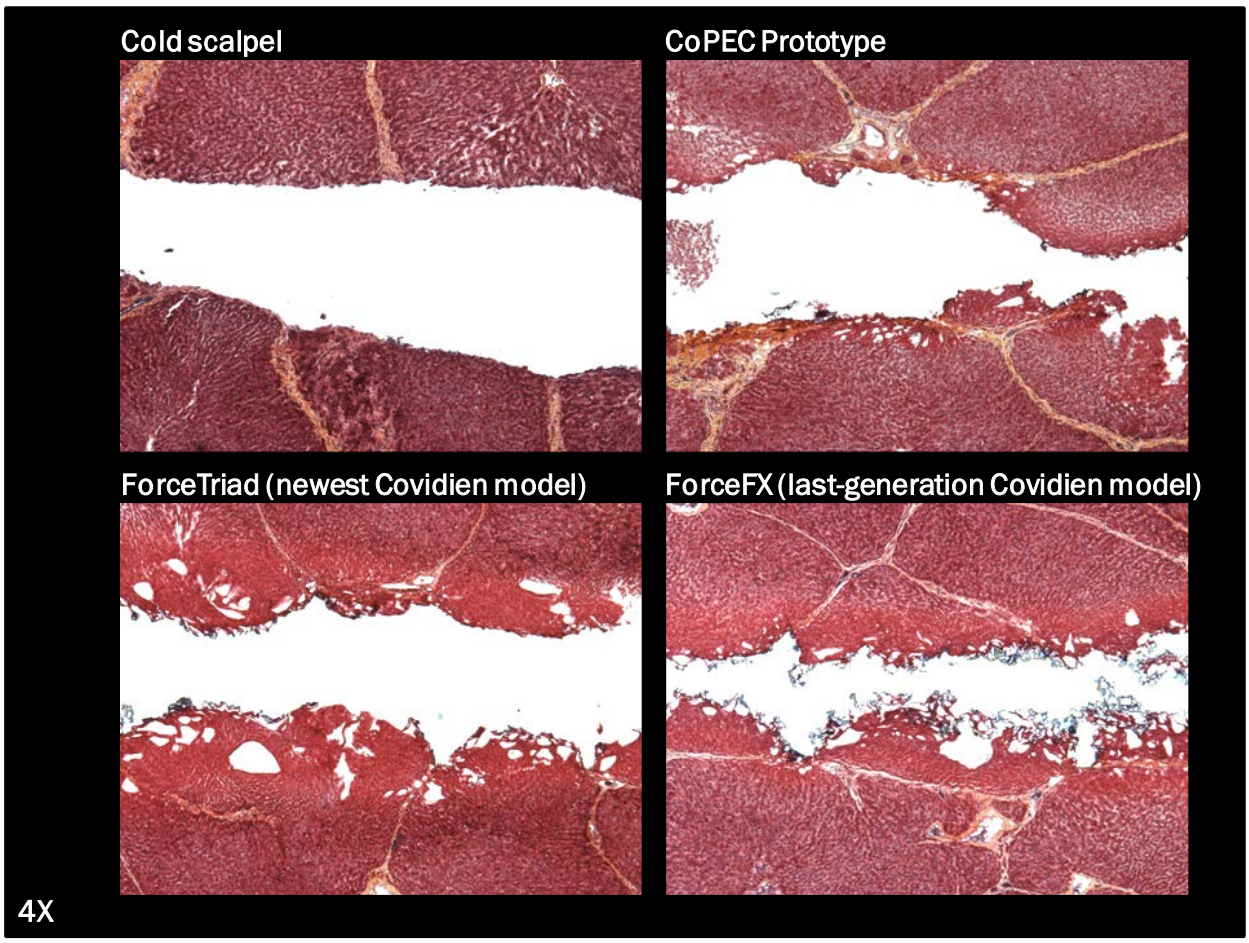


Fig. 4.21 – Histology samples at 4x magnification

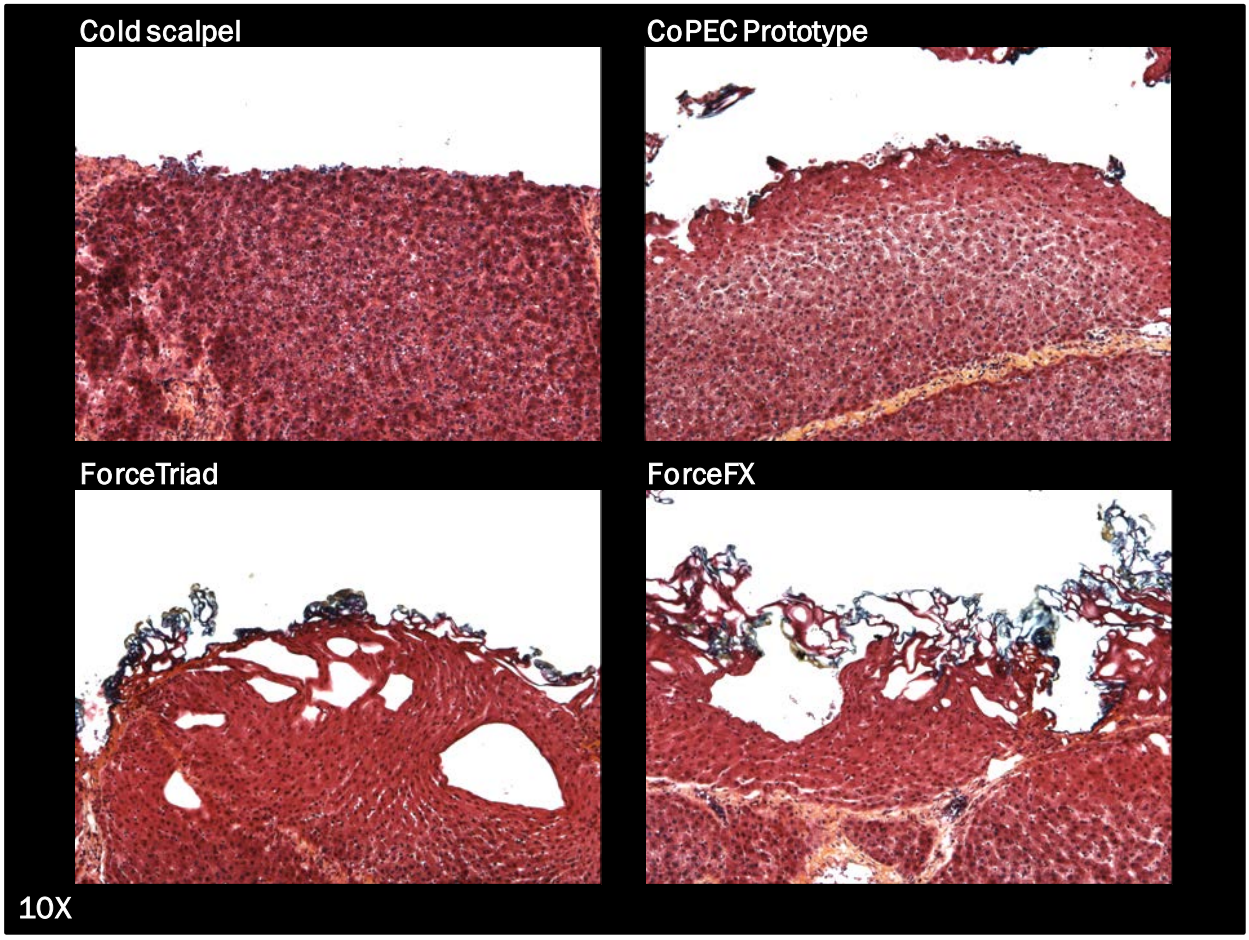


Fig. 4.22 – Histology samples at 10x magnification

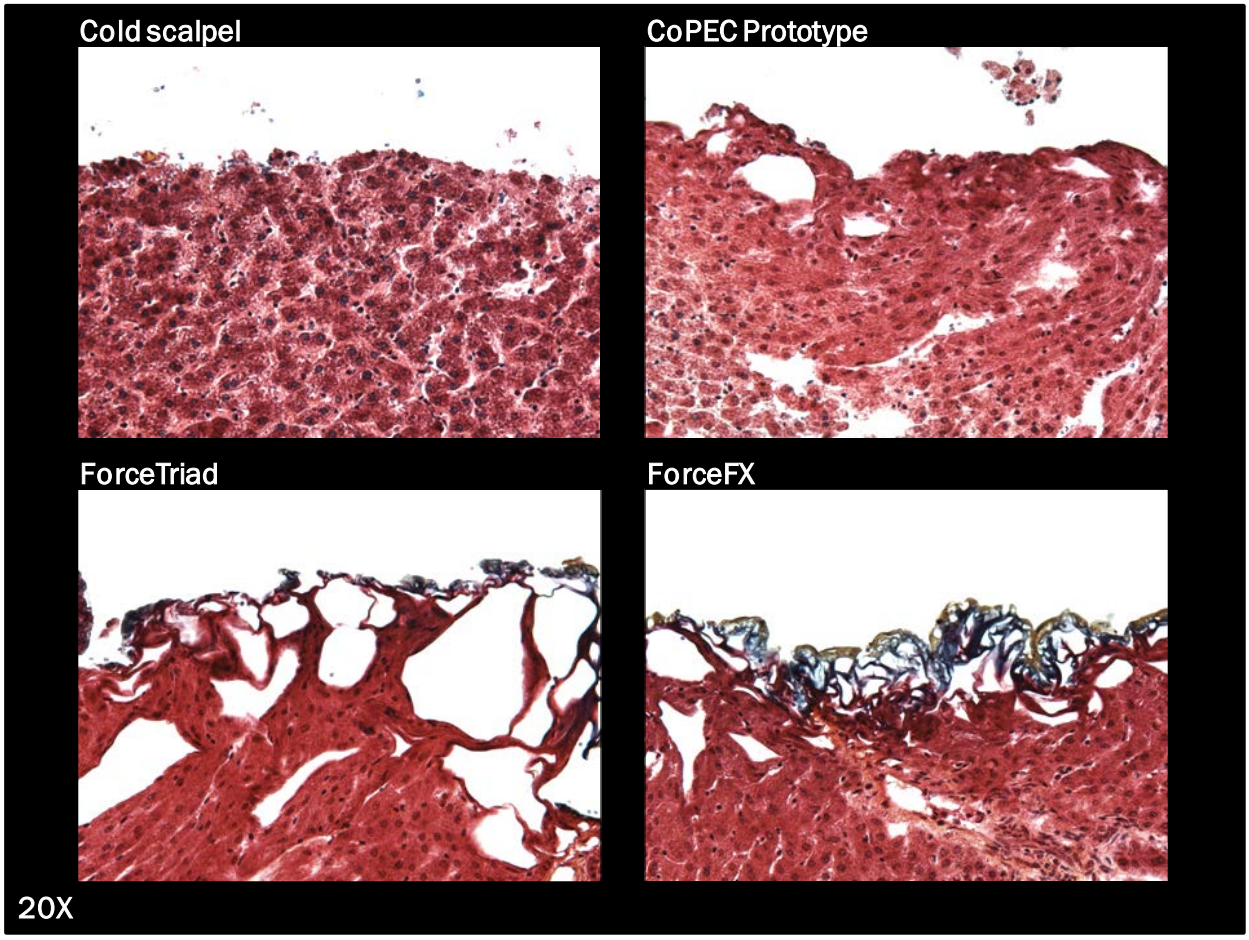


Fig. 4.23 – Histology samples at 20x magnification

Figures 4.21-4.23 clearly show that the laboratory prototype demonstrates significantly decreased thermal spread from either commercially-available unit, as evidenced by decreased volumes of blue and yellow-stained (necrotic) tissue. Blinded evaluation of the samples by an independent liver biologist confirmed this conclusion, agreeing that all cut margins exhibited reduced tissue necrosis. Figures 4.21-4.23 are presented as representative examples of the tissue effect consistently observed over a large number of prepared samples.

While the necrotic tissue margins in the electrosurgical cuts of Figs. 4.21-4.23 are only a few cellular layers wide, even minor reductions in collateral tissue damage have valuable, appreciable clinical effects. Reductions in collateral tissue damage are reported in the literature for other surgical technologies [34, 35], with claims that cold scalpel incisions are universally superior across several metrics of comparison. Figures 4.21-4.23 demonstrate that the prototype ESG performs similarly to a cold scalpel, thus realizing a clinically-appreciable improvement in surgical outcomes.

The prepared histological specimens also demonstrated a decreased number of incurred air bubbles: an unexpected (but desirable) finding. As tissue is vaporized, a mechanical pressure wave propagates through the residual tissue, occasionally forcing gas bubbles into the interstitial space. These incurred bubbles are undesirable, as they must be absorbed and thus retard healing. The prototype converter demonstrates reduction in incurred gas bubbles.

Through a controlled tissue-cutting experiment and histological analysis of the cut specimens, it is shown that the prototype ESG significantly reduces collateral tissue damage. This improved result is attributed to the superior transient response of the prototype ESG. A correlation between output power regulation and thermal damage was previously unknown to the literature, but is a significant finding, given the magnitude of the observed clinical effects. This conclusion is expected to be of considerable interest to ESG manufacturers, who have previously underestimated the importance of ESG transient response.

## 4.7 – Conclusions

A prototype ESG is constructed employing the proposed CPM control methods to obtain a device that inherently produces the ideal ESG output characteristic. The high-speed feedback loop results in excellent transient response, with the converter regulating load steps in less than ten cycles. Voltage- and current-limited modes are invoked equally quickly. Transitions between the two constant-power stages are clean and expedient, and allow constant power source coverage of a full range of load impedances of interest in monopolar electrosurgery.

Experimental results demonstrate that this high-speed control results in excellent per-cycle output power regulation, with the prototype demonstrating a standard deviation in per-cycle output power of less than 1 W (compared to ~10 W observed in commercially-available units). Histological analysis of cut porcine tissue proves that per-cycle output power regulation directly correlates to decreased thermal spread and tissue damage. Thus, this prototype has demonstrated significantly improved clinical effects through the application of high-speed output power regulation. Also notably, compared to prior-art resonant inverter-based designs, the laboratory prototype is a markedly simpler design, as it has no large tank components, and requires only a single current sensor to operate the entire system (compared to an output voltage and current sensor required by the prior art).

# CHAPTER 5

# REALIZING NON-CUTTING WAVEFORMS WITH CONTINUOUS OUTPUTS

## 5.1 – Introduction to Non-Cutting Waveforms

While monopolar electrosurgery is frequently used for dissecting tissue, increasing the maximum voltage limit causes significantly different tissue effects, which are also frequently desired. Increased peak voltage causes increased arcing from the tip of the electrosurgical instrument, effectively changing the contact geometry of the tool. In general, higher peak voltages lead to greater thermal spread, greater tissue charring (black coagulation), and shallower depth of cut. Clinically, this type of output is used to intentionally increase thermal spread (for increased hemostasis) or to fulgurate tissue (vaporizing large volumes of surface tissue with arcs). Figure 5.1 illustrates different tissue effects achieved with higher peak voltages (but same average power).

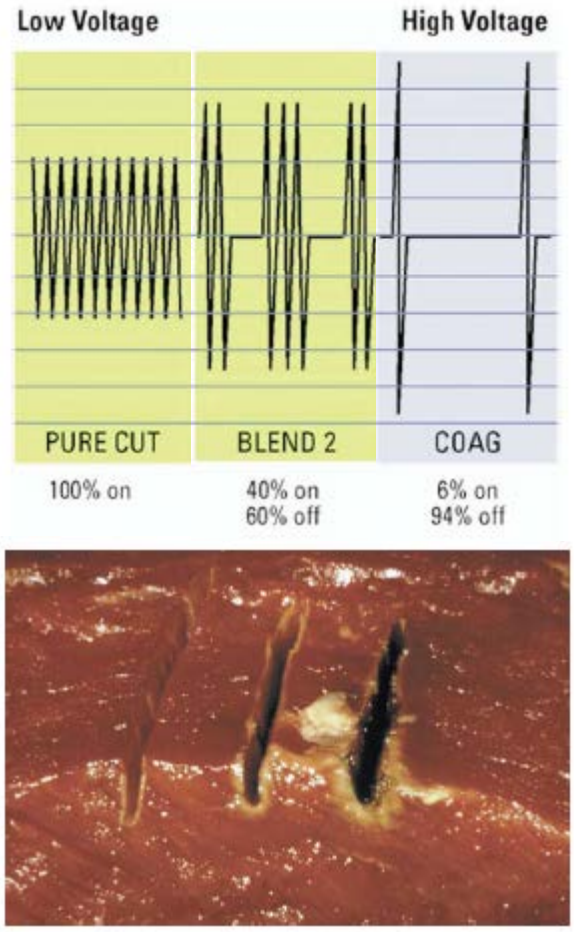


Fig. 5.1 – Different tissue effects achieved with different peak voltage but same average power

*Illustration courtesy Covidien*

With prior-art resonant inverters, production of high voltage outputs requires increasing the size of the elliptical output characteristic, which consequently also increases the average output power. To achieve variation in peak output voltage with constant average output power, the output waveform is modulated, as shown in Fig. 5.1.

As output voltages increase, the likelihood of arcing increases. Additionally, for these non-cutting modes, surgeons tend to hold the instrument a small distance away from the tissue in

order to intentionally strike arcs. When used in this manner, the load characteristic of tissue/tool interface begins to resemble a spark gap, with an (*i*, *v*) characteristic similar to Fig. 5.2.

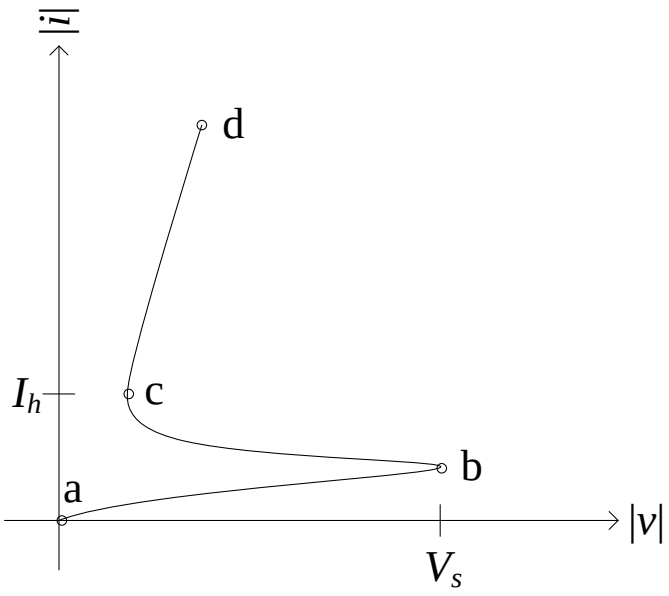


Fig. 5.2 – Spark gap (*i*, *v*) curve

To strike an arc, a peak switching voltage ($V_s$) must be reached. From points "b" to "c" in Fig. 5.2, a negative resistance region is encountered until the holding current ($I_h$) is reached. From points "c" to "d", a non-thermal positive-resistance region exists until the ESG commutates its output, extinguishing the arc.

Figure 5.3 demonstrates how prior art resonant inverters may achieve sufficiently high peak voltage and the desired average output power, but Fig. 5.4 illustrates how requesting a high voltage may result in excessive average output power.

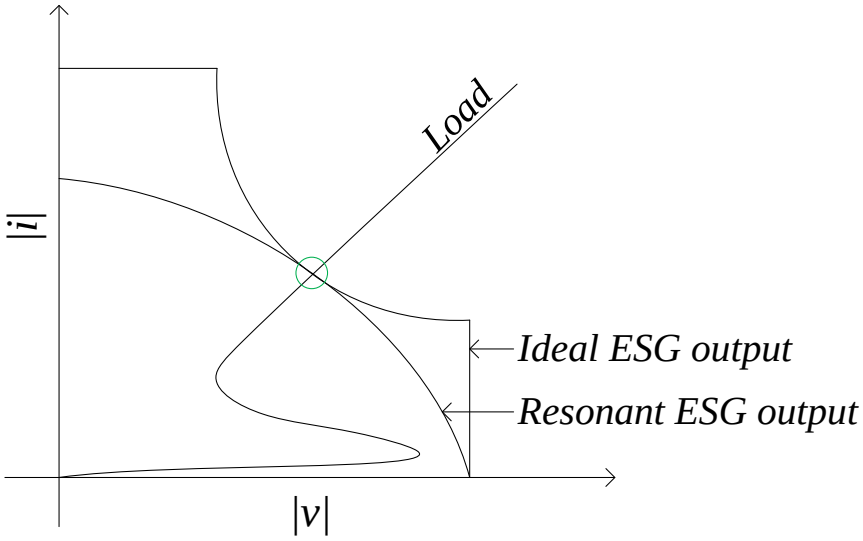


Fig. 5.3 – Sufficient $V_{pk}$ to strike arc, and correct average output power

In Fig. 5.3, the peak switching voltage requested by the load line is enclosed within the resonant ESG output ellipse; thus, an arc is struck. A steady-state operating point is then established at the intersection of the load line and the output ellipse, which also happens to intersect with the constant power hyperbola.

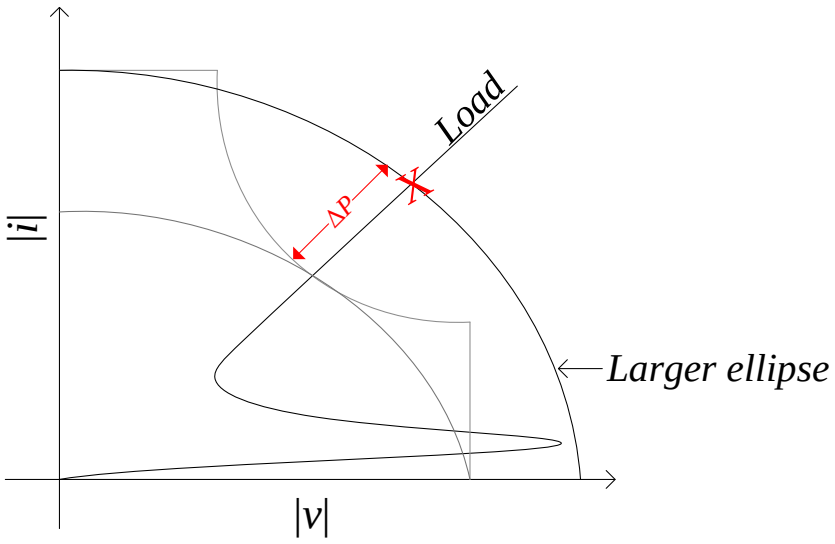


Fig. 5.4 – New, higher $V_{pk}$ required to strike arc results in excessive average output power

In Fig. 5.4, the elliptical output characteristic of the resonant inverter is enlarged to encompass a load-line which requires a higher peak voltage to initiate an arc. As a consequence, excessive average power is delivered, as the load line now intersects the ellipse at a point that does not also intersect the constant power hyperbola. To avoid this, prior-art resonant inverters achieve high peak voltages with low average output power by modulating the output, as shown in Fig. 5.1. The need to construct an efficient power stage capable of variable-frequency modulation of the output complicates the ESG design considerably.

## 5.2 – CPM-Based Alternative Methods of Producing Non-Cutting Waveforms

The CPM controlled series buck-boost topology presented in this thesis offers a simple alternative to modulating the output of a resonant inverter. The series buck-boost has two degrees of control freedom, allowing production of continuous (non-modulated) output waveforms with arbitrary peak output voltage and average output power, as illustrated in Fig. 5.5, where the peak voltage is given by (5.1), and the RMS voltage given by (5.2).

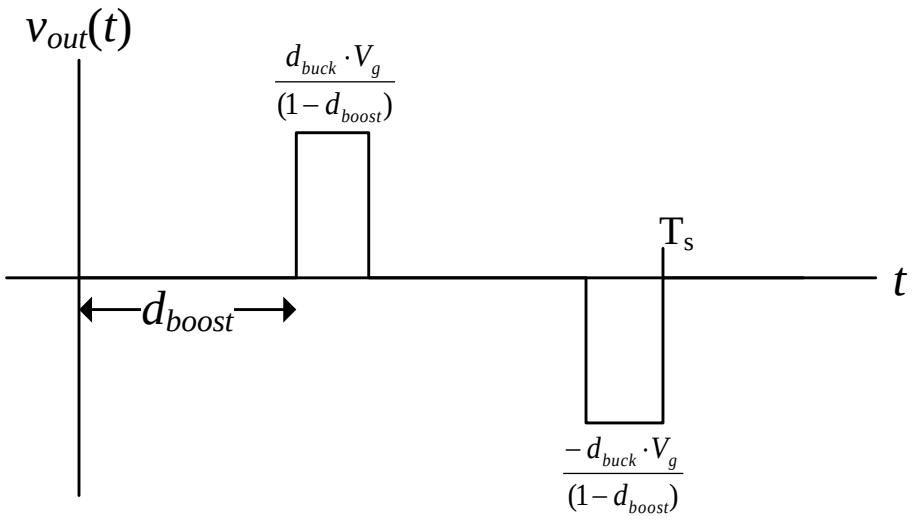


Fig. 5.5 – Two degrees of control freedom from series buck-boost

$$V_{PK} = \frac{D_{buck} \cdot V_g}{(1-D_{boost})} \tag{5.1}$$

$$V_{RMS} = \frac{D_{buck} \cdot V_g}{\sqrt{1-D_{boost}}} \tag{5.2}$$

Figure 5.6 shows the output voltage waveform from a resonant-inverter-based ESG operating in “fulgurate” mode (high peak voltage, low average power). Note that the RMS value of the output voltage is approximately 250 $V_{RMS}$, and the peak voltage is approximately 1 kV.

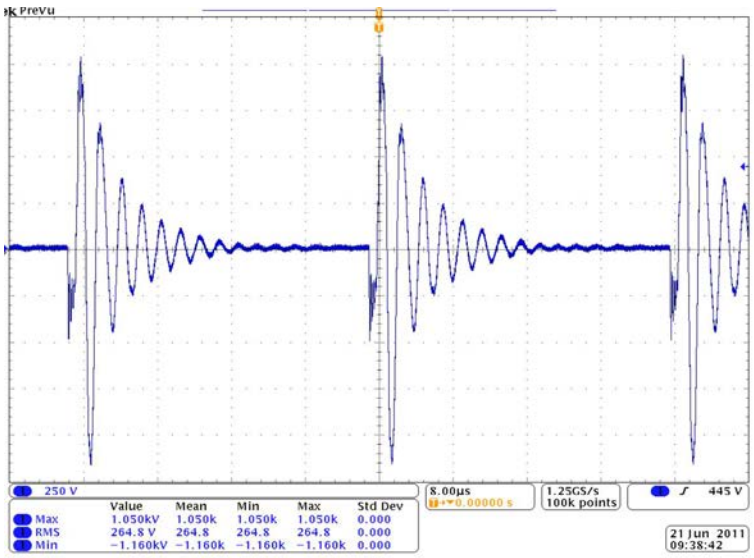


Fig. 5.6 – Modulated output from resonant ESG in fulgurate mode

Figure 5.7 shows the output voltage waveform from a prototype series buck-boost inverter, with both stages operating simultaneously to produce a waveform with high peak voltage and low average power. Figure 5.8 is the same output voltage waveform as Fig. 5.7, shown at a shorter time scale.

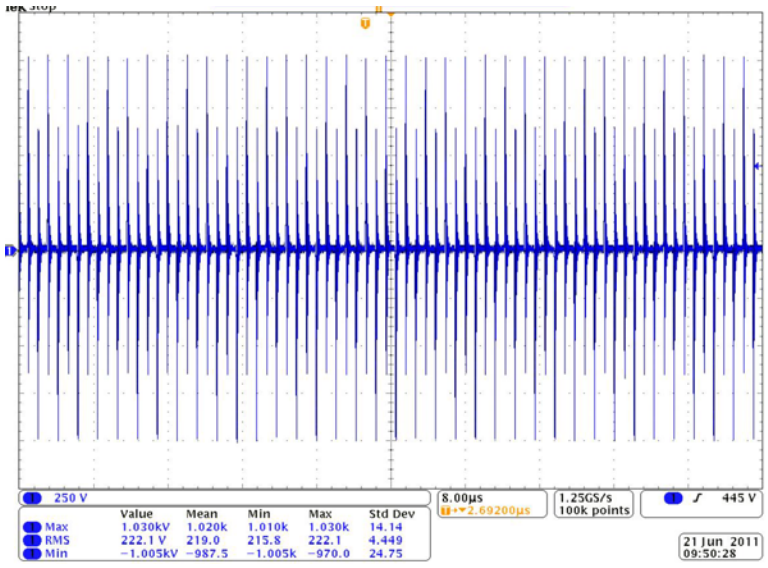


Fig. 5.7 – Continuous output from series buck-boost to realize fulgurate-type effect

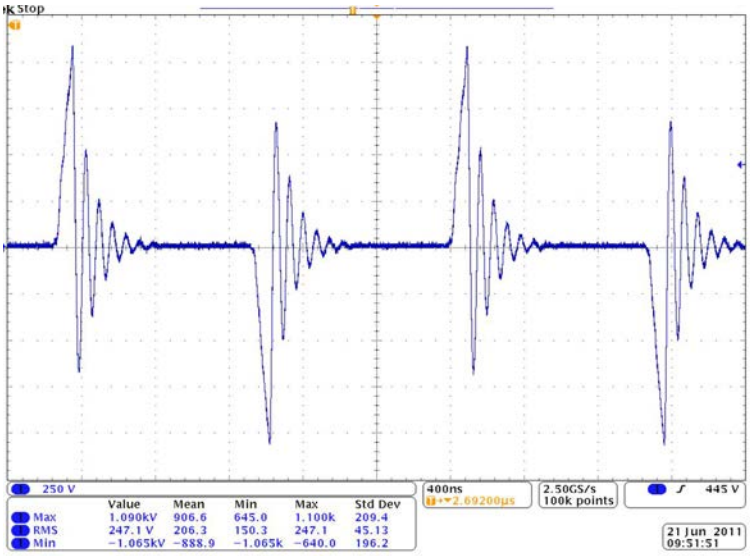


Fig. 5.8 – Zoomed in waveform of Fig. 5.7

The RMS value of the continuous output waveform is, again, approximately 250 $V_{RMS}$, and the peak voltage approximately 1 kV. The output frequency in Figs. 5.7 and 5.8 is 472 kHz, not reduced as in Fig. 5.6. The buck converter is operating at $d$=14%, and the boost inverter simultaneously operating at $d$=96%. Thus, it is possible to produce a continuous (non-modulated) output waveform that will achieve the same tissue effects as the modulated output produced by resonant ESGs. The only parameter value in the prototype ESG that is changed (relative to Chapter 4) is the output transformer turns ratio, which is increased from 1:2 to 1:4, but uses the same interleaving. In use, switching between cutting and non-cutting modes occurs infrequently enough that mechanical relays could reasonably be used to swap output transformers.

Figure 5.9 shows two attempts at surface coagulation made in galline muscle tissue – one made with a modulated, resonant ESG (ForceTriad), and one made with the series buck-boost

prototype – both showing macroscopically similar results. Note that carbonization and shallow cutting depth is the expected result.


Fig. 5.9 – Coagulation and charring in galline tissue from modulated and continuous waveforms

## 5.3 – Conclusions

The simultaneous control of two duty cycle commands in a series buck-boost inverter is demonstrated to produce a continuous output waveform with high peak voltage and low average power, appropriate for use in non-cutting electrosurgical applications. This represents a major simplification over prior-art methods, as it does not require modulation of the output carrier. Tissue effects from continuous high voltage waveforms are shown to be similar to those achieved with a modulated waveform.

# CHAPTER 6

# CONCLUSIONS

This thesis approaches the design of electrosurgical generators with a revolutionary new approach to output regulation, implementing various CPM control methods to achieve near-deadbeat control over output current, power, and voltage.

Two methods of producing constant power AC sources are presented, using fixed-limit CPM control of a full-bridge boost inverter, and using NLC control of a DC-DC buck converter series connected to a full-bridge inverter. Both methods demonstrate extremely fast transient response, and require only a single sensor on the inductor current. The logical combination of these stages realizes a series buck-boost inverter, sharing a common inductor, with a wide dynamic range constant power output characteristic. Addition of constant current and voltage limits completes the production of the ideal ESG output characteristic.

Modeling and analysis of the constant power sources lends insight into which limitations prevent the constant power sources from behaving ideally. Steady-state errors in delivered power arise from peak-to-average differences and addition of artificial compensating ramp, and these errors can be minimized by increasing the size of the inductor and decreasing the magnitude of compensating ramp. Transient performance of the power sources is predicted by observing the closed-loop output impedance. In the case of the CPM boost power source, increasing inductor size improves steady-state performance and has no impact on the transient response. The NLC

buck power source exhibits a constant power source bandwidth approximately defined by $R/L$. Discrete-time sampling effects are shown to be inconsequential for the parameter values used in this work.

A prototype ESG, constructed using the presented CPM-based system architecture, realizes the ideal ESG output characteristic, and demonstrates near-deadbeat output power regulation and voltage limiting. When used to cut human tissue analog, the prototype ESG shows an order-of-magnitude reduction in standard deviation of per-cycle output power. Through histological analysis of electrosurgically-cut porcine liver tissue, it is shown that improved power regulation directly correlates with decreased collateral tissue damage. This conclusion is previously unknown in the literature, but has profound clinical implications, and should be of considerable interest to ESG manufacturers who underestimate the importance of fast transient response.

By simultaneously manipulating both degrees of control freedom available in a series buck-boost inverter, it is demonstrated that high-peak-voltage, low-average-power waveforms can be generated without resorting to pulsating or modulating the output carrier. As design of power stages capable of producing such modulated waveforms are complex, this represents a significant simplification.

## 6.1 – List of Specific Contributions

- CPM control of a full-bridge boost inverter is shown to produce a constant power AC source, achieving near-deadbeat output power regulation, with no need to sense output quantities.
- Nonlinear carrier-control of a buck converter is shown to produce a constant power source, with near-deadbeat power regulation, and no need to sense output quantities.
- Series combination of the nonlinear carrier-controlled buck converter with a fixed-limit CPM boost inverter produces a wide-range constant power source with dynamic range ideal for use in ESGs.
- Modeling of the constant power sources produces expressions for the constant power bandwidth and steady-state errors, guiding design of the power source stages.
- The series buck-boost inverter, combined with a CPM-based control system, is shown to be capable of producing the ideal ESG output characteristic (constant power source with maximum voltage and current limits), achieving near-deadbeat power regulation, instantaneous voltage- and current-limiting, and requiring only a single sensor.
- Tissue thermal spread is experimentally demonstrated to be directly correlated to per-cycle output power regulation: a conclusion of significant clinical importance which was previously unknown in the literature.
- Continuous non-cutting waveforms are demonstrated to have similar tissue effects to prior-art modulated schemes, presenting the opportunity to develop markedly simpler multi-function ESGs.

## 6.2 – Patents

- United States Provisional #61/426,985, "*Dual-Current-Mode Controller for Regulation of Electrosurgical Generator Output Power,*" Inventors: D. Friedrichs, R. W. Erickson, and J. Gilbert. Filed 12/23/2010. 24pgs.

- United States Provisional #61/530,528, "*Constant power source by nonlinear carrier-control of a buck converter for use in electrosurgical generator,*" Inventors: D. Friedrichs, R. W. Erickson, and J. Gilbert. Filed 9/2/2011. 31pgs.

## 6.3 – Publications

- **Published/Presented:**

  - D. Friedrichs, R. W. Erickson, and J. Gilbert, "A New Dual Current-Mode Controller Improves Power Regulation in Electrosurgical Generators," *IEEE Transactions on Biomedical Circuits and Systems,* accepted April 21, 2011, to be published.

  - D. Friedrichs, R. W. Erickson, and J. Gilbert, "A New System Architecture Improves Output Power Regulation in Electrosurgical Generators," *33rd Annual IEEE Engineering in Medicine and Biology Society Conference*, Boston, MA, Aug. 30 – Sept. 3, 2011, pp.6870-6873.

- **In Review:**
  - D. Friedrichs, M. I. Koster, R. W. Erickson, and J. Gilbert, “Improving Output Power Regulation Decreases Collateral Tissue Damage in Electrosurgery,” submitted to *IEEE Transactions on Biomedical Engineering*, 6 pgs.

## 6.4 – Future Work

Potential future areas of investigation related to this work include:

- Use of average current-programmed mode control, rather than peak current-programmed mode control, to eliminate peak-to-average-type errors, which would allow for a reduction in the size of the shared inductor, which would improve the NLC buck power source transient response.
- Soft switching of boost stage transistors, to decrease switching element stress and reduce radiated EMI.
- Further investigation of non-cutting modes, to efficiently realize these modes using the same converter and control system.

# References

[1] L. E. Curtiss, “High frequency currents in endoscopy: A review of principles and precautions,” *Gastrointestinal Endoscopy*, vol. 20, no. 1, pp. 9 -12, 1973.

[2] D. V. Palanker, A. Vankov, and P. Huie, “Electrosurgery With Cellular Precision,” *IEEE Transactions on Biomedical Engineering*, vol. 55 no. 2, pp. 838-841, Feb 2008.

[3] Medtech Insight, U.S. Markets for Electrosurgical and Thermal Ablation Projects, Report #A556, Jul 2006.

[4] D. E. Barlow, “Endoscopic applications of electrosurgery: a review of basic principles”. *Gastrointestinal Endoscopy*, vol. 28, no. 2, pp. 73-76, 1982.

[5] W. M. Honig, “The Mechanism of Cutting in Electrosurgery,” *IEEE Transactions on Biomedical Engineering*, pp. 58-62, Jan. 1975.

[6] N. N. Massarweh, N. Cosgriff, D. P. Slakey, “Electrosurgery: History, Principles, and Current and Future Uses,” *Journal of the American College of Surgeons*, vol. 202, no. 3, pp. 520-530, March 2006.

[7] D. J. Zinder, “Common myths about electrosurgery,” *Otolaryngology - Head and Neck Surgery*, vol. 123, no. 4, pp. 450-455, Oct. 2000.

[8] J. A. Pearce, *Electrosurgery*. New York: Wiley, 1986.

[9] J. L. Eggleston, J. S. Kennedy, R. C. Platt, and K. D. Taylor, “Instant Response electrosurgery generator for laparoscopy and endoscopy,” *Minimally Invasive Therapies & Allied Technologies*, vol. 5, no. 6, pp. 491-495, 1997.

[10] M. L. Morris, R. D. Tucker, T. H. Baron, and L. M. Wong Kee Song, “Electrosurgery in Gastrointestinal Endoscopy: Principles to Practice,” *The American Journal of Gastroenterology*, vol. 104, pp. 1563-1574, June 2009.

[11] Z. P. Chen, W. H. Miller, R. B. Roemer, T. C. Cetas, “Errors between two- and three-dimensional thermal model predictions of hyperthermia treatments,” *Int. Journal Hyperthermia*, vol. 6, no. 1, pp. 175-191, 1990.

[12] A. K. Ward, C. M. Ladtkow, and G. J. Collins, “Material Removal Mechanisms in Monopolar Electrosurgery,” *Proceedings of the 29th Annual International Conference of the IEEE EMBS*, Lyon, France, pp. 1180-1183, Aug. 23-26, 2007.

[13] J.S. Glaser, A. F. Witulski, R. G. Myers, "Steady-state analysis of the constant-frequency clamped series resonant converter," *IEEE Transactions on Aerospace and Electronic Systems*, vol.30, no.1, pp.135-143, Jan 1994.

[14] A. F. Wittulski, R. W. Erickson, "Steady-State Analysis of the Series Resonant Converter," *IEEE Transactions on Aerospace and Electronic Systems* vol.AES-21, no.6, pp.791-799, Nov. 1985.

[15] R. D. Middlebrook, “Modeling current-programmed buck and boost regulators,” *IEEE Transactions on Power Electronics*, vol. 4, no. 1, pp. 36-52, Jan 1989.

[16] R. W. Erickson and D. Maksimovic, *Fundamentals of Power Electronics*, 2nd ed. New York: Springer, 2004, pp. 456.

[17] D. Maksimovic, Yungtaek Jang, R. W. Erickson, "Nonlinear-carrier control for high-power-factor boost rectifier ," *IEEE Transactions on Power Electronics*, vol.11, no.4, pp.578-584, Jul 1996.

[18] R. Zane, D. Maksimović, “Nonlinear-carrier control for high-power-factor rectifiers based on up-down switching converters,” *IEEE Transactions on Power Electronics*, vol. 13, no. 2, pp. 213 – 221, Mar. 1998.

[19] L. Dixon, “Average Current Mode Control of Switching Power Supplies,” Unitrode Application Note U-140.

[20] J. P. Gegner, C. Q. Lee, "Linear peak current mode control: a simple active power factor correction control technique for continuous conduction mode," *27th Annual IEEE Power Electronics Specialists Conference, 1996. PESC '96 Record.*, vol.1, no., pp.196-202 vol.1, 23-27 Jun 1996.

[21] R. Redl, B. P. Erisman, "Reducing distortion in peak-current-controlled boost power-factor correctors," *Ninth Annual Applied Power Electronics Conference and Exposition, 1994. APEC '94 Conference Proceedings*, vol., no., pp.576-583 vol.2, 13-17 Feb 1994.

[22] R. D. Middlebrook, “Topics in Multiple-Loop Regulators and Current-Mode Programming,” *IEEE Transactions on Power Electronics*, vol. PE-2, no. 2, pp. 109-123, April 1987.

[23] A. R. Brown, “Topics in modeling, measurement, and design of high performance switching regulators,” Ph.D. thesis, Power Electronics Group, California Institute of Technology, Pasedena, 1981.

[24] R. B. Ridley, “A New Small-Signal Model for Current-Mode Control,” Ph.D. dissertation, Virginia Polytechnic Institute and State University, Blacksburg, 1990.

[25] F. Dong Tan and R. D. Middlebrook, “A Unified Model for Current-Programmed Converters,” *IEEE Transactions on Power Electronics*, vol. 10, no. 4, pp.397-408, July 1995.

[26] S. Freeland and R. D. Middlebrook, “A unified analysis of converters with resonant switches,” *IEEE PESC Record*, pp.20-30, 1987.

[27] D. Friedrichs, R. W. Erickson, and J. Gilbert, “A New Dual Current-Mode Controller Improves Power Regulation in Electrosurgical Generators,” *IEEE Transactions on Biomedical Circuits and Systems*, accepted April 21, 2011, to appear in vol. 5, no. 5, Oct. 2011.

[28] D. Friedrichs, R. W. Erickson, and J. Gilbert, "A New System Architecture Improves Output Power Regulation in Electrosurgical Generators," *33rd Annual IEEE Engineering in Medicine and Biology Society Conference*, Boston, MA, Aug. 30 – Sept. 3, 2011, pp.6870-6873.

[29] G. K. Miller, D. B. Drennan, and D. J. Maylahn, "The effect of technique on histology of arthroscopic partial meniscectomy with electrosurgery," *Arthroscopy: The Journal of Arthroscopic and Related Surgery*, vol. 3, no. 1, 1987, pp. 36-44.

[30] M. E. Ruidiaz, et. al, "Quantitative Comparison of Surgical Margin Histology Following Excision With Traditional Electrosurgery and a Low-Thermal-Injury Dissection Device," *Journal of Surgical Oncology*, July 2011, doi: 10.1002/jso.22012 [Epub ahead of print].

[31] R. Mausberg, H. Visser, T. Aschoff, K. Donath, and W. Krüger, "Histology of laser- and high-frequency-electrosurgical incisions in the palate of pigs," *Journal of Cranio-Maxillofacial Surgery*, vol. 21, no. 3, pp. 130-132, April 1993.

[32] Y. Yin, R. Zane, R. Erickson, J. Glaser, "Direct modeling of envelope dynamics in resonant inverters," *IEE Electronics Letters*, vol. 40, no. 13, pp. 834 – 836, June 2004.

[33] D. Friedrichs, M. I. Koster, R. W. Erickson, and J. Gilbert, "Improving Output Power Regulation Decreases Collateral Tissue Damage in Electrosurgery," submitted *to IEEE Transaction on Biomedical Engineering*, 6 pgs.

[34] S. J. Vore, *et. al*, "Comparative healing of surgical incisions created by a standard 'bovie,' the Utah Medical Epitome Electrode, and a Bard-Parker cold scalpel blade in a porcine model: a pilot study," *Annals of Plastic Surgery*, vol. 49, no. 6, pp. 635-45, Dec. 2002.

[35] E. I. Chang, G. A. Carlson, J. G. Vose, E. J. Huang, and G. P. Yang, "Comparative healing of rat fascia following incision with three surgical instruments," *Journal of Surgical Research*, vol. 167, no. 1, pp 47-54, May 2011.